# DESIGN AND DEVELOPMENT OF COMPACT MULTIPHOTON MICROSCOPES

by

SeyedSoroush Mehravar

---

A Dissertation Submitted to the Faculty of the

COLLEGE OF OPTICAL SCIENCES

In Partial Fulfillment of the Requirements
For the Degree of

DOCTOR OF PHILOSOPHY

In the Graduate College

THE UNIVERSITY OF ARIZONA

2016

THE UNIVERSITY OF ARIZONA
GRADUATE COLLEGE

As members of the Dissertation Committee, we certify that we have read the dissertation prepared by SeyedSoroush Mehravar
entitled Design and Development of Compact Multiphoton Microscopes
and recommend that it be accepted as fulfilling the dissertation requirement for the Degree of Doctor of Philosophy.

Date: 18 Aug 2016
Khanh Q. Kieu

Date: 18 Aug 2016
Nasser Peyghambarian

Date: 18 Aug 2016
Gholam A. Peyman

Date: 18 Aug 2016

Date: 18 Aug 2016

Final approval and acceptance of this dissertation is contingent upon the candidate's submission of the final copies of the dissertation to the Graduate College.
I hereby certify that I have read this dissertation prepared under my direction and recommend that it be accepted as fulfilling the dissertation requirement.

Date: 18 Aug 2016
Dissertation Director: Khanh Q. Kieu

# STATEMENT BY AUTHOR

This dissertation has been submitted in partial fulfillment of the requirements for an advanced degree at the University of Arizona and is deposited in the University Library to be made available to borrowers under rules of the Library.

Brief quotations from this dissertation are allowable without special permission, provided that an accurate acknowledgement of the source is made. Requests for permission for extended quotation from or reproduction of this manuscript in whole or in part may be granted by the head of the major department or the Dean of the Graduate College when in his or her judgment the proposed use of the material is in the interests of scholarship. In all other instances, however, permission must be obtained from the author

SIGNED: SeyedSoroush Mehravar

# ACKNOWLEDGMENTS

Throughout my journey as a graduate student in College of Optical Sciences, I received invaluable support from my family, advisors, colleagues and friends. No need to say that without them, I would not have accomplished this much. I would like to express my sincere gratitude here.

First and foremost, I would like to thank my advisor, Professor Khanh Kieu. His passion about science and fundamental research has been a motivation for me to work hard and try to implement the applied ideas through experiments. Khanh discussed and debated all the ideas in my research studies, helped me developing them, carefully read and edited numerous manuscript drafts, and gave me a wealth of suggestions to improve. It was a great opportunity to work closely with him and be part of his research team. I will never forget his efforts to make me enthusiastic about the world and improving the lives using novel scientific techniques. I have learnt from him a lot and I have rarely seen someone like him to work hard with such enthusiasm and passion. I want to thank him again for his patience and support.

Next, I have to sincerely appreciate my advisor and supervisor, Professor Nasser Peyghambarian, who gave me the opportunity of being part of his team. His support through these five years financially and emotionally helped me pursue my studies and research. Without his effort to support the graduate students by providing state-of-the-art equipment and laboratories, the research projects would not have been completed.

Much gratitude goes to Dr. Gholam A. Peyman as my advisor and committee member. He was a great mentor to me throughout the years we have been collaborating. His enthusiasm and passion about the research and making the lives better is inexpressible. Besides his humbleness and kindness, his passion for sciences makes him as my role model. He was the only individual that I could talk about everything with him. I would like to thank Professor Masud Mansuripur, who has been guiding me through these years. He was the very first person in the College that I could stop by his office anytime and start a discussion. His personality and character is exemplary. I would like also to thank Professor Robert A. Norwood, who was a great mentor for my projects. He has been always nice to everyone and tried his best to solve students' problems with his happy face and unforgettable laughs.

Great faculty members and staff of the College of Optical Sciences have made the past five years a unique experience for me. Majid Behabadi has been the only person in the College always saying "Good Morning!" even at 5p.m. I would like to thank him for his support and making our environment friendly and enjoyable. The numerous support from Linda Schadler is greatly appreciated from writing admission letters to providing funding sources for me. Mark Rodriguez has helped me a lot as a graduate advisor throughout past three years. Amanda Ferraris has been always there with her office door open when I've had questions. Thank to Ruth Corcoran and Melissa Ayala for their great job and help. I should also thank Palash Gangopadhyay for his support and being there whenever I had scientific questions.

Special thanks to the former and current lab members and colleagues, Babak Amirsolaimani, Soha Namnabat, Farhad Akhoundi, Dmitriy Churin, Roopa Gowda, Raj Patil, Benjamin Cromey, Dawson Baker, Neil Ou, Jashua Olson, Erfan Motefakker Fard, Sander Zandbergen, Roland Himmelhuber, Byron Coccolivo, Lasse Karvonen, Antii Saynatjoki, Sasan and Nam Nguyen. I do believe that we have made history to be remembered, both inside and outside the lab.

Additional thanks to my friends for being the ones that I always wanted, needed, and appreciated. Negin, Kimia, Suzan, Mehrdad, Davoud, Andisheh, Hameds, Nimas, Hamid and Elmira; Tucson will miss the time we spent together after we leave. I would like to thank other close friends Arash, Soheil, Alireza and Amirhossien, who although were not in Tuscon; they have been always in my heart.

Last, but most importantly, my deepest debt of gratitude goes to my parents,

Ahmad and Effat, and my sweet little sister, Sepideh, for all their prayers, supports, and inspirations. I also would like to thank my best friends, Shiva, and my wingman, Shayan, who have seen and helped me through every step I've taken in the past few years. All my research projects have been supported by sate of the Arizona TRIF Photonics and Imaging fundings.

# DEDICATION

*To my mother, father, and sister*

# TABLE OF CONTENTS

LIST OF FIGURES . . . . . . . . . . . . . . . . . . . . . . . . . . . . 10

ABSTRACT . . . . . . . . . . . . . . . . . . . . . . . . . . . . . . . . 17

CHAPTER 1 Introduction . . . . . . . . . . . . . . . . . . . . . . . . 18

CHAPTER 2 Multiphoton Microscopy . . . . . . . . . . . . . . . . . . 24
- 2.1 Multi-photon theory and instrumentation . . . . . . . . . . . . . . 24
  - 2.1.1 Theory . . . . . . . . . . . . . . . . . . . . . . . . . . 24
  - 2.1.2 MPM schematic . . . . . . . . . . . . . . . . . . . . . . 27
- 2.2 Optical Design . . . . . . . . . . . . . . . . . . . . . . . . . . 30
  - 2.2.1 Tube lens . . . . . . . . . . . . . . . . . . . . . . . . 32
  - 2.2.2 Scan lens . . . . . . . . . . . . . . . . . . . . . . . . 34
  - 2.2.3 Relay lens . . . . . . . . . . . . . . . . . . . . . . . . 37
  - 2.2.4 Entire optical design . . . . . . . . . . . . . . . . . . 37
- 2.3 MPM characterization . . . . . . . . . . . . . . . . . . . . . . . 41
  - 2.3.1 Lateral and axial resolution using FL microspheres . . . . . 45
  - 2.3.2 Measurement of lateral and axial resolution using nonlinear knife edge technique . . . . . . . . . . . . . . . . . . . . . 46
  - 2.3.3 Field curvature . . . . . . . . . . . . . . . . . . . . . 51
- 2.4 Detection . . . . . . . . . . . . . . . . . . . . . . . . . . . . . 54

CHAPTER 3 MPLAB: LabVIEW based laser-scanning software for multiphoton microscopy . . . . . . . . . . . . . . . . . . . . . . . . . . . 57
- 3.1 Data acquisition with NI-PCI-6110 using AI and AO ports . . . . . 57
- 3.2 Image analysis . . . . . . . . . . . . . . . . . . . . . . . . . . 64
- 3.3 Challenges . . . . . . . . . . . . . . . . . . . . . . . . . . . . 65

CHAPTER 4 Applications of MPM in bioscience and material characterization . . . . . . . . . . . . . . . . . . . . . . . . . . . . . . . . 69
- 4.1 Label-free multiphoton imaging of dysplasia in Barrett's esophagus 69
  - 4.1.1 Introduction . . . . . . . . . . . . . . . . . . . . . . . 69
  - 4.1.2 Multi-Photon Microscopy System . . . . . . . . . . . . . . 71
  - 4.1.3 Methods and Sample Preparation . . . . . . . . . . . . . . 73
  - 4.1.4 Results . . . . . . . . . . . . . . . . . . . . . . . . . 74
  - 4.1.5 Discussion . . . . . . . . . . . . . . . . . . . . . . . . 79
  - 4.1.6 Conclusion . . . . . . . . . . . . . . . . . . . . . . . . 81
- 4.2 Multiphoton microscopy as a detection tool for photobleaching of EO . . . . . . . . . . . . . . . . . . . . . . . . . . . . . . . . . 81

TABLE OF CONTENTS – *Continued*

4.2.1 Introduction . . . . . . . . . . . . . . . . . . . . . . . . . . . 81
4.2.2 Experimental setup . . . . . . . . . . . . . . . . . . . . . . . . 83
4.2.3 Results and discussion . . . . . . . . . . . . . . . . . . . . . . 85
4.2.4 Conclusion . . . . . . . . . . . . . . . . . . . . . . . . . . . . 91
4.3 Multi-photon microscopy for characterization of 2D materials . . . 92

CHAPTER 5 Summary . . . . . . . . . . . . . . . . . . . . . . . . . . . . . 104

# LIST OF FIGURES

1.1 a) Comparison between different imaging modalities in terms of penetration depth and resolution. b) Excitation volume for CW and femtosecond laser. In excitation with femtosecond laser only the focal volume of the objective lens is excited and photodamage and photobleaching are reduced for out-of-focus regions. . . . . . . 19

2.1 Jablonski diagram showing 5 different nonlinear process of 2PEF, 3PEF, SHG, THG and CARS . . . . . . . . . . . . . . . . . . . . . . . . 24
2.2 THG signal from center of a sphere with different sizes. The graph shows the FTHG and BTHG versus the sphere size and as can be seen the BTHG has smaller period compared to FTHG signal . . . . 28
2.3 SOLIDWORKS model of the MPM (courtesy of Benjamin Cromey) 28
2.4 Design of the first microscope prototype: schematic and spot diagram for 1040nm illumination . . . . . . . . . . . . . . . . . . . . . . . . 31
2.5 OPD fan and field curvature for the first prototype design . . . . . 32
2.6 Simple objective lens representation . . . . . . . . . . . . . . . . . . 33
2.7 Tube lens schematic and the spot diagram for maximum 2.6 degree optical FOV . . . . . . . . . . . . . . . . . . . . . . . . . . . . 34
2.8 OPD fan and field curvature of the tube lens . . . . . . . . . . . . 35
2.9 Scan lens schematic and the spot diagram for 10 optical degree scanning . . . . . . . . . . . . . . . . . . . . . . . . . . . . . . . . 36
2.10 OPD fan and field curvature of the designed scan lens for maximum 10 optical degree scanning . . . . . . . . . . . . . . . . . . . 36
2.11 Relay lens system consisting of two achromatic lenses with 60mm focal length and two meniscuses with 150mm focal lengths . . . . . 38
2.12 Entire imaging system shown for 10 optical degree scanning angle and a paraxial objective lens model . . . . . . . . . . . . . . . . . . 39
2.13 Spot and OPD fan diagrams. Note that for 10 optical degree scanning angle, the FOV is $488\mu m \times 488\mu m$ and almost diffraction limited. The OPD fan shows a maximum aberration of 0.4 waves . . . 40
2.14 Field curvature and f-theta diagrams. The RMS wavefront error vs. field also shows that for optical fields below 8 degrees, the system is diffraction limited . . . . . . . . . . . . . . . . . . . . . . . . . 40

LIST OF FIGURES – *Continued*

2.15 (a) Schematic of the MPM used for optical characterization of the system. MLL: Mode-locked laser, C: Collimator, G: Galvo scanners, SL: Scan lens, TL: Tube lens, D: Dichroic mirror, L: Lens, F: bandpass filter, PMT: Photomultiplier tube. (b) Emission spectrum of GaAs using 1040nm excitation wavelength. The power dependency measurements show the two and three photon process indicated by the slopes of 2 and 3, respectively . . . . . . . . . . . . . . 43
2.16 Two and three photon images of $0.5\mu m$ microspheres. The measured data points are fitted with a Gaussian PSF and the FWHM of the PSF is considered as system resolution . . . . . . . . . . . . . . 45
2.17 Resolution measurement using GaAs wafer. The laser scans across the sharp edge of a GaAs wafer and the two and three photon process resolution is extracted by the curves fitted to the measured data points . . . . . . . . . . . . . . . . . . . . . . . . . . . . . . 47
2.18 Left: Schematic diagram of the objective lens field curvature (Petzval surface). Right: THG signal generated from the surface of the GaAs wafer when its location is below (down), at the focal plane (middle) and above (up) the focal plane . . . . . . . . . . . . . . . 52
2.19 Top row: Objective lenses field curvatures for 20× aspheric (Left), 40× Olympus (Middle) and 50× Jena Zeiss (Right). Bottom row: projected Petzval surfaces in top row onto xz- and yz-plane. The projected curves are fitted by a quadratic curve showing the quadratic field dependency of field curvature . . . . . . . . . . . . 53
2.20 Uncorrected cover slip (left) and corrected for field curvature image (right) using the data retrieved by measuring the field curvature for 20× aspheric objective lens . . . . . . . . . . . . . . . . . . . 54
2.21 Hamamatsu PMT data sheet and specifications . . . . . . . . . . . 55
2.22 Box for controlling the gain of PMTs. A potentiometer controls the gain voltage through a divider circuit. A LED indicates the on and off status . . . . . . . . . . . . . . . . . . . . . . . . . . . . . . 56

3.1 MPLab control panel for image display and acquisition parameters 60
3.2 MPLab block diagram for writing and reading the data points . . . 61
3.3 nonuniform illumination correction. Left and right columns show 2PEFL and THG images before and after nonuniform illumination correction. Scale bars: 600$\mu$m . . . . . . . . . . . . . . . . . . . . . 66

LIST OF FIGURES – *Continued*

4.1 Schematic diagram of the in-house MPM system (left) and the multiphoton spectrum of Barrett Esophagus tissue (right). Red: Optical spectrum of the multiphoton generated signal from a normal tissue showing a strong THG signal at 520nm. Inset: zoom-in SHG spectrum . . . . . . . . . . . . . . . . . . . . . . . . . . . . . 72

4.2 Comparison between multi-photon microscopy and conventional light microscopy of BE tissue that is negative for dysplasia. (a) H&E conventional light microscopy image showing intestinal metaplasia with goblet cells. There is surface maturation, low nucle nuclear to cytoplasmic ratio and no dysplasia. (b-d) magnified regions shown in (a). (e) High resolution THG signal from MPM and (f-h) the magnified regions in (e). (i) SHG signal recorded simultaneously with the THG signal showing collagen distribution in the stroma and blood vessels. (j-l) magnified marked regions in the SHG image to show collagen in the basement membrane. The THG signal has a clear correlation to the H&E light-microscope image. The architectural structure of nuclei indicates that the tissue has no dysplastic feature. The yellow arrows show the cells with no evidence of dysplasia. (FOV in (e) and (i): $1000 \times 750 \mu m^2$, acquisition time: 2min) . . . . . . . . . . . . . . . . . . . . . . . . . 76

4.3 Multi-photon and conventional light microscopy images for low-grade dysplastic BE tissue. (a) Conventional light microscopy image of the tissue stained with H&E; there is intestinal metaplasia with goblet cells, surface luminal cells displaying nuclear stratification, hyperchromasia, and an increased nuclear to cytoplasmic ratio (N: C). (b-d) magnified regions marked in the H&E image. (e-h) High resolution THG images that show features of low-grade dysplasia in the same biopsy. (i-l) corresponding simultaneous SHG signals of the THG images that display the presence of collagen. The spatial distribution of cell nuclei is consistent with low-grade dysplasia. The cells with low-grade dysplasia are marked with arrows. (FOV in (e) and (i): $750 \times 1000 \mu m2$, acquisition time: 2min). The vertical white lines in (j)-(l) are the PMT artifacts . . . . 77

LIST OF FIGURES – *Continued*

4.4 MPM and conventional light microscopy images of high-grade dysplastic tissue. (a) Conventional light microscopy image of the tissue after labeling with H&E. There is a progressive dysplastic change in a background of intestinal metaplasia. Cells have marked hyperchromatic nuclei nuclear stratification, loss of polarity and a markedly increased N:C ratio, considerably more than in low grade dysplasia. (b-d) magnified squared regions marked in (a). (e) High resolution THG and (f-h) corresponding magnified regions. (i) High resolution SHG image and (j-l) the magnified regions marked in to show basement membrane collagen (i). The dense nuclei with variable shapes and sizes as well as the loss of orderly arrangement of the cells are consistent with high-grade dysplasia. Arrows represent the cells with high-grade dysplasia. (FOV in (e) and (i): $500 \times 500 \mu m^2$, acquisition time: <1min) . . . . . 78

4.5 SHG signal from Barrett's with non-dysplastic dysplasia (a), low grade dysplasia (b) and high grade dysplasia (c). Corresponding graphs to the right show the thickness of the basement membrane collagen measured at each of the three chosen points per image, which confirm increasing thickness with progression of dysplasia . 80

4.6 The schematic of the multi-photon microscope, and b) diagram showing various sources and probes on materials photodegradation study . . . . . . . . . . . . . . . . . . . . . . . . . . . . . . . . 84

4.7 $LiNbO_3$ multiphoton spectrum excited at 1550nm, and b) normalized SHG intensity versus laser exposure timing for various laser powers . . . . . . . . . . . . . . . . . . . . . . . . . . . . . . . . . 86

4.8 Multiphoton spectrum of DR1 on fused silica, the inset shows the log-log plot of the output THG signal versus input power, b) normalized THG intensity versus exposure timing for various laser powers, and c) THG profile of the sample where each square . . . . 87

4.9 DR1 decay curve with 30mW power (circle-marked line), best fitted one- (dash- dotted line), double-(dotted line), and stretched-exponential (solid line) functions, b) log- log plots of the photobleaching rates $k_1$ and $k_2$ vs. irradiation power, and c) the ratio between parameters $\mathrm{k}_1$ and $k_2$ (left axis) and $A_1$ and $A_2$ (right axis) vs irradiation power . . . . . . . . . . . . . . . . . . . . . . . . . 88

LIST OF FIGURES – *Continued*

4.10 Multiphoton spectrum of SEO250 on fused silica, the inset shows a UV/Vis absorption spectrum of SEO250 (top) and the log-log plot of the output THG signal versus input power (bottom), b) normalized THG intensity versus laser exposure timing for various laser powers, and c) THG profile of the sample where each square is continuously exposed by a different laser power and exposure timing . 90

4.11 a) Fitting SEO250 decay curve with 19.8 mW power (circle-marked line) with 1- (dash-dotted line), 2-(dotted line), and stretched-(solid line) exponential functions. b) log- log plots of the photobleaching rates $k_1$ and $k_2$ for SEO250, inset: the ratio between parameters $A_1$ and $A_2$ vs irradiation power, and c) the photobleaching rate versus irradiation power when the experimental data was fitted with a stretched-exponential function . . . . . . . . . . . . . . . . . . . . . 91

4.12 (a) Composite of SHG (red) and THG (green), (b) SHG in the poled region, (c) THG from on top of the gold electrodes. The orange box in (b) indicates the region in which the quantitative SHG data was collected. (d) Ratio of the measured $r_{33}$ to the square root . . . . . . 93

4.13 Typical multiphoton micrographs of a sample containing exfoliated graphene on $SiO_2/Si$ substrate. (a) Fluorescence, (b) third-harmonic signal, and (c) merged RGB image using fluorescence (red) and THG (green) signals. One particularly interesting few-layer graphene flake considered below is marked with white circles and shown magnified in the merged RGB image . . . . . . . . 93

4.14 Dependence of the THG peak signal on the laser peak power and number of graphene layers. Dots are measurement values; the curves are exponential fits to the power dependence. In the logarithmic plot in the inset, three points corresponding to the lowest THG power deviate from the general trend because the power level is below the linear regime of our detection system . . . . . . . 95

4.15 (a) SHG and (b) THG images of the few-layer GaSe flake, (c) RGB composite image generated from the SHG and THG images, and (d) cross-sections of the SHG and THG signals taken from the white dashed line in (c). The spectra of the generated light have been measured from the points marked with Roman numbers II, V and VII in (c). (e). Measured spectra of the generated light from three different positions (different thicknesses) on the flake. The positions are marked by Roman numbers II, V and VII . . . . . . . 96

4.16 Power dependence of the (a) SHG and (b) THG signals. (c) SHG and THG signals as a function of the number of the GaSe layers measured with $1kW$ excitation peak power . . . . . . . . . . . . . . 97
4.17 (a) SHG and (b) THG images of the few-layer GaTe flake. (c) RGB composite image generated from the SHG and THG images. (d) Cross-sectional SHG and THG signals taken from the blue dashed line in (c); scale bars in the SHG and THG images are $10\mu m$. (e) AFM image of the staircase area where the intensity is at maximum for both SHG and THG. (f) AFM cross-section of the staircase area taken from the white dashed line B-B′ in (e) showing the steps from 17 to 57nm. Excitation peak power dependence of the (h) SHG and (i) THG signals. The lines are fits to square (h) and cubic (i) power dependences . . . . . . . . . . . . . . . . . . . . . . . . . . . . . 98
4.18 SHG intensity versus the induce voltage across the electrodes . . . 99
4.19 Normalized multiphoton excitation spectra and micrographs of (a) the blend of BBCP D with 30 wt % QDs and (b) neat polymer sample. The wavelength of light for excitation was 1550nm . . . . . . . 100
4.20 Damage threshold of directly deposited graphene is comparable to mono- and bi-layered graphene prepared by the transfer technique. ÎŤIntensity is the intensity difference of THG signal between the studied area and the reference area. The damage area has less THG than the pristine area. Multiphoton microscopic images of (a) transferred graphene film with a tear and folded areas and (b) directly deposited graphene with a scratch made by a scalpel. (a-inset) average graphene film thickness is comparable to folded bi-layered graphene prepared by transfer technique. (Both image size is about $300 \times 300\mu m^2$. Color bar indicates the intensity of THG signal.) . . . . . . . . . . . . . . . . . . . . . . . . . . . 101
4.21 (a) Optical setup used to measure the third-harmonic signal of the silicon samples. (b) Measured third-harmonic spectra for the samples with different trench and ridge geometries. (c) THG signal as a function of the angle of polarization of the input be beam. (d) Spatially resolved optical images of the third-harmonic signal for two orthogonal polarizations of the input beam . . . . . . . . . . . 102
4.22 Multiphoton microscope images of the boundaries between textured (left) and planar (right) substrates coated with rhodamine 6G (a), green fluorescent protein (b), and chlorophyll (c) . . . . . . . 103

LIST OF FIGURES – *Continued*

4.23 Fluorescence signals (left column) and enhancements (right column) calculated from the MPM measurements. The inset shows five images of the R6G sample at different focus positions . . . . . . 103

# ABSTRACT

A compact multi-photon microscope (MPM) was designed and developed with the use of low-cost mode-locked fiber lasers operating at 1040nm and 1560nm. The MPM was assembled in-house and the system aberration was investigated using the optical design software: Zemax. A novel characterization methodology based on 'nonlinear knife-edge' technique was also introduced to measure the axial, lateral resolution, and the field curvature of the multi-photon microscope's image plane. The field curvature was then post-corrected using data processing in MATLAB. A customized laser scanning software based on LabVIEW was developed for data acquisition, image display and controlling peripheral electronics. Finally, different modalities of multi-photon excitation such as second- and third harmonic generation, two- and three-photon fluorescence were utilized to study a wide variety of samples from cancerous cells to 2D-layered materials.

# CHAPTER 1

# Introduction

Multi-Photon Microscopy (MPM) is a nonlinear imaging modality that provides sub-micro meter resolution images with millimeter penetration depth. The use of high peak power laser pulses generates a tremendous photon flux confined at the focal volume of a high numerical aperture (NA) objective lens resulting is an optical sectioning enabling 3D reconstruction of highly scattering tissues. There are various imaging modalities with different working principals and applications. In each technique there is a trade-off between penetration depth and resolution of the imaging. Figure 1.1(a) illustrates this trade-off pictorially for different imaging modalities. Among them, MPM can provide sub-micrometer resolution with descent penetration depth of $\sim 2mm$. The inherent optical sectioning property of MPM which confines the excitation only in the small focal volume of an objective lens reduces the out-of-focus photobleaching and photodamage significantly, the known issues with continuous-wave (CW) excitation (Figure 1.1(b)).

Two-photon absorption was first predicted by Maria-Goeppert-Mayer (1906-1972) in her doctoral dissertation in 1931, but it was only back in 1992 that Denk, Strickler and Webb developed the idea of combining two-photon absorption with laser scanning technique to create high-resolution images [1] . MPM has shown its potential for a wide range of applications in neuroscience, cancer detection and high-resolution 3D writing. There are different imaging modalities such as Two- and Three-Photon Excitation Fluorescence (2PEF, 3PEF), Second- and Third-Harmonic Generation (SHG, THG) in Multi-Photon Imaging (MPI) providing different and complementary information about the sample under test. 2PEF and 3PEF signals are generated when atom or molecule transits from ground state to

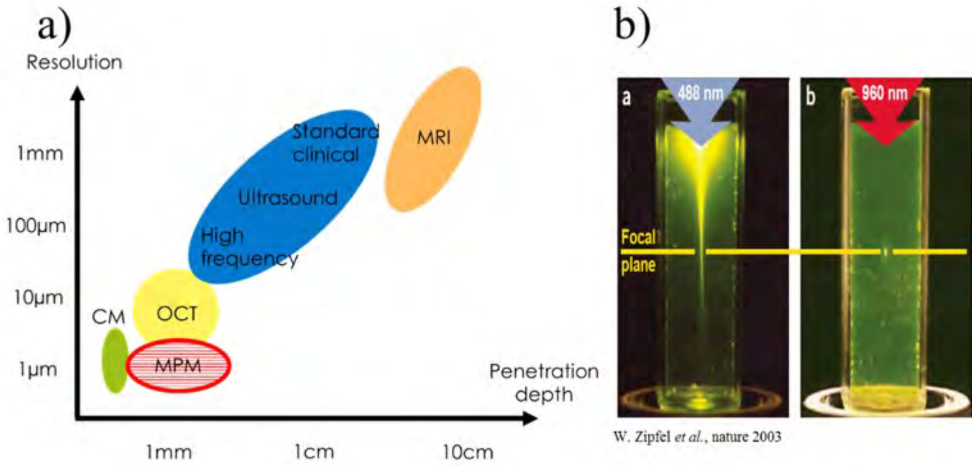

Figure 1.1: a) Comparison between different imaging modalities in terms of penetration depth and resolution. b) Excitation volume for CW and femtosecond laser. In excitation with femtosecond laser only the focal volume of the objective lens is excited and photodamage and photobleaching are reduced for out-of-focus regions.

the excited state which in turn emits a light at a wavelength normally in the visible range of light. SHG and THG are coherent signals that a photon at exactly half and 1/3 of the excitation wavelength is generated when two or three photons are scattered by tissue simultaneously. The harmonic signal is directional and depends on the distribution and direction of the induced dipoles in the focal plane of the sample. SHG can be found in samples where centro-symmetry is broken such as collagen and fibrous structures in biological specimen. THG is sensitive to the interfaces and can be generated where refractive index changes. It was shown that THG signal can be used to distinguish cell boundaries and structures for label-free imaging of different stages of dysplasia in Barrett's esophagus [2] and imaging of targeted lipid microbubbles for cancer studies [3]. THG was also used to monitor the photobleaching of electro-optical polymers under femtosecond illumination [4]. Two-photon microscopy was also used in neuroscience for brain studies [5], dynamic calcium monitoring [6]. Horton et.al [7] used 1700nm excitation wavelength to generate THG and 3PEF signals for in vivo studies of mouse brain and achieved 1.6mm penetration depth inside the cortex. Another suitable wavelength for brain studies was proved to be 1060nm using low-cost and compact fiber lasers with low repetition rates [8, 9, 10]. An automated method by combining two-photon fluorescence microscopy and tissue sectioning used to reconstruct mouse brain in 3D [11]. Mahou et.al used femtosecond Ti:Sa laser followed by OPO to simultaneously excite three chromophores generating multi-color two-photon imaging by wavelength mixing [12]. Custom-made MPM were reported in literature for ex-vivo and in-vivo studies. Negrean et.al optimized the scan and tube lens design for two-photon microscopy covering 600-1700nm wavelength region [13]. Large field of view (FOV) MPM were also designed achieving 5mm FOV to study murine cortex [14]. Another approach was demonstrated by Stirman et.al for two-photon calcium imaging with $> 9.5mm^2$ FOV [15]. Parabolic mirrors were used to improve the laser scanning in confocal and two-photon microscopy [16, 17]. A cost-effective and high-performance two-photon microscope was reported in [18] explaining the system design and modification for different applications. A custom-made two-photon microscope was also developed for video-rate Ca2+ imaging [19]. Nikolenco et.al converted a confocal microscope scan head to two-photon microscope for brain imaging [20]. Random pattern scanning technique was utilized for fast 3D imaging of dendrite processes [21], dendrite Ca2+ spike propagation [22] and cellular network dynamics [23]. Flusberg et.al designed and fabricated an ultra-light weight microendoscope for in vivo brain imaging [24]. MPM requires a mode-locked laser to provide high peak power pulses for initiating nonlinear interaction while preserving low average power to avoid thermal damage on tissue. Ti:Sa lasers are still the workhorse of the MPI field covering excitation wavelengths from 700nm to 1100nm [25, 26, 27, 28, 29, 30, 31, 32, 33]. Squier and Miller reviewed the laser sources for high resolution nonlinear microscopy [34].

The first demonstration of laser scanning microscopy by using Ti:Sa mode-locked laser backs to 1992 [35]. However, the cost and size of Ti:Sa laser prevent MPM to be used widespread in clinical application. Moreover, it requires frequent alignment for long-term operation. Based on scattering theory, utilizing longer NIR wavelength results in deeper penetration inside the scattering tissue. Therefore, there is a need to develop compact and low-cost fiber based mode-locked laser to address the current issues with the excitation source. There has been a strong research and development on using fiber lasers in the field of MPI [36, 37]. A comprehensive review on the fiber laser source development for MPM was reported by Xu and Wise in [38]. There are three major wavelength regions for designing mode-locked fiber lasers. $Yb^{3+}$ [39, 40, 41], $Er^{3+}$ and $Tm^{3+}$ doped fibers cover 1020-1100nm, 1520-1630nm and 1850-2000nm wavelength regions, respectively. However, new windows are being investigated that can cover 1300nm wavelength where biological tissues have low water absorption. Currently, semiconductor saturable absorber mirrors (SESAM) and nonlinear polarization evolution (NPE) are the key important elements to achieve passive mode-locking in fiber lasers [33, 42, 43]. There are limitations in performance and stabilities of mode-locked lasers based on SESAM and NPE. Carbon nanotube saturable absorber (CNTSA) [44, 45] seems to be a promising replacement for passive mode-locking providing compact, low-cost and stable performance design [46]. Adaptive optics was utilized to modify the beam wavefront to generate almost aberration-free waveform resulting in sharp images at deep penetration inside a tissue [47, 48]. Neil et.al used a spatial light modulator to correct specimen-induced aberration in two-photon and confocal microscopy [49]. The parameters estimating the accuracy of sensorless adaptive optics was investigated theoretically and experimentally in [50]. The wavefront correction can be done in real-time for in vivo applications [51, 52, 53]. In adaptive optics, a deformable mirror is used to manipulate the initial wavefront and compensate for the known wavefront aberration existed in the two- or multi-photon microscopy system [54, 55, 56]. Different implementations and techniques have been reported to use adaptive optics in two-photon microscopy [57, 58]. Finally, the performance of sensorless adaptive optics for multiphoton microscopy was reported in [59] and two, three and four photon microscopy were compared in [60]. MPM is a raster scanning imaging modality in which the limited power of the laser source makes fast imaging of structures in 3D challenging. There are different techniques to fasten the image acquisition up to video rate in MPM. One technique called "multifocal multiphoton microscopy (MMM)" is based on the incident beam distribution over multiple foci [61, 62, 63, 64, 65, 66, 67]. Then the frame rate scales with the number of excitation foci. One of challenges with MMM is the constructive interference between multiple foci resulting in a decrease in axial resolution. However, this issue can be solved by delaying the successive foci in time. A frame rate of 600Hz was reported by Bahlmann et.al using this implementation [61]. In MMM a single element detector can no longer be used since different foci have to be mapped into a 2D plane detector. However, this limitation can be solved by using segmented detector or descanned detection scheme. Kim et.al followed this approach by using multianode PMT in which each anode receives photons from corresponding foci on the sample [68]. Another approach for video rate MPI is to use polygon [69] or resonant scanners [19, 70, 71]. In this technique the repetition rate of the excitation source has to be designed so that there are enough pulses per pixel dwell time required for excitation. Since using polygon and resonant scanners do not have flexibility to scan a region of interest with arbitrary scan field, acousto-optic deflectors and tunable lenses are used to address this issue. Using acousto-optic deflectors researchers can access to multiple regions of interest at different lateral planes [72, 73, 74, 75, 76, 77, 78, 79, 80]. Spatiotemporal focusing can also increase the imaging rate in which the pulse is stretched in wavelength using gratings or prisms and then coupled back only at the focal plane of the objective lens [81, 82, 83, 84, 85, 86, 87, 88, 89]. Finally, a high speed imaging device can be realized by rapid axial scanning of the beam instead of lateral scanning by modifying the divergence of the beam at back aperture of the objective lens (remote focusing) [90, 91, 92, 93, 94].

# CHAPTER 2

# Multiphoton Microscopy

## 2.1 Multi-photon theory and instrumentation

### 2.1.1 Theory

MPM is a nonlinear process in which multiple photons are nearly simultaneously absorbed by the material and another photon with larger energy compared to the excitation photon is generated. Figure 2.1 below shows different multi-photon interaction processes. In 2PEF modality two photons are absorbed and the atom or molecule transits from ground state to the excited state. Then, the atom or molecule emits a photon to come back to the ground state. The same scenario

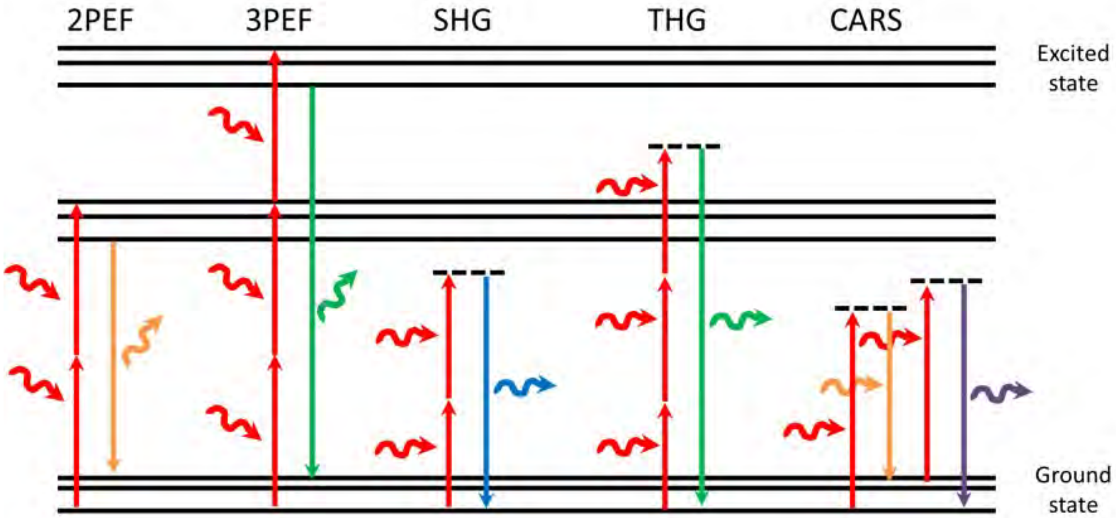

Figure 2.1: Jablonski diagram showing 5 different nonlinear process of 2PEF, 3PEF, SHG, THG and CARS

occurs for 3PEF. In harmonic generation process, two or three photon are scattered simultaneously, but the transition occurs between the ground state and a virtual state instead of a real state as happening in 2- and 3PEFL. Therefore, harmonic generation is a parametric process in which the energy is preserved and the emitted photon is coherent and has an energy exactly equal to the harmonic of the excitation photon. Coherent Anti-Stoke Scattering (CARS) is another multiphoton process which is sensitive to the vibration states of the molecules and can be used to image chemical bonds. The efficiency of a nonlinear process depends on different parameters. Nonlinear process occurs only when the incident photons are confined or concentrated in time and space simultaneously. The space confinement can be fulfilled using high NA objective lenses. However, realizing confinement of photons in time is expensive and hard to implement. This requires to use ultra-short mode-locked lasers and this type of excitation source is the main cost of a MPM. The efficiency of multi-photon process scales with $(\frac{1}{f_r\tau})^{n-1}$, in which $n$,$f_r$ and $\tau$ are the nonlinear order, laser repetition rate and pulse duration. For example, for two-photon process the fluorescence signal can be formulated as [95] :

$$FL = \frac{\eta\sigma}{\tau f_r^2}\left(\frac{\pi NA^2}{hc\lambda}\right)^2 \langle P\rangle^2 e^{-2z/l_s} \tag{2.1}$$

Where $\eta, \sigma, h$ and $c$ are the fluorophore quantum efficiency, fluorophore two-photon absorption cross section, Planck's constant and speed of light, respectively. $\langle P\rangle$ is the laser average power and $l_s$ is the scattering length for the tissue at the excitation wavelength. Note that, the average power has to be kept low to avoid damage or photobleaching of the tissue. This requires to decrease the laser repetition rate to generate large pulse energy. Due to the Mie scattering theory, the scattering at longer wavelengths scales with $\lambda^{-4}$, resulting in larger penetration depth in a highly scattering material for NIR excitation wavelength (assuming linear absorption is small). Moreover, the longer wavelength photons have smaller photon energies preventing damage on the samples. However, the spot size increases at longer wavelengths resulting in decreased lateral and axial resolution. In nonlinear harmonic generation processes, the induced polarization from the intense incident electric fields generates new frequencies which are not in the spectrum of the incident light. In harmonic generation processes the energy is preserved while momentum conservation may not be required. In the case where momentum is also conserved the wave coupling increases consequently. The momentum conservation is known as phase matching which occurs in nonlinear harmonic signals such as SHG and THG [96]. Nonlinear Schrödinger equation is used to explain the coupling between the incident electric field and the induced polarization which for THG process can be formulated as [97]:

$$\nabla^2 E(3\omega) + \frac{n^2(3\omega)(3\omega)^2}{c^2} E(3\omega) = \frac{(3\omega)^2}{\epsilon_0 c^2} \chi^{(3)}(3\omega, \omega, \omega, \omega) E^3(\omega) \tag{2.2}$$

In which the electric fields at the fundamental wavelength and THG are:

$$E(\omega) \propto A_1 e^{i(k_1 z - \omega t)} \tag{2.3}$$

$$E(3\omega) \propto A_3 e^{i(k_3 z - 3\omega t)} \tag{2.4}$$

In which $k_1 = n(\omega)\omega/c$ is the wave number at fundamental frequency. Using slowly-varying amplitude approximation (SVAA), the solution of the nonlinear wave equation at $z = l$ inside the sample can be expressed as:

$$E(3\omega) \propto {A_1}^3 l sinc(\frac{\Delta k l}{2}) \tag{2.5}$$

In which $\Delta k = k(3\omega) - 3k(\omega) = 3\omega(n(3\omega) - n(\omega))/c$ is the wavenumber mismatch resulting from the dispersion of the refractive index. When $\Delta k = 0$ phase matching condition occurs; however, due to the dispersion of refractive index phase matching does not usually occur. Therefore, the harmonic electric field depends on the sample thickness and oscillates with the period of $\pi/\Delta k$

which is called the coherence length $(l_c)$. Considering the incident wave as a plane wave, the forward and backward coherence length can be formulated as:

$$l_c^{FTHG} = \frac{\pi}{k(3\omega) - 3k(\omega)} \tag{2.6}$$

$$l_c^{BTHG} = \frac{\pi}{k(3\omega) + 3k(\omega)} \approx \frac{\lambda}{12n(\omega)} \tag{2.7}$$

Considering negligible refractive index dispersion. This shows that backward coherence length is smaller than the forward one. For a focused Gaussian wave the forward coherence length can be described as [98]:

$$l_{c,gaus}^{FTHG} = \frac{\pi}{|k(3\omega) - 3(k(\omega) + k_G|)} \approx \frac{\pi}{3|k_G|} \tag{2.8}$$

Where $k_G$ is the Gouy phase shift and can be described as the phase difference between the focusing beam and harmonic plane wave propagation along the optics axis. For strong focusing beam this phase shift is dominant over the material dispersion. Due to the sinc- shape electric field the forward THG (FTHG) and backward THG (BTHG) signals have periodic behavior based on the size of the sample, but BTHG has smaller period compared to FTHG signal. Figure 2.2 below compares the FTHG and BTHG signals for a sphere in a homogenous medium.

Moreover, the influence of NA, dispersion, orientation and incident polarization can be found in [98].

### 2.1.2 MPM schematic

Figure 2.3 shows the schematic design of the MPM using SOLIDWORKS.

The fiber laser delivers the ultra-short pulses at 1550nm and 1040nm excitation wavelengths to the galvo-galvo scanning system. A collimator designed at the excitation wavelength from Thorlabs is used to collimate the laser beam before being deflected by the first galvo mirror (Y). A relay lens system is used to

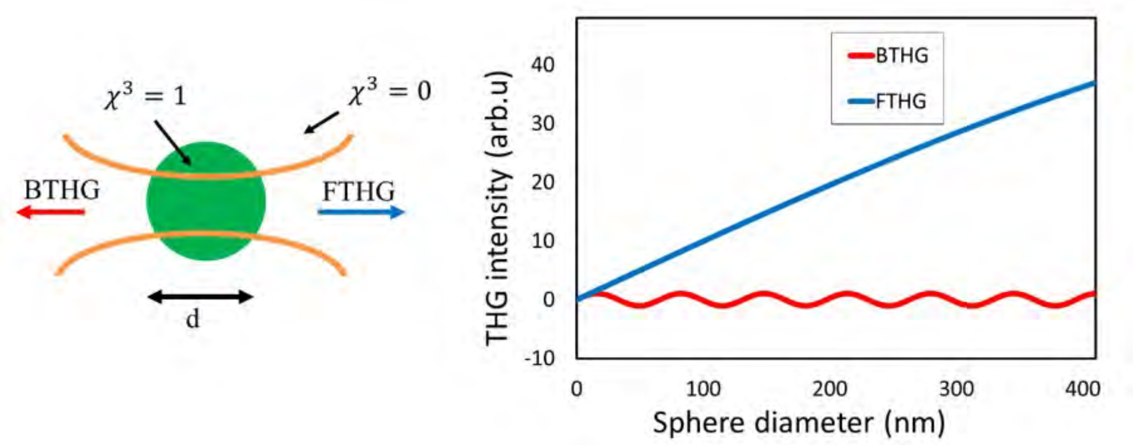

Figure 2.2: THG signal from center of a sphere with different sizes. The graph shows the FTHG and BTHG versus the sphere size and as can be seen the BTHG has smaller period compared to FTHG signal

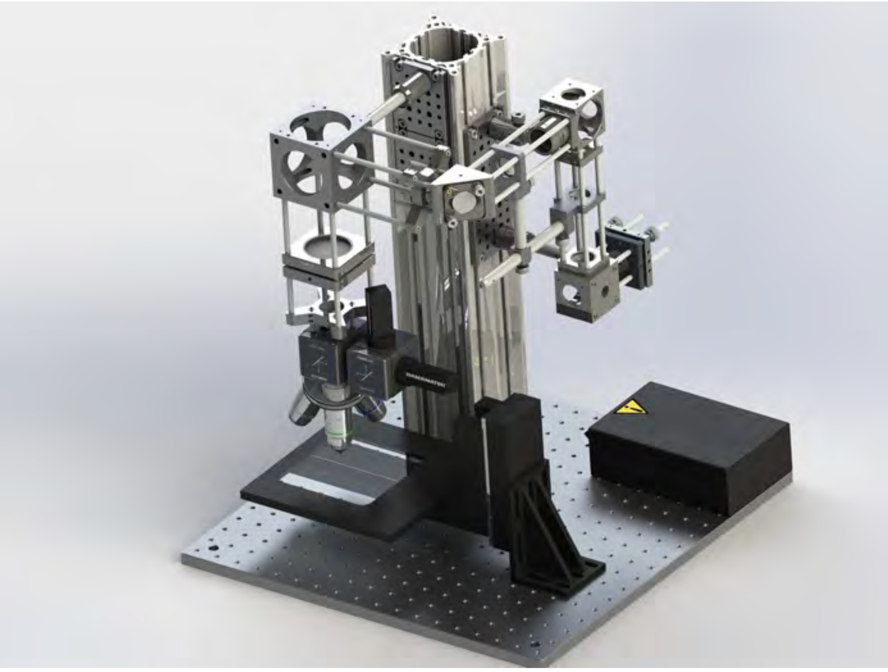

Figure 2.3: SOLIDWORKS model of the MPM (courtesy of Benjamin Cromey)

image the laser beam from the Y-mirror surface to the surface of the second mirror (X-mirror) in order to prevent vignetting in the image. Each element of the relay lens has a focal length of 40mm. The relay lens system has a transmission of 90% using C-coated lenses. A telescope path consisting of scan and tube lenses are used to expand the incident beam to fill the back aperture of the objective lens. The magnification value is defined by ratio of the objective lens back aperture to the collimator size which is here 4 times. Using compound lenses can realize the maximum possible FOV that can be supported by the objective lens. The process of selecting scan lenses and tube lenses are explained in detail in the following sections. A dichroic mirror is used to separate the excitation wavelength from the generated up-converted signal from the sample. The nonlinear multi-photon processes occur at the focal volume of the objective lens where the high photon flux initiates the nonlinear processes. This is why pulsed lasers with large peak powers are typically used in nonlinear imaging. The objective lens has to have good transmission both at the excitation wavelength and the up-converted signal which is normally in the visible region of light. This accompanying with the aberration-corrected design make the objective lenses cost effective and an important element in each MPM system. When sample is excited, the generated light can be collected in forward and backward directions. The harmonic generated signals have larger values in the forward direction due to the phase-matching condition that can be collected using a condenser. However, the forward collection requires a thin slice of the sample and for thicker samples or in vivo application the signal is collected in the backward direction. The backward generated signal is then redirected to the detection unit using the pump/signal dichroic and another dichroic to isolate different spectral regions corresponding to different imaging modalities. The selection of the second dichroic mirror and the filters in front of the PMTs is based on the nature of the signal to be detected. For example, for SHG and THG signals narrow band-pass filters are required, while fluorescent signal needs filters with larger bandwidths. Due to the signal leakage between the channels, it is possible to un-mix the signal using simple algorithms providing that the contribution of each channel through the other one is already known or can be measured. It might be possible to use CCDs for image reconstruction and recording the pixel intensities; however, PMTs are better options due to their sensitivities and their noise performance. The output of the PMTs are then amplified using low-noise current amplifiers before being digitized by an analog to digital (A/D) convertor (NI PCI 6110). The DAQ card has two analog outputs to control the galvo-galvo mirrors and multiple analog inputs. The data acquisition rate can be set up to $5MS/s$ per channel as mentioned in the PCI data sheet. A customized LabVIEW program has been developed to acquire data and construct the images. The data acquisition was synchronized with peripheral devices for 3D imaging. A motorized stage (LSI LXI 4000) is used to move the sample in x, y and z directions. The resolution of the stage is ∼100nm based on the data sheet. It can move 10cm laterally and 2cm axially.

## 2.2 Optical Design

In multi-photon imaging (MPI), it is important that image is reconstructed with minimum amount of aberrations. The aberration can modify the image quality resulting in incorrect interpretation which is vital for in vivo applications. The aberration can be balanced through the optical modeling design using Zemax software. In Zemax, the lenses are loaded into the software using the available library and the distance between the optical elements are optimized using optimization function. The first design prototype includes two achromatic lenses and the objective lens is assumed to be a paraxial surface, since there is typically no information regarding to the optical design of the objective lens. There are several conditions that needs attention to meet the best performance of the microscope. In order to utilize the full NA of the objective lens, its back aperture has to be filled by expanding the incident beam diameter. In the first design, we used a collimator (F280FC-980 and F280FC-1550, Thorlabs) with exit beam diameter of 3.6 mm. The objective lenses we are using for our experiment have 13-15mm back aperture, therefore a magnification of 4 is required. There are different sets of scan and tube lenses with the focal lengths ratio of 4 that can be chosen. However, it is better to use the lenses with larger focal length due to the reduced aspherical aberration. There are two drawbacks on selecting the larger focal length lenses. First, the total length of the system is increased making the system large. Second, since we are using 25.4mm (1inch) lenses, the optical angle scanning range is reduced using a large focal length scan lens resulting in small FOV. For the first design, I have chosen achromatic lenses with 40mm and 150mm focal lengths (AC254-40-B and AC254-150-B, Thorlabs) as scan and tube lenses, respectively. Figure 2.4 shows the Zemax layout and the optical elements.

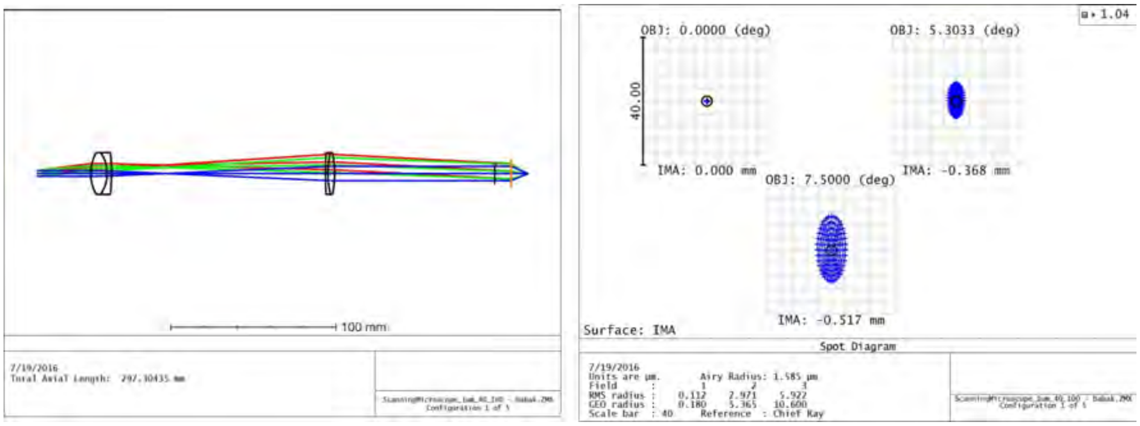

Figure 2.4: Design of the first microscope prototype: schematic and spot diagram for 1040nm illumination

The design was optimized for spot radius and the operating wavelength of 1040nm. The spot diagram was also shown in this figure. The OPD fan nd the field curvature curves for this design are also shown in Figure 2.5.

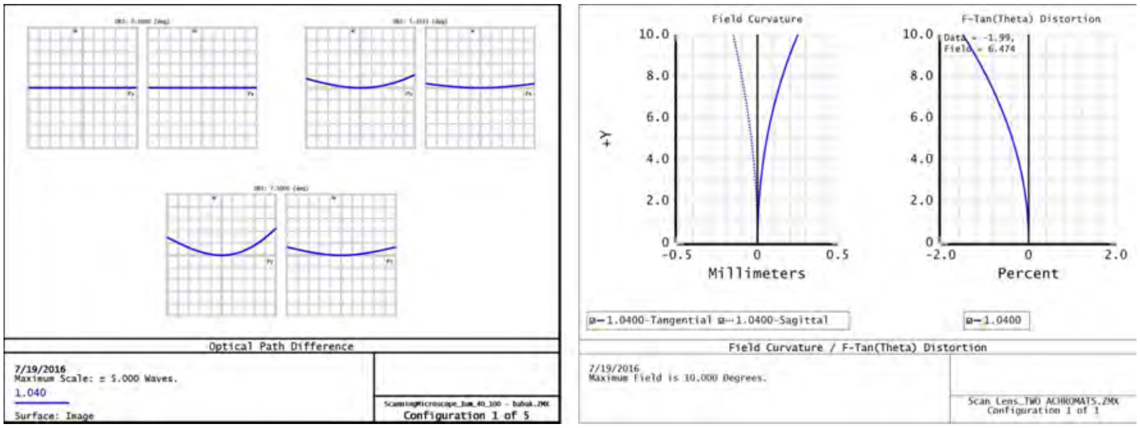

Figure 2.5: OPD fan and field curvature for the first prototype design

This design suffers from astigmatism, distortion and field curvature aberrations. The maximum field curvature and the astigmatism for tangential and sagittal cross sections are 2.07 and 0.88 waves (Figure 2.5). The maximum HFOV by 7.5 optical degrees scanning of the mirrors is 500$\mu$m for an objective lens with 20× magnification and 10mm focal length (Nikon S Fluor, 0.75 NA). As can be seen in Figure 2.4 the system is not diffraction limited for the optical field of larger than 5 degree. Note that, in this design the back aperture of the objective lens was not filled out completely to realize maximum supported NA for the best resolution performance. Considering these issues, I started to design a system using compound lenses instead of single lenses as scan and tube lenses. Each compound scan and tube lens was separately optimized to realize a tele-centric system. The detail of the design will be explained in the following subsections.

### 2.2.1 Tube lens

Instead of starting with scan lens design, it is better to first design the tube lens and based on the required field angle then design the scan lens. There are several criterion that have to be met first to design a tube lens. One is the maximum ray angle exiting the tube lens. This ray angle is defined by the objective lens specifications. Figure 2.6 below shows a schematic of the ideal objective lens and the parameters required to define the entrance ray angle to its back aperture. I mainly focus on two objective lenses mostly used for our experiments. The first one is Nikon 40× with 1.3NA oil immersion. This objective lens has a back aperture of 13mm. The focal length of the objective lens can be calculated as:

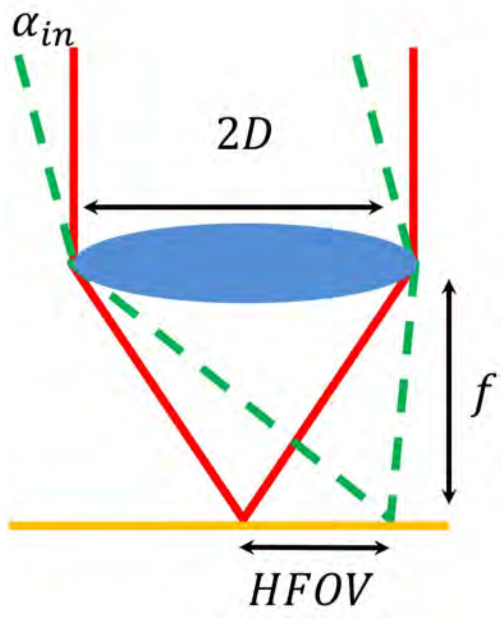

Figure 2.6: Simple objective lens representation

$$NA = n\frac{f}{2D} \tag{2.9}$$

Where $n = 1.52$ is the refractive index of oil. Then the focal length is calculated to be $f = 8.18$mm. The maximum FOV is defined as the ratio of the field number (assuming 20) and the magnification (40×) which is 0.5mm. The incident beam angle is then:

$$2f\alpha_{in} \approx FOV \Rightarrow \alpha_{in} = \frac{FOV}{2f} = 0.03rad = 1.75^{\circ} \tag{2.10}$$

This is the exit ray angle for the tube lens, as well. The entrance pupil in Zemax for the tube lens design was also set to 13mm representing the back aperture size of the objective lens. After examining different sets of scan and tube lenses with the ratio of 4, I decided to use a tube lens with a focal length of 125mm. It is possible to use either a single achromatic doublet with a 125mm focal length or two back-to-back 250mm focal length achromatic doublets. Using two doublets give the software a few degrees of freedom to optimize the aberrations and realizing the image-space telecentricity for the tube lens. Moreover, spherical aberration is reduced 4 times using two achromatic lenses having 2f focal lengths instead of using one doublet with a focal length of f. Figure 2.7 shows the optical layout and the spot diagram using two doublets.

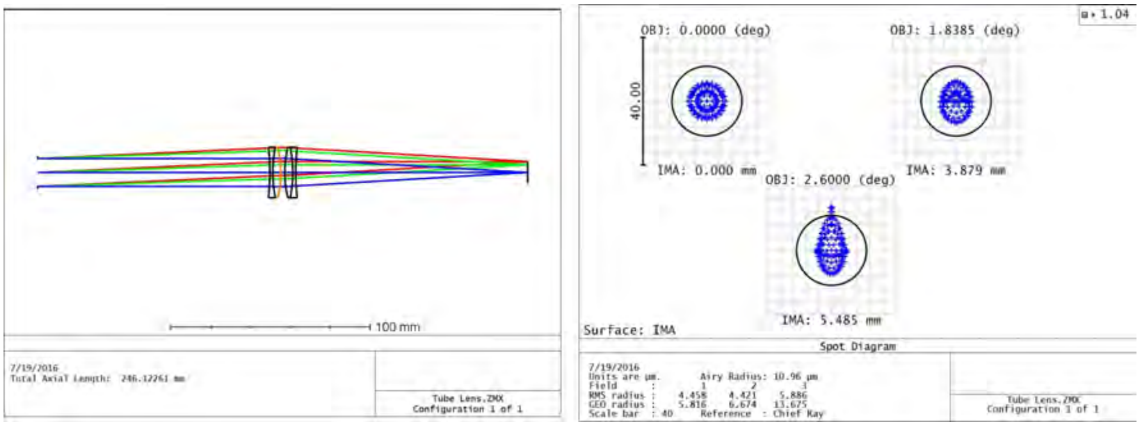

Figure 2.7: Tube lens schematic and the spot diagram for maximum 2.6 degree optical FOV

The incident wavelength was set to 1040nm and I used a Gaussian approximation with an apodization factor of 1. Figure 2.8 shows the OPD fan and field curvature/astigmatism. Note that this is the inverted order of elements in the layout, since the stop aperture was inserted at the first surface.

### 2.2.2 Scan lens

After designing a compound tub lens, a scan lens with a focal length of 30mm is required to expand the incident beam by a factor of 4. It is possible to use

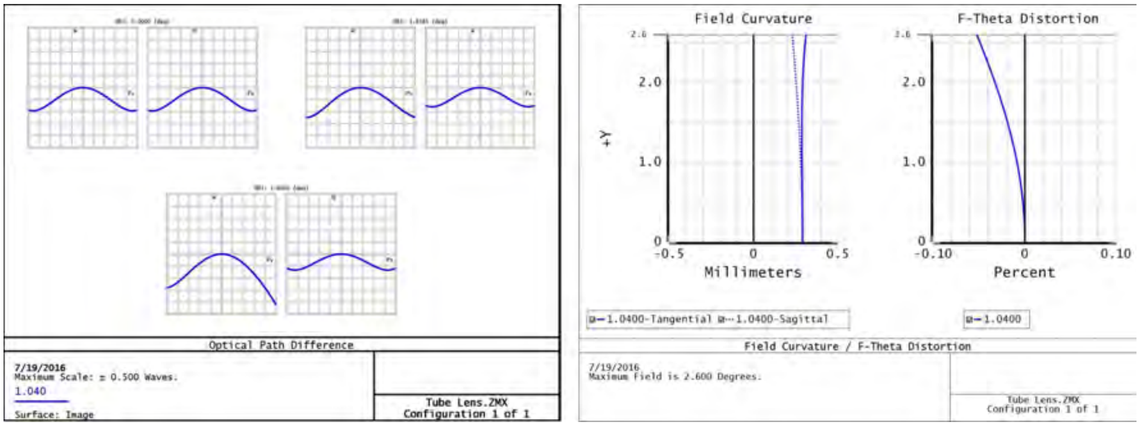

Figure 2.8: OPD fan and field curvature of the tube lens

commercial scan lenses from Thorlabs which are designed specifically for Optical Coherence Tomography (OCT) applications, but they are expensive and are not normally designed for longer NIR wavelengths (i.e. 1550nm). Note that the distance between the first surface of the compound scan lens and the scanning mirror must be larger than 25mm which is the half size of the galvo mirror cage. There are different approaches to designing a scan lens with 30mm focal length and object telecentricity. One can use a single doublet, but by using a single lens we are not able to control the telecentricity. Another approach is to use two back-to-back 60mm focal length doublets followed by a meniscus. As mentioned above using two doublets decreases the spherical aberration. Using meniscus reduced the spherical aberration additionally and let us to control the focal length of the compound lens. Figure 2.9 shows the optical layout of the compound scan lens. In the optimization merit function, I used the operand "RANG" (ray angle) to minimize the chief ray angle for different field angles. Moreover, the distance between the mirror, achromatic and meniscus lenses can be varied in order to reach a 30mm focal length. The whole scan lens design then optimized using spot size radius with 8 rings and 8 arms and maximum glass-air distance of 50mm.

The spot diagram of the compound lens was also shown in Figure 2.9. Figure

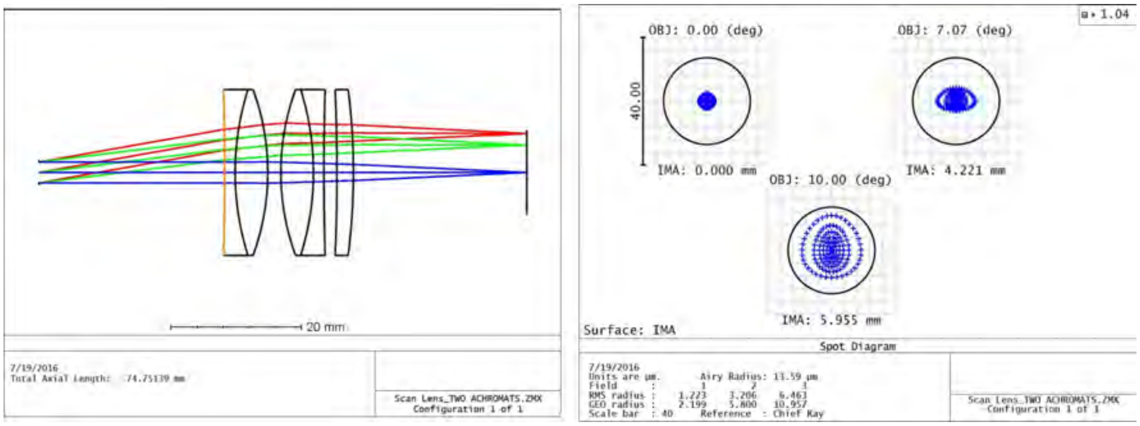

Figure 2.9: Scan lens schematic and the spot diagram for 10 optical degree scanning

2.10 illustrates the OPD fan and field curvature/astigmatism of the design. Back to the tube lens design, the image surface size was calculated to be 6mm which is the image size after the scan lens due to the inverted design of the tube lens.

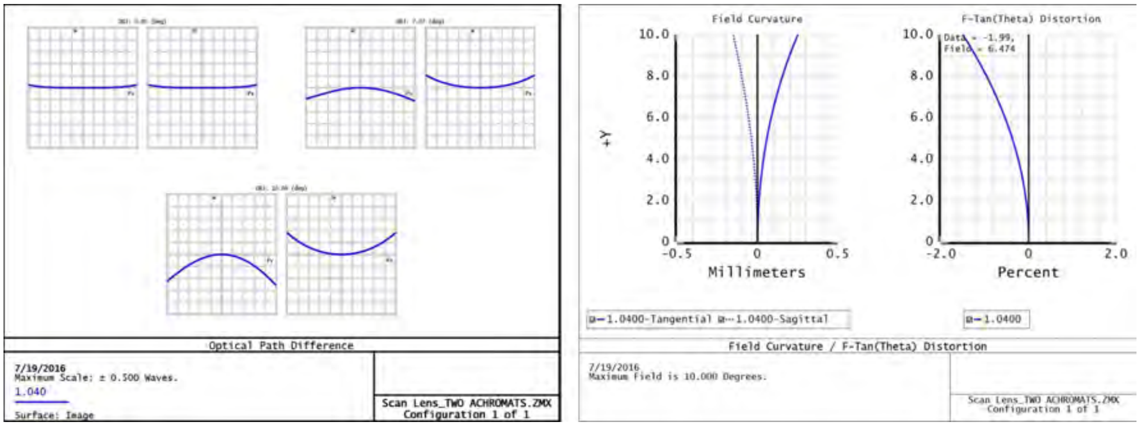

Figure 2.10: OPD fan and field curvature of the designed scan lens for maximum 10 optical degree scanning

### 2.2.3 Relay lens

In typical MPM a galvo-galvo mirror scanning system is used to realize laser raster scanning for 2D image reconstruction. The distance between the mirrors surfaces are typically 1cm. The laser beam is deflected from the surface of the first galvo mirror (X-mirror) before reaching to the surface of the second galvo mirror (Y-mirror). The distance between the first surface of the scan lens and the galvo-galvo system is so that that the mid-distance between the galvo mirrors is considered as the entrance pupil of the scan lens. In an imaging system the image of the laser source has to be imaged on the back aperture of the objective lens. However, the beam should not move laterally on the back aperture but only pivoting around the center of the back aperture. When the galvo mirrors are close to each other, the image of the incident beam is displaced across the back aperture. In order to fix this issue, a relay lens configuration is needed. In a relay lens system, the incident beam is relayed (imaged) on the surface of the second mirror after deflection from the first galvo mirror. Figure 2.11 shows the optical layout of the relay lens system. In a relay system two identical compound lenses are used to maintain a unit magnification as well. For this design, I used an achromatic doublet followed by a meniscus as the relay lens compound lens. This compound configuration was then optimized to make a tele-centric lens system. After the relay lens system, it is important that the different field ray angles should intersect at the same points along the optical axis to maintain the best performance of the following scan and tube lens configuration.

### 2.2.4 Entire optical design

After optimal design of relay, scan and tube lenses, they are sequentially inserted into Zemax lens data and the distances between the lenses are optimized again considering the aberrations that have to be minimized. As mentioned above, a

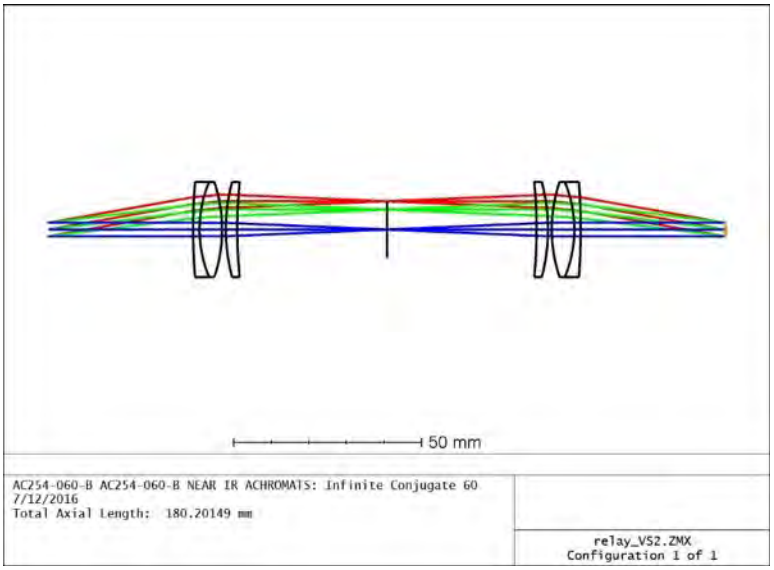

Figure 2.11: Relay lens system consisting of two achromatic lenses with 60mm focal length and two meniscuses with 150mm focal lengths

paraxial surface was used as an ideal objective lens. Figure 2.12 shows the entire design of the optical path.

The spot diagram was also shown in Figure 2.13 indicating the good performance of the system with the proposed design. Distortion has the largest contribution to the aberration existed in the current design. The maximum aberration in OPD fan is 0.4 waves.

The field curvature diagram (Figure 2.14) shows $2\mu$m field curvature aberration. For scanning angles below 8 optical degrees the system is almost diffraction limited. Note that, although the lenses used in this design are B-coated, this design has the same performance using 1550nm excitation source at the cost of a slightly change in the focal plane due to the axial chromatic aberration and 50% transmission loss.

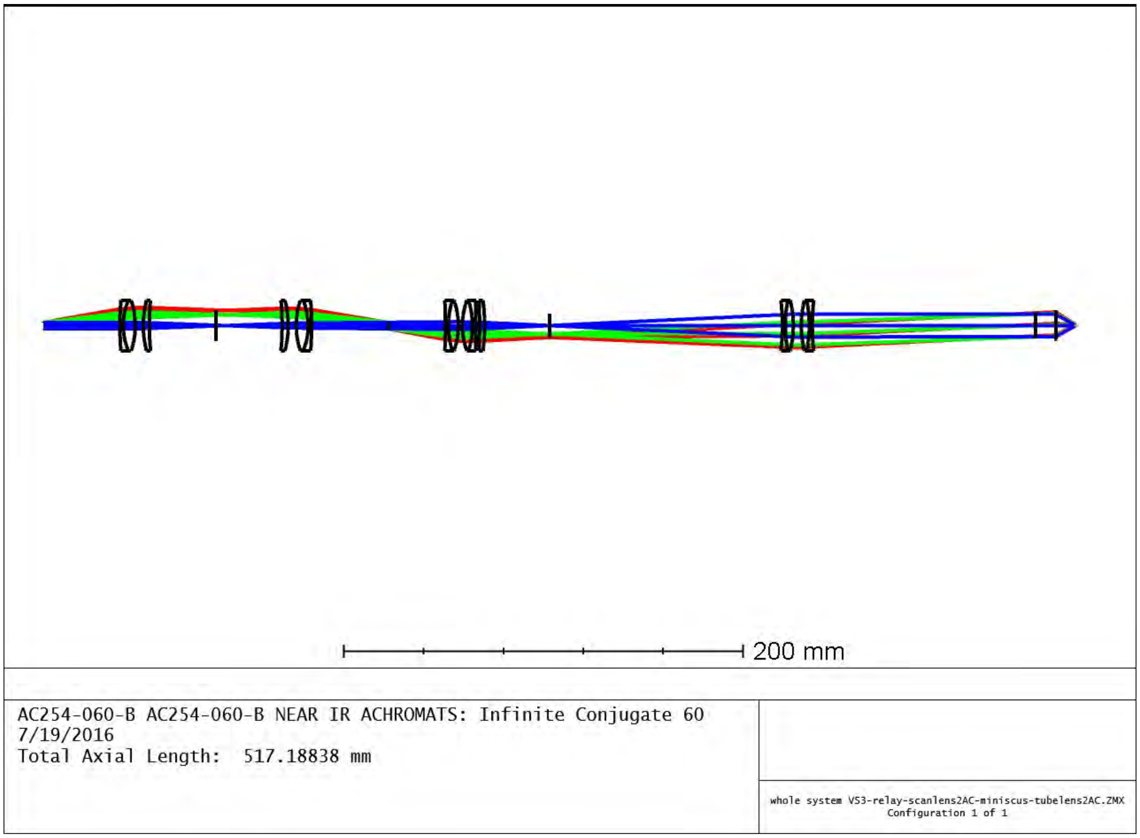

Figure 2.12: Entire imaging system shown for 10 optical degree scanning angle and a paraxial objective lens model

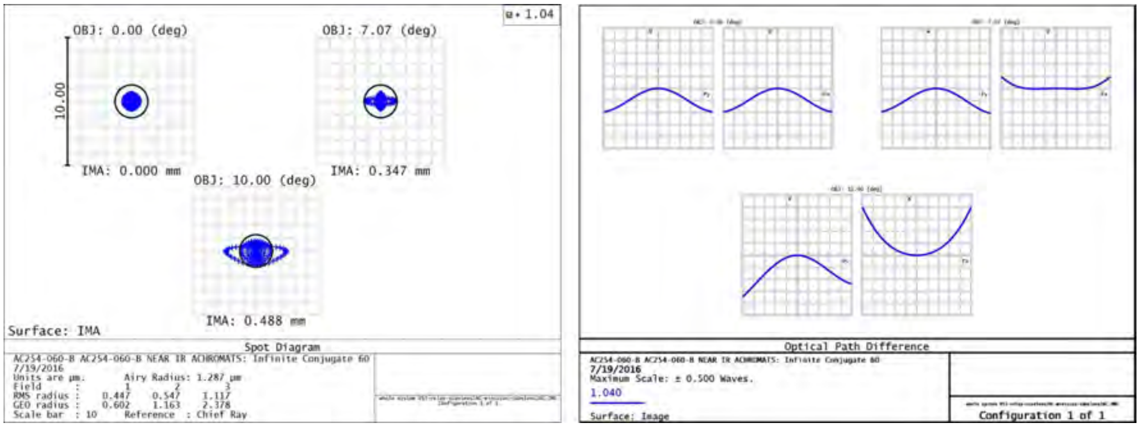

Figure 2.13: Spot and OPD fan diagrams. Note that for 10 optical degree scanning angle, the FOV is $488\mu m \times 488\mu m$ and almost diffraction limited. The OPD fan shows a maximum aberration of 0.4 waves

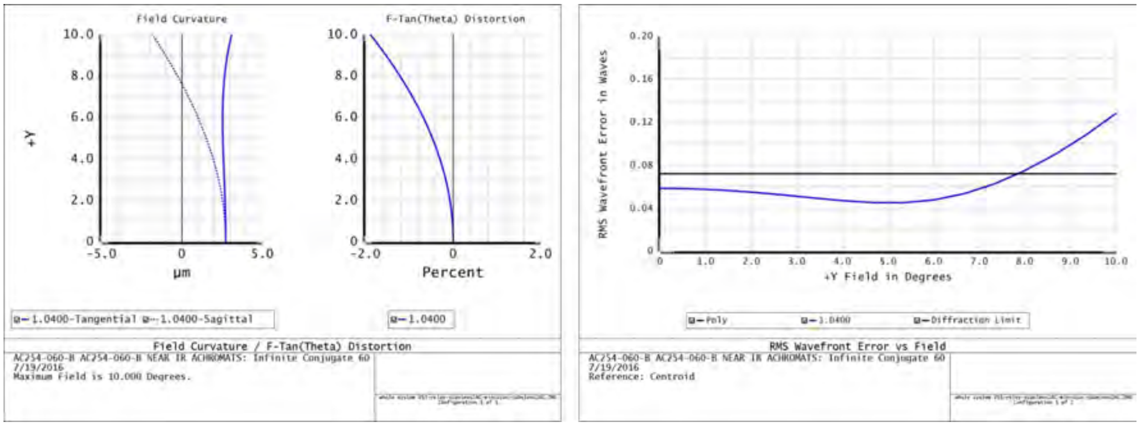

Figure 2.14: Field curvature and f-theta diagrams. The RMS wavefront error vs. field also shows that for optical fields below 8 degrees, the system is diffraction limited

## 2.3 MPM characterization

Multi-photon imaging (MPI) is a powerful nonlinear imaging modality to reconstruct three-dimensional images of objects with high resolution [1, 98]. Multiphoton microscopy (MPM) has a wide range of applications from in vivo and ex vivo imaging of brain [7, 8], cancer detection studies [99], optical characterization of 2D materials [100, 101, 102], photobleaching monitoring of electro-optic (EO) polymers [4, 103], and 3D direct laser writing [104, 105]. The longer wavelength excitation provides deep penetration due to reduced scattering as well as less amount of photodamage and photobleaching out of focal volume. Different MPI modalities such as two- and three-photon excitation fluorescence (2-3PEF), second and third harmonic generation (SHG, THG) and four wave mixing (FWM) can probe different structures of a sample under study. Fluorescence signals may be generated from intrinsic or extrinsic fluorescence agents. SHG signal can be found in structures that the centrosymmetry is broken such as collagen and fibrous structures. On the other hand, THG signal is sensitive to the interfaces where the refractive indices change. It is important to characterize a MPM system in terms of resolution and amount of aberration introduced by the optical elements. The resolution is a measurement of the capability of the imaging system to resolve the smallest possible structures in lateral and axial directions. Moreover, optical aberrations degrade the image quality especially the off-axis aberrations may lead to incorrect image interpretation in laser scanning microscopy. The impulse response of the imaging system to a point source, known as point spread function (PSF), is the figure of merit for spatial resolution measurement. An aberration-free optical system has a perfect Airy-disk PSF and any aberration existed in the system results in distorted and attenuated PSF described by Strehl ratio. The quality and resolution of a confocal microscope was investigated in [106] by interpreting PSF. Young et. al also investigated the effect of spherical aberration induced by refractive index mismatch on MPM resolution [107]. The standard way to measure the lateral and axial resolutions of a MPM is to scan across uniform fluorescence microspheres with defined sizes and examine the capability of the system to resolve the beads [13, 18] .Sectioned Imaging Property (SIP) is a powerful method to measure the axial resolution of a MPM based on the analysis of a stack of image planes of thin fluorescence layers [108, 109]. There are several drawbacks using fluorescent microspheres and thin layers. First, photobleaching and photodamage [110, 111], may occur by exciting fluorescent dyes with high pulse energy femtosecond lasers , a phenomenon that usually occurs in MPI and should be avoided during imaging. Second, the fluorescent samples must be precisely engineered to provide similar microspheres' sizes and uniform thin layers and custom-designed for the excitation wavelength. This process is time-consuming and might be expensive. Finally, for objective lenses with relatively weak transmission at the excitation and emission wavelengths of the fluorescent materials, the poor signal-to-noise ratio (SNR) may lead to inaccurate resolution measurement and characterization. The use of coverslip to embed the fluorescent dyes also limits the application of fluorescent samples to characterize objective lenses and endoscope probes used for cell imaging even though they have been efforts to overcome this barrier with different methods and material developments [110, 111, 112, 113]. Other characterization methods for characterization of linear imaging systems such as knife-edge technique [114, 115, 116] can be developed for nonlinear imaging modalities. In this report, we introduce the nonlinear knife-edge technique based on the back-reflected 2PEF/SHG and THG signals from uniform surface and edge of a GaAs wafer to characterize the MPM. This methodology provides not only information about the lateral and axial resolutions of the system, but also the field curvature aberration introduced by optics and the objective lens. The strong back-reflected signals result in relatively high SNR compared to the signals from fluorescent microspheres and thin layers with no photobleaching effect. Moreover, the use of GaAs wafer allows characterizing the system with or without the cover slip depending on the objective lens used for imaging. This rapid technique is simple with almost no sample preparation and provides persistent information over time. We used this technique to characterize three objective lenses and compared the results with the standard characterization method using fluorescent microspheres and theoretical spot sizes for aberration-free PSFs. Figure 2.15(a) shows the schematic of our in-house designed MPM. We used a mode-locked fiber laser as excitation sources operating at 1040nm with 65mW output power [46, 117]. The laser designed so that the output pulse duration and repetition rate are 100fs and 8MHz, respectively.

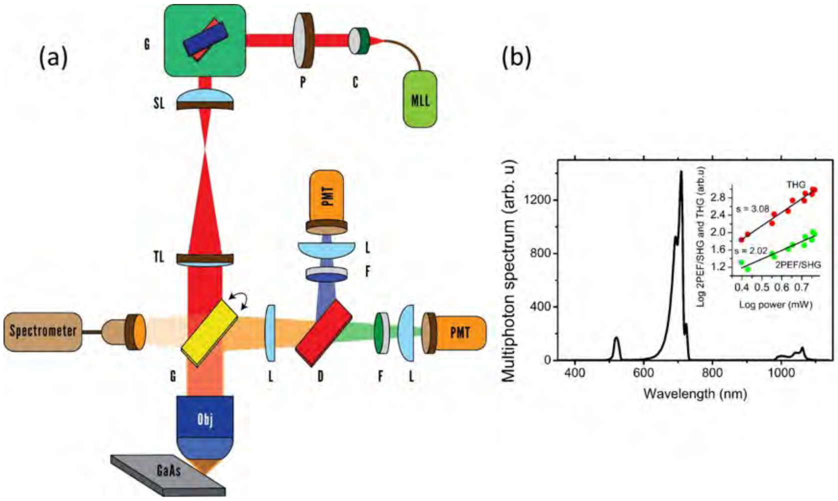

Figure 2.15: (a) Schematic of the MPM used for optical characterization of the system. MLL: Mode-locked laser, C: Collimator, G: Galvo scanners, SL: Scan lens, TL: Tube lens, D: Dichroic mirror, L: Lens, F: bandpass filter, PMT: Photomultiplier tube. (b) Emission spectrum of GaAs using 1040nm excitation wavelength. The power dependency measurements show the two and three photon process indicated by the slopes of 2 and 3, respectively

A reflective fiber collimator (Thorlabs, RC04FC-P01) is used to collimate the laser output with 4mm beam diameter. A 2D galvo scanner (Thorlabs, GVSM002) raster scans the collimated beam in a xy-plane on the sample. A telescope path including scan and tube lenses are used to expand the beam by a factor of 4 to slightly overfill the back aperture of the objective lens to realize the smallest spot size on the sample. A dichroic filter with 870nm cutoff wavelength (Semrock) separates the excitation wavelength and the emitted signal from sample. A second dichroic mirror with a cutoff wavelength at 506nm splits the generated signal into two channels for simultaneous recording. Two PMTs (Hamamatsu, H10721-20 and H10721-110) are used to record different imaging modalities in a non-descanned detection scheme. A band-pass filter at 340/22nm (Semrock) is placed in front of the PMT in the short wavelength channel to isolate the THG signal. The long wavelength channel collects SHG or 2PEF signals by using appropriate filters in front of the PMT. The signals from the PMTs are amplified using low noise current amplifiers (SR570, Stanford Research System) before being digitized by a PCI data acquisition card (NI PCI-6110). A LabVIEW-based software was developed to acquire the data, reconstruct a point-by-point image and synchronize the acquisition with peripherals. A xyz motorized stage (ASI, LXI4000) was used to move the sample laterally and axially. The images were saved as 16-bit TIFF format with user-defined image size and frame rate. In this report, backward SHG/2PEF and THG signals generated from the air/GaAs wafer interface are used to characterize the MPM. A single-side polished GaAs was cut along its lattice direction at one edge for lateral resolution measurement. Figure 2.15(b) shows the 2PEF/SHG and THG intensities versus the laser beam power measured on the sample with the slopes of 2 and 3, respectively. Figure 2.15(b)also shows the multiphoton spectrum of GaAs wafer under 1040nm excitation using Ocean Optics spectrometer (model QE65000). Note that, due to the limited wavelength coverage of the spectrometer (350-1150nm), the THG signal ( 345nm) from 1040nm excitation source could not be shown in the multi-photon spectrum.

### 2.3.1 Lateral and axial resolution using FL microspheres

The conventional method to measure the resolution of a multiphoton microscope is to use fluorescence (FL) microspheres (Invitrogen Focalcheck test slide 1) with defined sizes. Here, we used 0.5$\mu$m diameter microspheres to measure the lateral and axial resolutions of the two and three photon processes with 1040nm excitation wavelength. Each microsphere consists of blue, green, red and far red FL dyes. Figure 2.16 shows the 2PEF and 3PEF images of the microspheres and the corresponding intensity profiles at 1040nm excitation wavelength using 20× Nikon Fluor (0.75NA) as an objective lens. There is no THG signal using 1040nm laser source since the fluorescence microspheres do not emit at 345nm. The Gaussian intensity profile shown in Figure 2.16 can be ideally modeled as the convolution of a Gaussian PSF ($a\exp(-2(x-b)^2/c^2)$) and a rectangular function assuming uniform intensities for FL microspheres. In order to estimate the spot

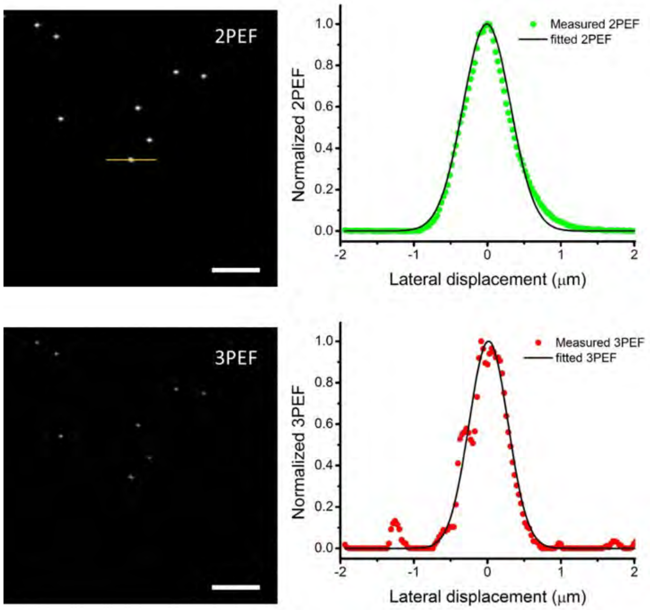

Figure 2.16: Two and three photon images of 0.5$\mu m$ microspheres. The measured data points are fitted with a Gaussian PSF and the FWHM of the PSF is considered as system resolution

size, each intensity profile is fitted against a Gaussian profile with the FWHM of $1.17c/F$ in which $F$ is the convolution factor. This convolution factor can be defined by convolving Gaussian functions with different FWHMs and a rectangular function with 0.5$\mu$m window. The ratio between the original FWHM and the FWHM of the Gaussian profile resulted from the convolution defines F. A look-up table listing the original FWHM, convoleved FWHM and F can be used to extract the original FWHM based on the measured (fitted) FWHM using FL microspheres. In this measurement using Nikon 20× (0.75NA), the lateral resolution for two and three photon processes are measured at 749nm and 608nm, respectively. We also measured the axial resolution of the system by translating the stage with 0.5$\mu$m step size and extracted two- and three-photon intensity profiles in x-z plane. Similar to the lateral resolution measurement, the extracted intensity profiles were fitted with Gaussian PSFs and the FWHMs were considered as the axial resolutions. Note that, one can also use SIPchart plugin available for Fiji [118] and extract the illumination profile and the skew of the z-response across the entire FOV.

### 2.3.2 Measurement of lateral and axial resolution using nonlinear knife edge technique

We developed the nonlinear knife-edge technique to measure the lateral and axial resolution of our MPM. To measure the lateral resolution, the laser beam was raster scanned across the sharp edge of a GaAs wafer and then the reflected signal was collected and a dichroic mirror separated the two- and three-photon processes for simultaneous recording. Figure 2.17 shows the SHG/2PEF and THG images of the GaAs wafer when laser scans across the sharp edge with corresponding intensity profiles extracted from the marked rectangles shown on the edge of GaAs.

In 2PEF/SHG image there is bright line along the sharp edge indicating the

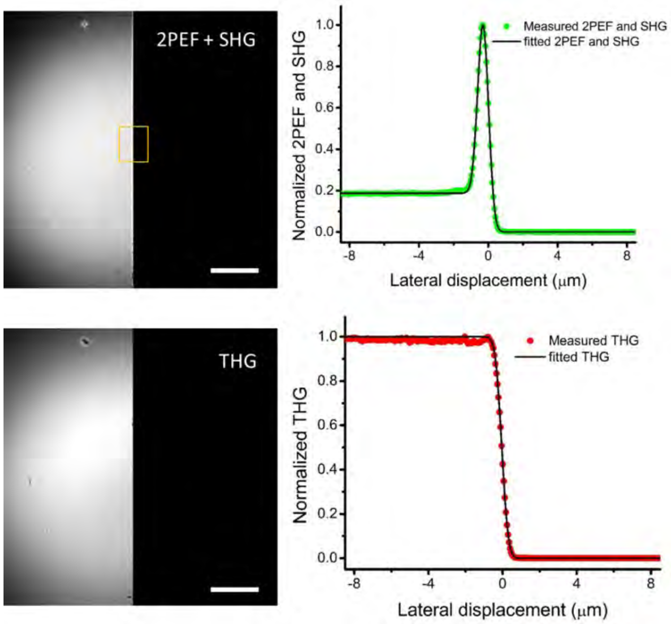

Figure 2.17: Resolution measurement using GaAs wafer. The laser scans across the sharp edge of a GaAs wafer and the two and three photon process resolution is extracted by the curves fitted to the measured data points

broken centrosymmetry when scanning across this area. We modeled this edge as a summation of a step and a delta function representing the bright line. By convolving the Gaussian PSF and the modeled edge profile the back reflected 2PEF/SHG signal can be described and fitted as follows:

$$
\begin{aligned}
f(x) &= ae^{-2\frac{(x-b)^2}{c^2}} * [step(x) + k\delta(x)] && (2.11)\\
&= \frac{a}{2}(1 - erf(\sqrt{2}\frac{x-b}{c}) + de^{-2\frac{(x-b)^2}{c^2}} && (2.12)
\end{aligned}
$$

in which $a, b, c, d, k$ are fitting coefficients and $*$ denotes the convolution operator. Then, the FWHM of the two-photon resolution can be calculated as $1.17c$. Back reflected THG image of the edge was also shown in Figure 2.17. By considering the edge as a step function, the THG intensity profile can be fitted against an error function of $\frac{a}{2}(1 - erf(\sqrt{2}(x-b)/c))$ in which the three-photon resolution can be estimated as $1.17c$. By transverse translating the GaAs edge, the lateral resolution can be measured across the entire FOV. The measured lateral resolution for two and three photon processes are 725nm and 631nm, respectively. Axial resolution was measured by translating the stage ($0.5\mu$m step size) and recording a stack of plane images of the uniform GaAs wafer away from the edge. A z-profile was generated using z-project plugin in Fiji considering a $50 \times 50$ pixels$^2$ region at the center of the images in the z-stack. The z-profile was fitted by a Gaussian profile and its FWHM was considered as the axial resolution of the system for two- and three-photon processes. As mentioned above, SIPchart can be used to visualize different characterization parameters. The theoretical lateral and axial resolutions for two- and three-photon processes were also calculated by following the procedure developed in [1], [119]. The theoretical lateral and axial resolutions can be expressed as follow:

$$
r_{xy}^{FWHM} = \begin{cases} \frac{0.532\lambda_{exc}}{\sqrt{m}NA} & NA \leq 0.7 \\ \frac{0.541\lambda_{exc}}{\sqrt{m}NA^{0.91}} & NA > 0.7 \end{cases} \tag{2.13}
$$

$$r_z^{FWHM} = \frac{0.886\lambda_{exc}}{\sqrt{m}(n - \sqrt{n^2 - NA^2})} \tag{2.14}$$

In which $m = 2, 3$ and n are the order of multiphoton process and refractive index of the immersion medium, respectively. The theoretical values are calculated to be 527nm and 430nm for two and three photon processes, respectively. The theoretical values of lateral and axial resolutions for three-photon process can be derived as following. The intensity point spread function at the focal plane of an objective lens for conventional fluorescence is given by [119]:

$$I_{conv} = |2\int_0^1 J_0(\nu\rho)e^{\frac{-iu\rho^2}{2}}\rho d\rho|^2 \tag{2.15}$$

Where $J_0$ is the zeroth order Bessel function of the first kind. For THG process in focal plane, the lateral intensity is given by:

$$I_{3p} = I_{conv}^3(0, \tfrac{\nu}{3}) = [\frac{2J_1(\frac{\nu}{3})}{\frac{\nu}{3}}]^6 \tag{2.16}$$

Where $J_1$ is a first order Bessel function of the first kind and $\nu$ is the radial optical coordinate given by:

$$\nu = \frac{2\pi}{\lambda} rnsin\alpha \tag{2.17}$$

In which $nsin\alpha$ is NA and r is the radial coordinate. Moreover, $\lambda = \lambda_{exc}/3$ is the THG wavelength. On the other hand, the intensity profile in Equation 2.16 can be approximated by:

$$I_{3p}(0,) = e^{-\frac{\nu^2}{12}} \tag{2.18}$$

Then, FWHM of lateral intensity profile in Equation 2.18 is:

$$\nu_{FWHM} = 4\sqrt{3}\ln 2 \tag{2.19}$$

Finally, the lateral resolution is obtained by inserting Equation 2.19 in Equation 2.17 resulting in:

$$r = \frac{0.53\lambda_{exc}}{\sqrt{3}NA} = \frac{0.31\lambda}{NA} \tag{2.20}$$

Likewise, on the optical axis the axial intensity is:

$$I_{3p}(u,0) = I^3_{conv}(\tfrac{u}{3},0) = \left[\frac{sin(\frac{u}{12})}{\frac{u}{12}}\right]^3 \tag{2.21}$$

Where $u$ is the axial optical coordinate given by:

$$u = \frac{8\pi}{\lambda} znsin(\tfrac{\alpha}{2}) = \frac{4\pi}{\lambda} z(n - \sqrt{n^2 - NA^2}) \tag{2.22}$$

Here $z$ is the axial coordinate and $n$ is the refractive index of immersion medium. The right-hand side expression in Equation 2.22 is obtained by using the identity $sin^2(\alpha/2) = (1 - cos(\alpha))/2$. The intensity profile in Equation 2.21 can also be approximated by [119]:

$$I_{3p}(u,0) = e^{-\frac{u^2}{144}} \tag{2.23}$$

Where its FWHM is given by:

$$u_{FWHM} = 24\sqrt{\ln 2} \tag{2.24}$$

The axial resolution is calculated by inserting Equation 2.24 in Equation 2.22 resulting in:

$$z = \frac{0.918\lambda_{exc}}{\sqrt{3}(n - \sqrt{(n^2 - NA^2)})} = \frac{1.06n\lambda_{exc}}{NA^2} \tag{2.25}$$

Where we used the approximation of $\sqrt{1 - x^2} = 1 - \frac{x^2}{2}$, for small values of x or equivalently for small NAs. By comparing the measured spot sizes and the theoretical values, we can observe that there is a good agreement between resolution measurement using FL microspheres and the nonlinear knife-edge technique introduced here. The discrepancy between the measured spot sizes and the theoretical value for an aberration-free PSF can be attributed to the residual aberrations in the system. Here, we used two single achromatic doublet as scan and tubes lenses which will introduce off-axis aberration when not corrected by other refractive surfaces. The objective lens may also impose some degrees of aberration which is not evident for us due to the secret design layout. It is worth mentioning that the 2D galvo scanners also introduces distortion and field curvature due the distance between the galvo surfaces.

### 2.3.3 Field curvature

Spherical aberration (on-axis) can be corrected or at least optimized by employing extra optical elements, stop shifting or bending optical elements. Further, special lenses with different coatings covering a broad range of wavelengths can be customized with minimum amount of aberrations acting as scan and tube lenses in MPM [13]. However, most researchers may have limited budget and utilizing off-the-shelf lenses is the best option for them rather than expensive customization of the lenses. On the other hand, the optical layout of the most objective lenses is a trade secret information resulting in inaccurate optical design of the entire optical system when there is no access to the objective lens layout. This may make the researchers to custom-design the entire optical path including the objective lens using off-the-shelf and customized lenses [15] which is a time-consuming and expensive process and degrades the throughput of the system when using multiple refractive elements. Off-axis aberrations existed in laser scanning microscopy degrade the image quality and lead to no uniform imaging performance throughout the entire FOV. Field curvature is an off-axis aberration in which different field angles focus on different image planes creating a curved surface (Petzval surface) rather than a flat image (Figure 2.18). This may be problematic for samples in which the exact location of a desired structure in axial direction is required. Since the curvature of the Petzval surface depends on the curvature summation of the individual refractive surfaces and the refractive indices of the glasses, one can minimize the field curvature aberration by using negative and positive lenses in the optical path. It is worth mentioning that in the presence of astigmatism aberration, the field curvature has asymmetrical shape in sagittal and tangential planes.

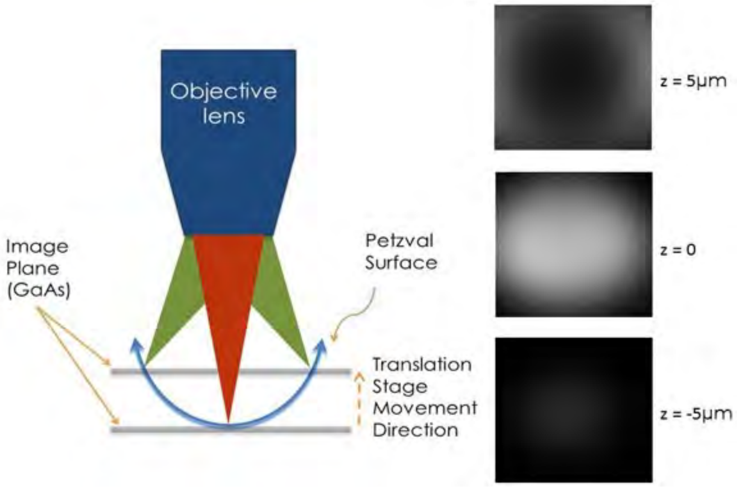

Figure 2.18: Left: Schematic diagram of the objective lens field curvature (Petzval surface). Right: THG signal generated from the surface of the GaAs wafer when its location is below (down), at the focal plane (middle) and above (up) the focal plane

We measured the Petzval curves for three objective lenses. Figure 2.19(a) shows the curves for an aspheric lens (Newport, 5724-H-C, 20×, 0.5NA), Olympus 40× (0.7NA) and Zeiss 50× (0.75NA) at 1040nm excitation wavelength. Figure 2.19 also shows the xz- and yz-plane cross sections (sagittal and tangential planes, respectively). The cross sections are fitted against second-order polynomials as expected for quadratic field dependent astigmatism and field curvature aberrations.

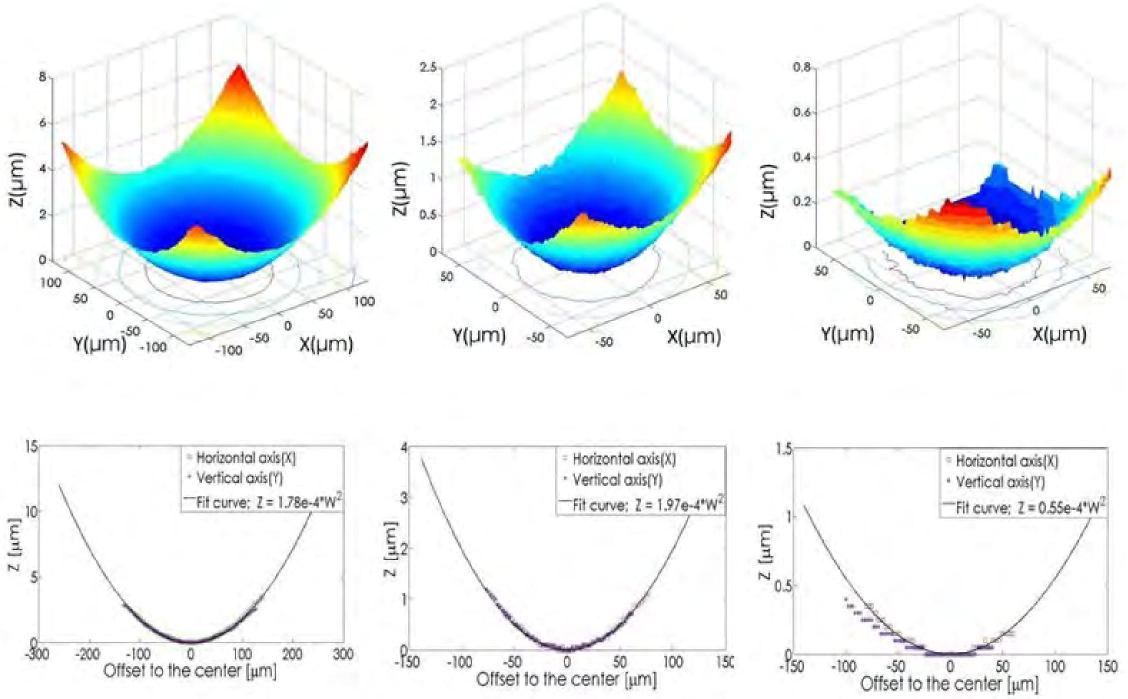

Figure 2.19: Top row: Objective lenses field curvatures for 20× aspheric (Left), 40× Olympus (Middle) and 50× Jena Zeiss (Right). Bottom row: projected Petzval surfaces in top row onto xz- and yz-plane. The projected curves are fitted by a quadratic curve showing the quadratic field dependency of field curvature

By measuring the field curvature and the quadratic coefficients defined for each objective lens, one can correct for the field curvature introduced by the imaging system. Figure 2.20 shows the THG image of a cover slip before and after aberration correction using the data retrieved for aspheric lens. This correction process can be only applied to samples consisting of discrete surfaces separated by at least the DOF of the objective lens.

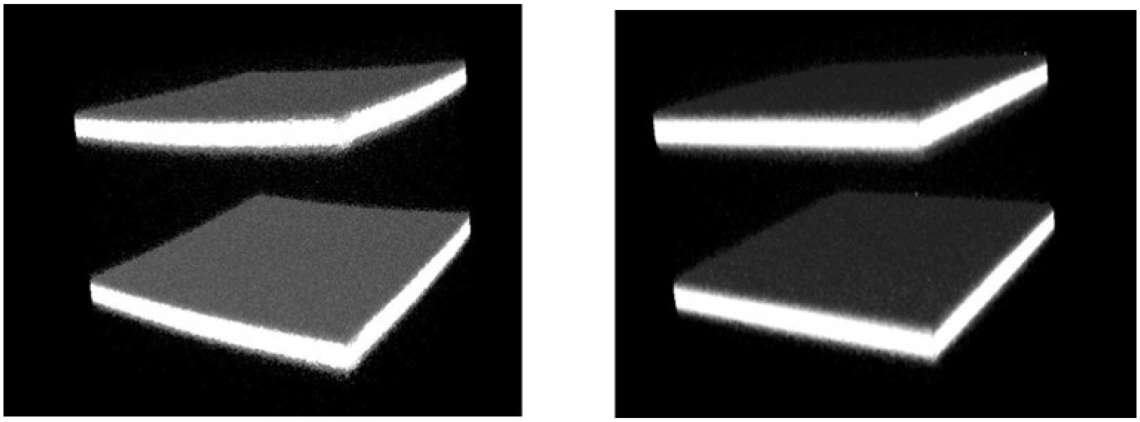

Figure 2.20: Uncorrected cover slip (left) and corrected for field curvature image (right) using the data retrieved by measuring the field curvature for 20× aspheric objective lens

## 2.4 Detection

The detection scheme of the MPM includes a focusing lens, dichroic mirror and passband filters followed by PMTs. The focusing lens is a singlet lens with a focal length of 200mm to collimate the beam coming from the specimen. Another lens with 35mm is used in front of each PMT to focus the collected light to the surface of PMTs. It is assumed that the generated signal is at infinity and the detector surface is at a distance 85mm from the surface of the focusing lens. The dichroic mirror (Semrock) is chosen based on the nature of the signal that we desire to detect. Narrow passband filters are used to filter out SHG and THG signals while wide passband filter are used to isolate 2- and 3PEFL signals. Note that, there are a few lenses inside the system to filter out the excess leakage of pump laser into the detectors (Thorlabs GS900 and Semrock multiphoton filter). Two sensitive PMTs from Hamamatsu are used in our MPM. These PMTs (H10721-20 and H10721-110) are selected with maximum quantum efficiencies for shorter and longer wavelengths in corresponding channels. Both PMTs have almost flat quantum efficiency from visible to NIR. The specifications of the PMTs are shown in Figure 2.21.

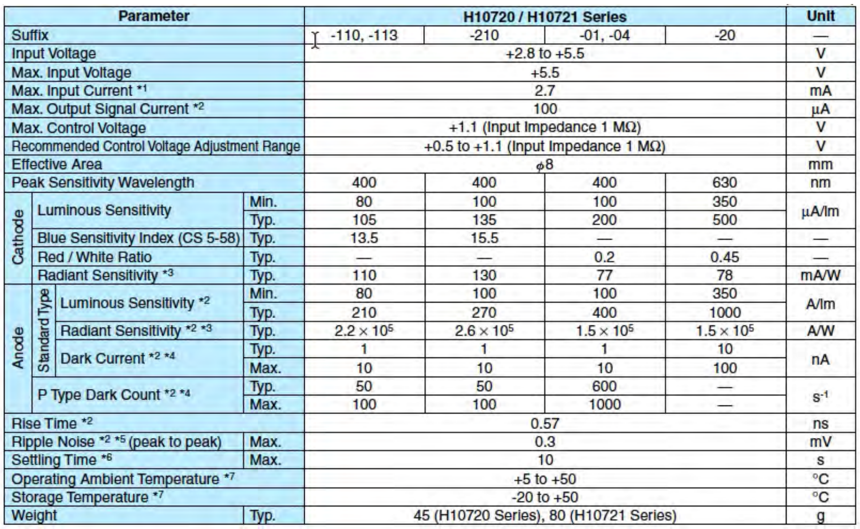

| Parameter | | | | H10720 / H10721 Series | | | | Unit |
|---|---|---|---|---|---|---|---|---|
| Suffix | | | | -110, -113 | -210 | -01, -04 | -20 | — |
| Input Voltage | | | | +2.8 to +5.5 | | | | V |
| Max. Input Voltage | | | | +5.5 | | | | V |
| Max. Input Current $^{*1}$ | | | | 2.7 | | | | mA |
| Max. Output Signal Current $^{*2}$ | | | | 100 | | | | μA |
| Max. Control Voltage | | | | +1.1 (Input Impedance 1 MΩ) | | | | V |
| Recommended Control Voltage Adjustment Range | | | | +0.5 to +1.1 (Input Impedance 1 MΩ) | | | | V |
| Effective Area | | | | $\phi$8 | | | | mm |
| Peak Sensitivity Wavelength | | | | 400 | 400 | 400 | 630 | nm |
| Cathode | | Luminous Sensitivity | Min. | 80 | 100 | 100 | 350 | μA/lm |
| | | | Typ. | 105 | 135 | 200 | 500 | |
| | | Blue Sensitivity Index (CS 5-58) | Typ. | 13.5 | 15.5 | — | — | — |
| | | Red / White Ratio | Typ. | — | — | 0.2 | 0.45 | — |
| | | Radiant Sensitivity $^{*3}$ | Typ. | 110 | 130 | 77 | 78 | mA/W |
| Anode | Standard Type | Luminous Sensitivity $^{*2}$ | Min. | 80 | 100 | 100 | 350 | A/lm |
| | | | Typ. | 210 | 270 | 400 | 1000 | |
| | | Radiant Sensitivity $^{*2\ *3}$ | Typ. | $2.2 \times 10^5$ | $2.6 \times 10^5$ | $1.5 \times 10^5$ | $1.5 \times 10^5$ | A/W |
| | | Dark Current $^{*2\ *4}$ | Typ. | 1 | 1 | 1 | 10 | nA |
| | | | Max. | 10 | 10 | 10 | 100 | |
| | P Type Dark Count $^{*2\ *4}$ | | Typ. | 50 | 50 | 600 | — | $s^{-1}$ |
| | | | Max. | 100 | 100 | 1000 | — | |
| Rise Time $^{*2}$ | | | | 0.57 | | | | ns |
| Ripple Noise $^{*2\ *5}$ (peak to peak) | | | Max. | 0.3 | | | | mV |
| Settling Time $^{*6}$ | | | Max. | 10 | | | | s |
| Operating Ambient Temperature $^{*7}$ | | | | +5 to +50 | | | | °C |
| Storage Temperature $^{*7}$ | | | | -20 to +50 | | | | °C |
| Weight | | | Typ. | 45 (H10720 Series), 80 (H10721 Series) | | | | g |

Figure 2.21: Hamamatsu PMT data sheet and specifications

The gain of PMTs can be controlled using a custom-built electronics housing (Figure 2.22) through a variable potentiometer and 5V DC adaptor. The circuit can provide a DC voltage between 0V to 1.1V required to control the gain of PMTs. The generated multi-photon power is converted to current in PMTs and then amplified using a low noise current amplifier (SR570 Stanford Research) before being digitized by a DAQ card (NI PCI 6110). In order to acquire multi-color image, it is required to change different sets of dichroic mirrors and filters and then co-register the recorded images in post-processing due to slightly movement of the sample through the change of optics.

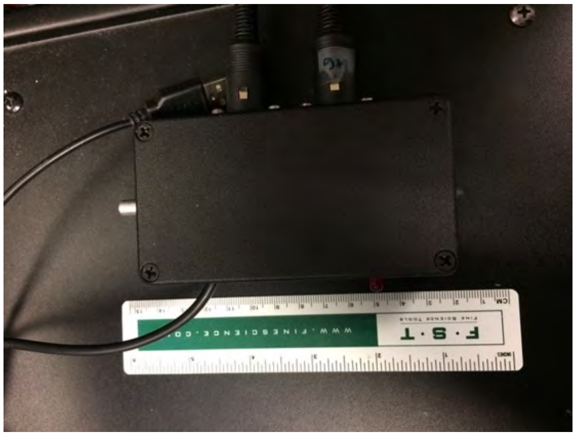

Figure 2.22: Box for controlling the gain of PMTs. A potentiometer controls the gain voltage through a divider circuit. A LED indicates the on and off status

# CHAPTER 3

# MPLAB: LabVIEW based laser-scanning software for multiphoton microscopy

There are a few open source laser scanning software programs which are already developed for two-photon microscopy (ScanImage (NIH), HelioScan). These programs are based on MATLAB, C++ or LabVIEW. However, these programs are customized for defined peripherals such as scanners and translation stages. Therefore, in order to use off-the-shelf electronics and stages, it is required to develop a customized laser scanning software compatible with available instruments. As part of this thesis, a laser scanning software (MPLab) has been customized and developed in National Instruments LabVIEW platform to control the scanning parameters and to synchronize the peripheral electronics. The software is compatible with any peripherals and can be customized for various applications. The working principal of MPLab is similar to ScanImage. The software consists of front panel and block diagram. In the front panel the user can control the image acquisition parameters as well as the stage movement in 3-dimensions. In the block diagram, the main working principal of data acquisition and peripherals' controls are implemented. Below each segments are explained in details and the corresponding front panel and block diagram are demonstrated.

## 3.1 Data acquisition with NI-PCI-6110 using AI and AO ports

In order to perform lateral laser scanning, the beam has to be deflected from two galvo-galvo mirrors realizing a 2D image construction. Here, we used two analog outputs (AO) of the DAQ board to send commands to the mirrors for raster scanning. Sawtooth and staircase patterns were used to implement the x-and y-direction scanning on the sample, respectively. Note that, in the x-direction scanning, the beam is scanning a line on the sample and then returns back to the initial point; however, a dead time has to be allocated to the end of the signal in order to let the mirror start from the beginning of the next line. It is worth mentioning that this dead time should have a smaller slope compared to the slew rate of the scanner preventing a damage on the fast scanner. When the fast axis (x-direction) raster scans a line the slow axis (y-direction) maintains its value on a fixed level. Therefore, the scanning rate of the fast and slow axes are different. Here, we used a fixed 200kHz sampling rate for AO and let the number of writing data points be variable realizing different acquisition times for each line. Consequently, the frame rate can be varied by changing the acquisition time for each line. This value was called "ms/line" in the front panel of MPLab under the "scan" panel. The user can enter different "ms/line" values resulting in different number of data points since the writing rate has been fixed to 200kHz. Equation 3.1 below relates this value to the number of writing points:

$$\text{\#of writing points} = \text{200k samples/s} \times ms/line \tag{3.1}$$

For example, for 8ms/line sawtooth and staircase patterns, signals are generated with 1600 data points. Also, the user can define the number of pixels in each frame by entering the desired number in "lines/frame". As an example, 1000 lines/frame creates a $1000 \times 1000$ pixels$^2$ image corresponding to 8 seconds/frame (i.e. 0.125 frame/s) using 8ms/line acquisition time. Data rate and the number of data points for reading the signal through AI channels are different from AO channels. Note that although the number of points and the rates are different, the acquisition time has to be the same in order to have a correct and synchronized data acquisition. For data reading, the rate was fixed to 2.5MS/s limited by the PC RAM and PCI DAQ card maximum data acquisition rate. Suppose we are going to use 8ms/line for reading and writing. The number of data points that are sampled through the DAQ board can be calculated similar to the Equation 3.1 which is $2.5MS/s \times 8ms = 20000$ points. Since the image size was set to (let's say) 1000, then every 20 points are averaged to represent a pixel. This number is called "bin factor" in the front panel. The data acquisition parameters can be monitored under the "parameters" subpanel. The image acquisition has two modes: Focus and Grab. The Focus mode is free-running image acquisition and real-time display. Grab mode is used for 2D and 3D data acquisition. Focus mode is used when the user wants to find a desired location, adjust the focal plane or find the edges of the sample to start 2D and 3D image acquisition afterwards. Note that in both modes the line acquisition time and image size are controlled by "ms/line" and "line/frame" controllers. The Focus mode controller panel is shown in Figure 3.1 below.

The top line in Figure 3.2 shows the AO writing VIs and their arrangement. A channel is created using "create channel". Then a data rate is defined in "sample clock" VI followed by "Analog 2D DBL Nchannel Nsample" VI and then selecting writing mode. The maximum data values sent to the mirrors were limited to Âś5 V to prevent any damage on the mirrors. The acquisition mode was also set on "Continuous" for real time representation. The second line shows the reading VIs and the arrangement. The reading structure defines the speed of data acquisition and processing. Similar to the writing path, AI channels are created using "create channel" followed by a "sample clock" and reading VIs.

In order to have correct image representation, the writing and reading structures have to be synchronized or run simultaneously. There are two ways to realize the synchronization. Using an external trigger such as square waves which can trigger the writing and the reading processes on the rising or falling edges. This method requires additional wiring or external hardware; however, one can use the PFI port of DAQ card to generate these pulses, too. Another method is to use the AO channel to start the trigger for AI channel. This means that, the read-

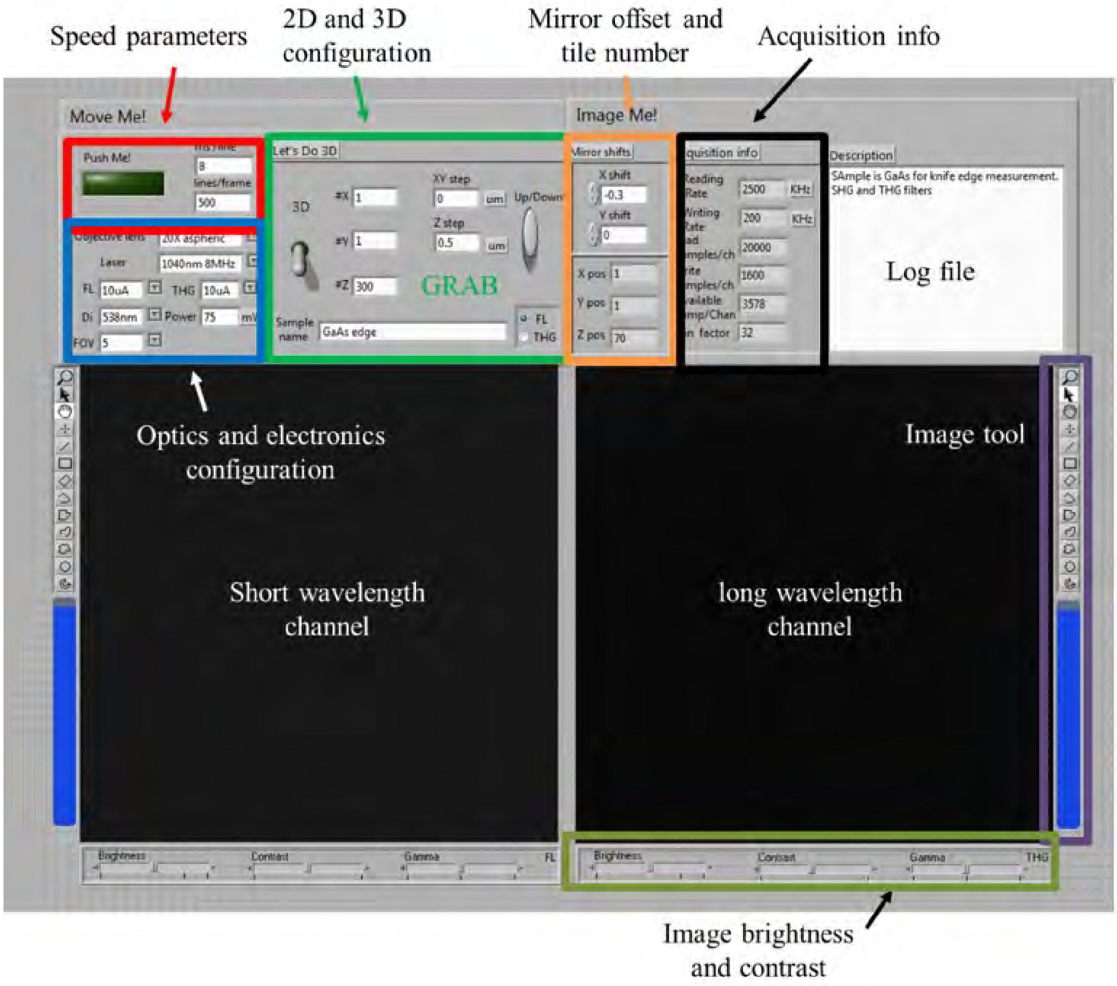

lines/frame 500
Objective lens 20X aspheric
Laser 1040nm 8MHz
FL 10uA
THG 10uA
Di 538nm
Power 75
FOV 5
#X 1
#Y 1
#Z 300
XY step 0 um
Z step 0.5 um
Sample name GaAs edge
● FL
○ THG
X shift -0.3
Y shift 0
X pos 1
Y pos 1
Z pos 70
Reading Rate 2500 KHz
Writing Rate 200 KHz
ad mples/ch 20000
ite mples/ch 1600
vailable mp/Chan 3578
n factor 32

SAmple is GaAs for knife edge measurement.
SHG and THG filters

Figure 3.1: MPLab control panel for image display and acquisition parameters

Writing : sending sawtooth and staircase functions to galvo-galvo mirrors for 2D scanning

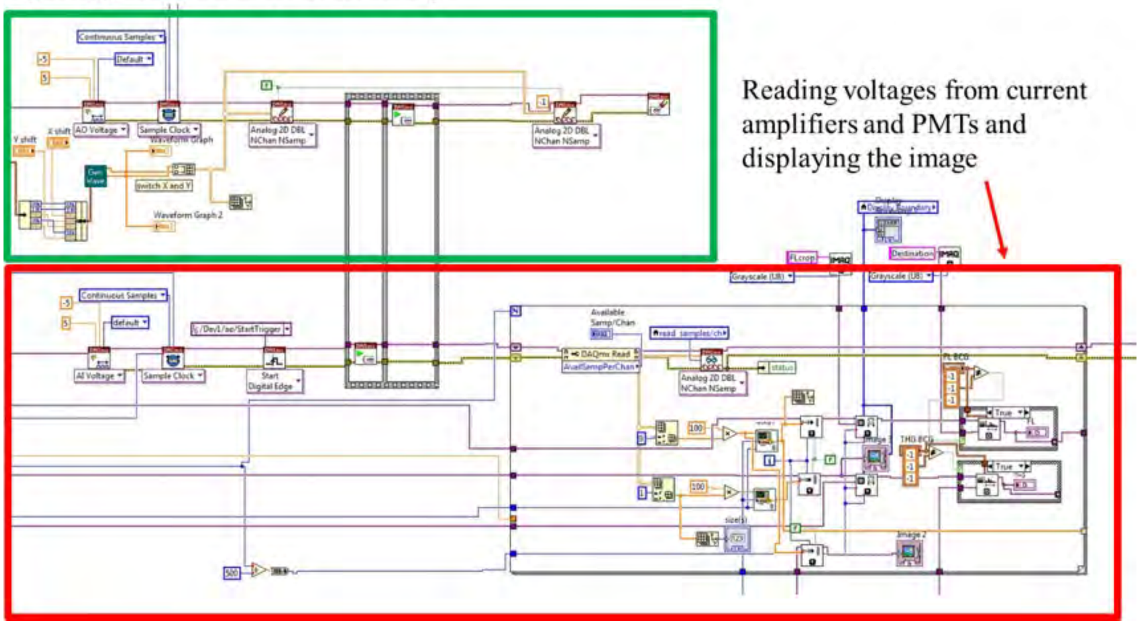

Reading voltages from current amplifiers and PMTs and displaying the image

Figure 3.2: MPLab block diagram for writing and reading the data points

ing starts whenever the writing starts sending commands to the mirrors. This seems the easiest way to implement the synchronization and I used this method in MPLab. In the reading path, a line is read from DAQ board and then loaded into a "picture" display VI. This means that the image is represented line by line. It is much better to show the image in "picture" VI rather than intensity graph due to the large memory usage of a 2D array before transferred to the intensity graph. There are functions to control the contrast of the image. On the other hand, in the Grab mode, the data acquisition is similar to the Focus mode but there are additional functions are added for Grab mode itself. First of all, the image is saved as TIFF format. One can use other image formats; however, TIFF is the most standard one used in image processing. Moreover, in order to capture a 2D or 3D image, multiple frame should be acquired and then stitched afterwards. Therefore, software has to take care of sample displacement in order to cover the whole specimen. This can be done by synchronizing the frame acquisition and stage movement so that the stage is moved just after a frame is grabbed. There are a few issues in image representation that should be corrected before stitching the sequential images. First, the dead time at the end of a sawtooth signal causes a mirror image at the right edge of the image. This mirror image is shown as squeezed replica of the frame. This issue can be addressed by feeding the fast and slow axes different maximum voltages in order to crop the right edge of the image providing that the remained image is still a squared FOV. Second, as the stage is moved to the next frame, a few lines at the beginning of each image are distorted due to the back and forth movement of the stage. One way is to crop these distorted lines from each frame or allocate a waiting time after each frame acquisition to let the stage become completely motionless. Even 50-100ms wait time results in 1-2 minutes longer acquisition time for 1000 frame acquisition. In order to acquire a 3D image, the user has to enter the number of tiles of frames in x, y and z-directions as well as the frame spacing and gap between sequential xy-frames. The frame spacing is normally considered as 90% of the frame FOV allowing 10% overlap between neighboring frames for post stitching the images. The user can also define the direction of axial movement of the stage which is either upward or downward. Moreover, the software can stitch a down sampled ($50 \times 50$ pixels$^2$) of each frame for real-time stitching the sequential frames in order to show the whole sample with lower resolution. This is mandatory and essential for the situations when the user looks for a special feature but it is hard to search for it frame by frame. Figure 3.1 and Figure 3.2 show the front panel and block diagram of MPLab. It is worth mentioning that, one can also call MATLAB inside a VI in order to use better optimized functions at the cost of memory usage. One of common problems with image acquisition is universal naming of the files for saving the images. Since each user prefers his/her own file naming structure, it would be useful to create a platform to save the image files with a unique structure. In this software, the user can select image acquisition parameters such as amplifiers gains, objective lens, laser source, laser power, dichroic mirror and FOV using dropdown boxes. Moreover, the user has to enter the sample name and optionally explain about the experiment and the goal of measurement in a "log info" allocated in the front panel. All these inputs are saved in a ".txt" file in order to be accessible for any user afterwards. The current MPM system has two channels representing lower and longer wavelengths separated by a dichroic mirror. The channels are shown in Figure 3.1. The "picture" VI in LabVIEW provides a built-in toolbar for manipulating or selecting different ROIs and zoom in and out capabilities. When a Grab section is started a folder is created with the sample name and image acquisition parameters. Inside the folder two files representing the channels are generated labeled as FL and THG. Note that, based on the dichroic mirror and the filters in front of the PMTs, these files can be interpreted as other imaging modalities such as 2PEF, 3PEF or SHG. Therefore, the user has to be aware of the nature of the signal he/she is saving. The stage controlling panel is running in parallel to the main loop of data acquisition. This gives the freedom to the user to move the stage during the data acquisition or even lock the movements. The stage movement can move the stage in three x, y and z-directions with the nominal resolution of  100nm. The sample position can also be monitored through the "Where" button. Moreover, the sample can be displaced to a user-defined position using "GoTo XY" and "GoTo Z" buttons. In MPI it is important to first find the focal plane and then move the stage upward or downward to find the desired structures. Besides, one can easily define a position as the origin of the coordinates for exploring other areas relative to the origin. These operations can be done by using "Zero XY" and "Zero Z" buttons. Note that, for 3D image acquisition, it is required to define the coordinates before starting the acquisition. The "Halt" button stops the stages while it is moving. This button can be used whenever the displacement of the stages is going to crash with objective lens or the sample unintentionally.

### 3.2 Image analysis

Most image analysis is performed in MATLAB or using an open source image processing software Fiji (`https://fiji.sc/`). Fiji has built-in functions as well as different plugins that were written and developed by users and can be installed in the software. Although Fiji has a capability of micro scripting in Java, it would be easier to manipulate the images first in MATLAB and then perform image analysis in Fiji. There is another interface called Miji (`http://imagej.net/Miji`) which can be called inside the MATLAB to link the two software platforms while using their strengths at the same time. Fiji is mostly used for stitching the sequential frames and noise reduction filtering. Moreover, it is used for overlapping different imaging modalities with different colors for better visualizations. Besides stitching, the images are analyzed and corrected for FOV efficiency. Due to the non-uniform illumination and ray vignetting the images are not illuminated uniformly resulting in abruption at the edge of the neighboring frames. This issue can be addressed both in software or prior to the image acquisition. One can capture a reference frame of samples with relatively high reflectance prior to image acquisition and then normalized the acquired images by the reference frame. This is an easy method proving that the sample does not have steep tilt resulting in incorrect normalization. The second method utilizes the variation of pixel intensities to generate a reference frame for normalization. This can be done by taking the median of each pixel in every frame and then generate a reference image with the median values. Figure 3.3 below shows 2PEF and THG images before and after FOV efficiency correction for a stained tissue.

The disadvantage of this technique is that for low intensity pixels the background noise is amplified through the normalization, therefore noise filtering is required prior to the normalization resulting in longer time image processing. From uncorrected and corrected images, it is clear that pixels at the edges of each frames are corrected using the median image as a reference frame. This discrepancy is more apparent for THG images. It is also possible to enhance the illumination using "Enhance Local Contrast (CLAHE)" plugin under "Process" tab in Fiji.

## 3.3 Challenges

There are several challenges in the software development. The data acquisition has to be optimized for the simultaneous data writing and reading. As mentioned above, the number of reading data points is usually more than that writing data points. Therefore, multiple data points have to be segmented (bin factor) to realize a squared image size. It seems that if the number of data points be a power of two the segmentation and image display is straightforward. The challenge as-

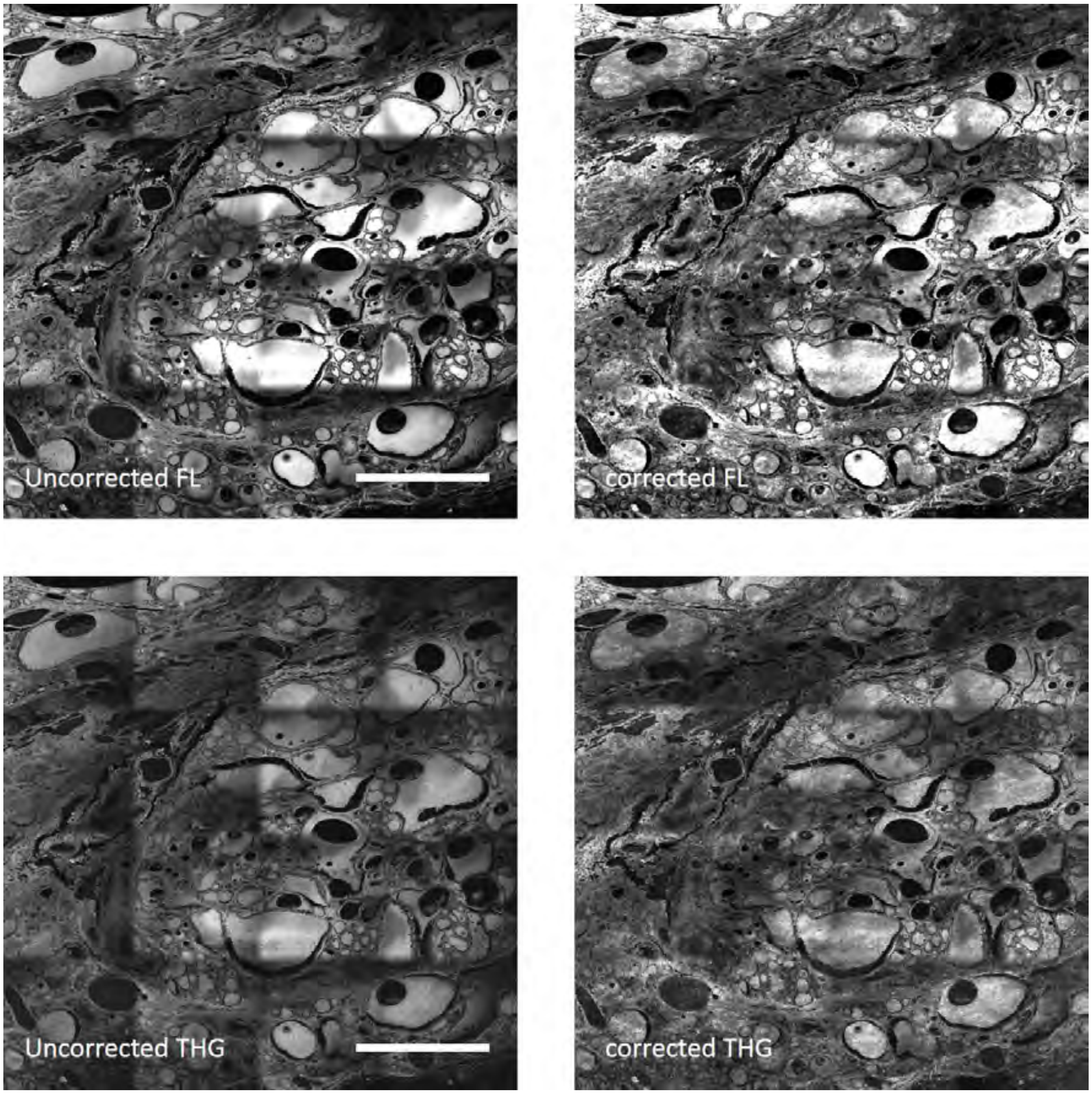

Figure 3.3: nonuniform illumination correction. Left and right columns show 2PEFL and THG images before and after nonuniform illumination correction. Scale bars: $600\mu$m

sociated with this implementation is that for unidirectional sawtooth pattern the X-mirror fly back results in a mirror image at the end of each line data acquisition. However, for fast acquisition time there is a cross talk between a line and the line right after that. It means that a portion of data points at the end of the first line is inserted into the beginning of the second line creating another mirror image. This issue should be solved to have a perfect image without any mirror images. One way is to crop a few pixels from the beginning and the end of each line. However, this may result in a rectangle image rather than a square one. It is also possible to shift each line and put the mirror image either at the end or at the beginning of each line. The consequence of this issue is that the actual line acquisition time is more than the user-defined acquisition time. Note that for large image size, the PC may crash due to the limited size of allocated memory for data acquisition. It is possible to pre-allocate memory for data acquisition and avoid this issue. However, using larger RAM should solve this problem. Another issue in data acquisition implementation is the speed handling. For fast frame rates the amount of defined data points need to be buffered before being read by the card. The more data stays in the buffer, the more possible that software crashes. Therefore, it is required for the fast acquisition time, either the image size or the reading rate is reduced both corresponding to the smaller number of buffered data points. This issue will decrease SNR and the mirror image will probably appear. In MPLab, the maximum frame rate of 2frames/s can be supported for an image size of $512 \times 512$ pixels$^2$ and 2.5MS/s reading rate. This issue has to be addressed for resonant scanning and in vivo applications. The sample size is normally much larger than imaging system FOV. Therefore, for 2D mapping it is require to acquire multiple sequential frames and then stitch them afterwards. In 2D mapping, one frame is acquired and then the stage moves with the size of FOV and this process continues until the entire sample is mapped out. The displacement of the stage has to be such that the small deviation from supposed displacement does not introduce incorrect fusion. Therefore, the resolution of the stage has to be in a reasonable range avoiding this problem. Moreover, in transition between consequence frames, the stage vibrates for a few millisecond before being stabilized. This vibration translates into shaky lines at the few first lines of each image. One way is to consider a dead time after each frame acquisition for stage stabilization. This increases the total acquisition time. An alternative way is to let each frame acquire more than user-defined lines/frame and then crop the few first lines to remove the vibration lines. This means that optical scanning angle should be set larger than the corresponding value of the desired FOV by applying larger voltages to the scanning mirrors. Sometimes, through moving from one frame to the other, the image gets blur or faded due to the system alignment or sample tilt. When the optics are not perfectly aligned along the optics axis the beam has a tilt with respect to the optics axis and the sample resulting in non-uniform mapping. Sample tilt is also unavoidable and one should use a tip tilt stage to compensate for this tilt. Non-uniform illumination of the sample can be a result of imperfect beam or not perfectly aligned optical system. This means that a uniform image has larger intensities at some points compared to the other regions. There are two ways to address this issue. One is to save an image of a uniform sample as a reference image and then normalize each image by this reference image. Another way is to create a reference image in which each pixel is the median of the corresponding pixel in a set of acquired images. Similar to the previous method, the images are then normalized to this median image. This method has been explained above in details. Note that, through the normalization process, the background noise is amplified as well resulting in poor SNR at low intensity pixels.

# CHAPTER 4

# Applications of MPM in bioscience and material characterization

## 4.1 Label-free multiphoton imaging of dysplasia in Barrett's esophagus

### 4.1.1 Introduction

The incidence of adenocarcinoma of the esophagus is rising faster than that of any other cancer in the U.S [120]. An estimated 16,980 new cases and 15,590 deaths are predicted in 2015. More than eighty percent of patients with invasive esophageal adenocarcinoma die within five years of diagnosis [121]. Barrett's esophagus is a complication of gastro-esophageal reflux disease (GERD) where the normal squamous epithelium of the esophagus is replaced by columnar epithelium with goblet cells (intestinal metaplasia); it is the major risk factor for esophageal adenocarcinoma [122]. Barrett's is a common disorder, affecting an estimated 5.6% of adults in the United States [123]. Regular endoscopic surveillance for dysplasia in Barrett's esophagus (BE) is recommended as early identification and therapy of dysplasia and adenocarcinoma has been associated with improved survival [124], [125]. If small foci of intra-mucosal adenocarcinoma can be accurately located, current endoscopic resection techniques can lead to an excellent long-term prognosis, evidenced by the remission rate of 93.8% after a mean follow-up of 57 months [126]. Detection of dysplasia within Barrett's esophagus is difficult, as dysplasia is not visible to the naked eye and is randomly distributed throughout the Barrett's epithelium. High-grade dysplasia and superficial adenocarcinoma can be multifocal, tiny and easily missed [127]. To further complicate matters, there is lack of intra- and inter-observer agreement among pathologists in distinguishing dysplasia from reactive epithelial changes to reflux esophagitis, and in grading the severity of dysplastic change [128][129][130]. Furthermore, islands of Barrett's buried under the normal squamous epithelium have been reported, which can contain or progress to dysplasia or adenocarcinoma [131][132][133]. Buried BE glands are also found to a varying degree under the regenerative neo-squamous epithelium after treatment of Barrett's tissue with radiofrequency ablation and argon plasma coagulation [133][134]. Thus, imaging below the epithelium would be valuable for the identification of buried glands and for their management. Although new techniques are being developed to facilitate image directed biopsies, the current reliance on routine histology delays treatment [135][136][137]. Confocal microscopy can provide microscopic images at endoscopy; however, this requires a contrast agent and current clinical devices do not image tissue well below the surface and are unable to identify buried glands [138]. Optical coherence tomography (OCT) can identify buried glands, but does not have the resolution to facilitate an accurate histologic diagnosis [139]. Auto-fluorescence microscopy under UV excitation can present high-resolution images in order to establish optical patterns for diagnosing dysplasia in BE [140]. Although AF microscopy is a label-free and high-resolution technique for visualization of cellular structures with no need of sample preparation, due to the short excitation the penetration depth is limited to the epithelium preventing to detect buried glands. Multi-photon microscopy (MPM) has emerged as an alternative solution that combines high resolution with the capability of increased imaging depth and short acquisition time [1][141]. Various multi-photon imaging (MPI) modalities such as second harmonic generation (SHG), two- and three-photon excitation fluorescence (2PEF and 3PEF), and third harmonic generation (THG) have been utilized. For instance, the 2PEF signal has been used to study the endogenous fluorescence of normal, pre-cancerous, and cancerous squamous epithelial tissues as well as the associated morphological features [142]. Recently, 2PEF was applied as a probe to characterize the normal esophageal squamous and gastric columnar mucosa biopsy to assess MPM [143]. Moreover, a miniaturized multiphoton probe was developed to examine fresh, unfixed and unstained gastrointestinal mucosa biopsies by using the 2PEF signal [144]. Further, it has been suggested that quantification of the SHG signal from fibrosis can be used as an indicator of epithelial tumor progression [145], [146]. Additionally, THG microscopy is an important label-free technique that can be applied to study a broad range of biological specimens [7][8] [147][148][149][150][151][152][153][154][155][156][157], as the signal is sensitive to interfaces and is able to image inhomogeneous structures where the refractive index changes. By using excitation wavelengths in the 1300-1700 nm range, image depth can be increased due to reduced scattering. It also facilitates the collection and detection of the THG signal. In this report, we assess the feasibility of label-free MPM (at 1560nm) in endoscopically obtained Barrett's tissue and provide herein what we believe to be the first THG images of Barrett's mucosa as well as the first description of thickened basement membrane collagen with neoplastic progression in BE at telecommunication wavelength excitation. The aim of our study is to determine if SHG and THG signals can be used to identify histologic features that can identify Barrett's metaplasia and differentiate between different grades of dysplasia.

### 4.1.2 Multi-Photon Microscopy System

Figure 4.1depicts the schematic diagram of the in-house designed and assembled MPM system [157].

The excitation source is a compact femtosecond fiber laser mode-locked by a carbon nanotube saturable absorber operating at 1560 nm with an 8MHz pulse repetition rate and 150fs pulse duration. The design of the excitation source is similar to that reported in [47]; the difference here is that the laser output is linearly polarized. The laser output is delivered to the microscope via a PM fiber

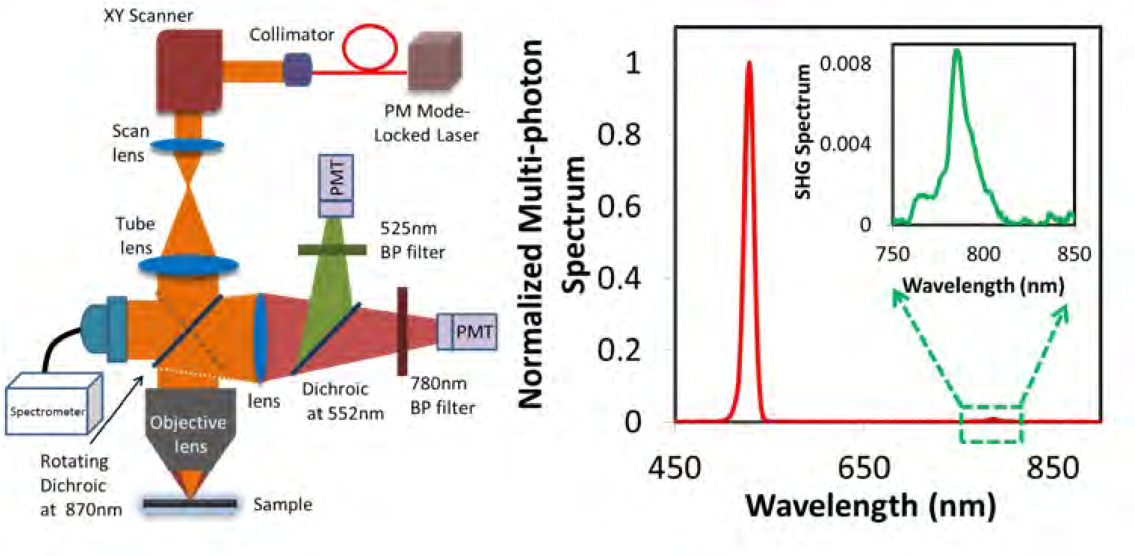

Figure 4.1: Schematic diagram of the in-house MPM system (left) and the multiphoton spectrum of Barrett Esophagus tissue (right). Red: Optical spectrum of the multiphoton generated signal from a normal tissue showing a strong THG signal at 520nm. Inset: zoom-in SHG spectrum

patch cord and is collimated by using a fiber collimator (Thorlabs, F240APC-1550); the collimated beam is then raster scanned on the sample attached to an xyz stage by employing a 2D galvo-scanner system. A telescope consisting of scan and tube lenses expands the beam to approximately illuminate the entire back aperture of objective lens (New Focus, 5724-H-C) so that the smallest possible laser spot size is achieved (THG resolution = $1.3\mu m$, see [157] for resolution measurement). The back-scattered signal from the sample is separated from the excitation source by a long-pass dichroic mirror with 870nm cut-off wavelength. We use a non-descanned detection scheme enabled by a dichroic mirror ($\lambda_{cut-off} = 552nm$, Semrock) and two similar high gain and sensitive PMTs (Hamamatsu H10720-21) for simultaneously recording in two channels. The longer wavelength channel collects the 2PEF, 3PEF or SHG signal by using appropriate filters before the PMT. On the other hand, the shorter wavelength channel collects the THG signal, where a narrow band pass filter centered at 525/30nm (Semrock) was embedded in front of the PMT. Two low-noise current amplifiers (Stanford Research Systems, SR570) amplify the signal generated by the PMTs before digitization by a data acquisition card (NI PCI 6110). In-house laser scanning software based on LAbVIEW was developed was developed to acquire images, control the image acquisition process and adjust the xyz translation stage. Each image frame was acquired and saved with $512 \times 512$ pixels$^2$ and a $250 \times 250 \mu m^2$ (FOV). The frame acquisition time was 8s (pixel dwell time of $\sim 30 \mu s$) with 15mW average power on the sample. Since the FOV was small in comparison to the region of interest, several frames were acquired and corrected for non-uniform illumination. The correction was performed by normalizing each frame by a reference frame outside the region where the sample resides. Finally, the sequentially ordered frames were stitched by using the Stitching [158] plugin in Fiji.

### 4.1.3 Methods and Sample Preparation

Cross-sectional imaging was performed on fixed tissue samples obtained by endoscopy from patients with Barrett's esophagus. Tissue samples were sectioned at $8 \mu m$, stained with hematoxylin and eosin (H&E) and evaluated independently by two gastrointestinal pathologists. Unstained samples were obtained from a section residing 8Âţm below the section used for histology, placed on a glass slide with a mounting medium, and covered with a glass cover slip for MP imaging. Representative samples were classified as Barrett's esophagus (BE) with no dysplasia (51 year old Caucasian male), BE with low-grade dysplasia (75 year old Caucasian man) and BE with high-grade dysplasia (72 year old Caucasian male). The institutional review board of the University of Arizona approved the study.

### 4.1.4 Results

The THG images presented herein (Figure **??**) demonstrate that these label-free images are of sufficient resolution and contrast to depict the histologic features of BE with and without dysplasia that are seen with standard H&E stains. Of interest, the SHG images displayed increasing thickness of the basement membrane collagen with progression of the dysplasia, which is normally not seen in H&E stains, but generally requires specific stains for displaying fibrous tissue [159][160][161]. It should be noted that although obtained from the same biopsy specimen and from the same patient, the multi-photon images are not as an exact a match as the H&E images. Due to the 3-dimensional nature of the tissue fragments suspended in paraffin, sequential $8\mu m$ sectioning of the tissue results in non-identical tissue shapes and sizes, and thus a variation of appearances seen from the same biopsy on separate slides. However, the H&E and multi-photon images depict the same histological features from the same tissue biopsy.

#### 4.1.4.1 Negative for Dysplasia

The THG images (Figure 4.2(e)-4.4(e)) show tissue structure with cell nuclei displayed with high contrast and resolution that is comparable to standard, H&E stained microscopic images. Figure 4.2(a-d) and Figure 4.2(e-h) show the H&E light-microscopic images and multi-photon THG images from a sample of Barrett's without dysplasia. The generation of TH signal from the surface of a microscope slide creates a bright background in THG images. Since the THG signal is phase-matched in the forward direction, the generated forward TH signal is larger than the backward THG signal. To detect this signal, we used a mirror underneath the thin section of the tissue to redirect the forward THG signal to the PMT. As is typical for non-dysplastic Barrett's, the cells are positioned uniformly in a single row along the basement membrane (Figure 4.2(f-h)). The nuclei are of normal size with a normal nucleus to cytoplasm ratio. The cells with no evidence of dysplasia are shown with yellow arrows in Figure 4.2. The SHG images (Figure 4.2(i-l)) show very fine strands of sub-epithelial collagen, which cannot be discerned in H&E images.

#### 4.1.4.2 Low-Grade Dysplasia

Figure 4.3 shows Barrett's with low-grade dysplasia; the cells are not all positioned in a single uniform line and the pattern of the glands remains normal. Nuclei are stratified and mildly hyperchromatic with an increased nucleus to cytoplasm ratio (Figure 4.3(f-h)). These changes are shown with high contrast and clarity in the THG images that depict all the features of the H&E findings. The yellow arrows in Figure 4.3 represent the cells with low-grade dysplasia. The SHG images shows thicker strands of sub-epithelial (basement-membrane) collagen than in Barrett's without dysplasia (Figure 4.2(i-l)). Note that collagen cannot be seen in any of the color H&E images.

#### 4.1.4.3 High-Grade Dysplasia

In Figure 4.4, the H&E and THG images exemplify high-grade dysplasia characterized by marked disruption of the tissue architecture with cellular disorganization. The nuclei are hyperchromatic and pleomorphic, with a greater increase in the nucleus to cytoplasm ratio as well as showing loss of polarity (Figure 4.4(e-h)). Label-free THG imaging with comparable contrast and resolution renders the features of the H&E images. The yellow arrows in Figure 4.4 point to the cells identified as high-grade dysplasia. In addition, the SHG images of the basement membrane show thicker strands of sub-epithelial collagen than in Barrett's with low-grade dysplasia and non-dysplastic Barrett's. Moreover, collagen is not seen in the H&E views.

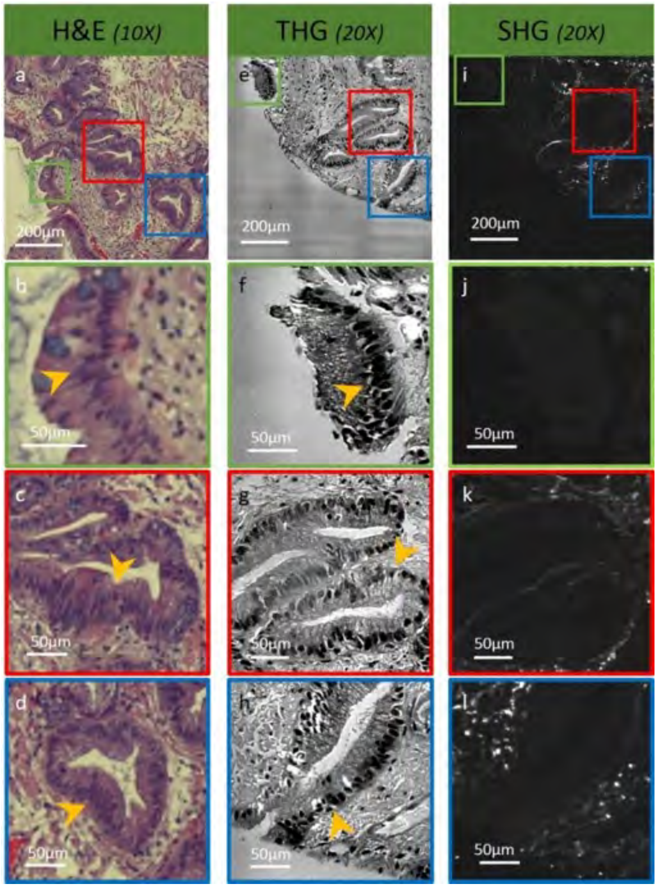

Figure 4.2: Comparison between multi-photon microscopy and conventional light microscopy of BE tissue that is negative for dysplasia. (a) H&E conventional light microscopy image showing intestinal metaplasia with goblet cells. There is surface maturation, low nucle nuclear to cytoplasmic ratio and no dysplasia. (b-d) magnified regions shown in (a). (e) High resolution THG signal from MPM and (f-h) the magnified regions in (e). (i) SHG signal recorded simultaneously with the THG signal showing collagen distribution in the stroma and blood vessels. (j-l) magnified marked regions in the SHG image to show collagen in the basement membrane. The THG signal has a clear correlation to the H&E light-microscope image. The architectural structure of nuclei indicates that the tissue has no dysplastic feature. The yellow arrows show the cells with no evidence of dysplasia. (FOV in (e) and (i): 1000 × 750$\mu m^2$, acquisition time: 2min)

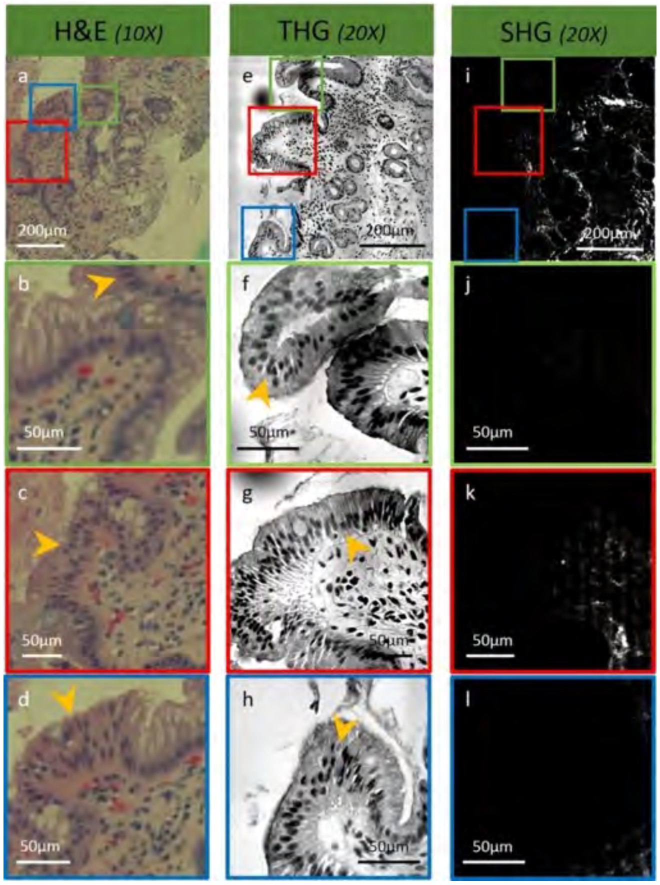

Figure 4.3: Multi-photon and conventional light microscopy images for low-grade dysplastic BE tissue. (a) Conventional light microscopy image of the tissue stained with H&E; there is intestinal metaplasia with goblet cells, surface luminal cells displaying nuclear stratification, hyperchromasia, and an increased nuclear to cytoplasmic ratio (N: C). (b-d) magnified regions marked in the H&E image. (e-h) High resolution THG images that show features of low-grade dysplasia in the same biopsy. (i-l) corresponding simultaneous SHG signals of the THG images that display the presence of collagen. The spatial distribution of cell nuclei is consistent with low-grade dysplasia. The cells with low-grade dysplasia are marked with arrows. (FOV in (e) and (i): $750 \times 1000 \mu m2$, acquisition time: 2min). The vertical white lines in (j)-(l) are the PMT artifacts

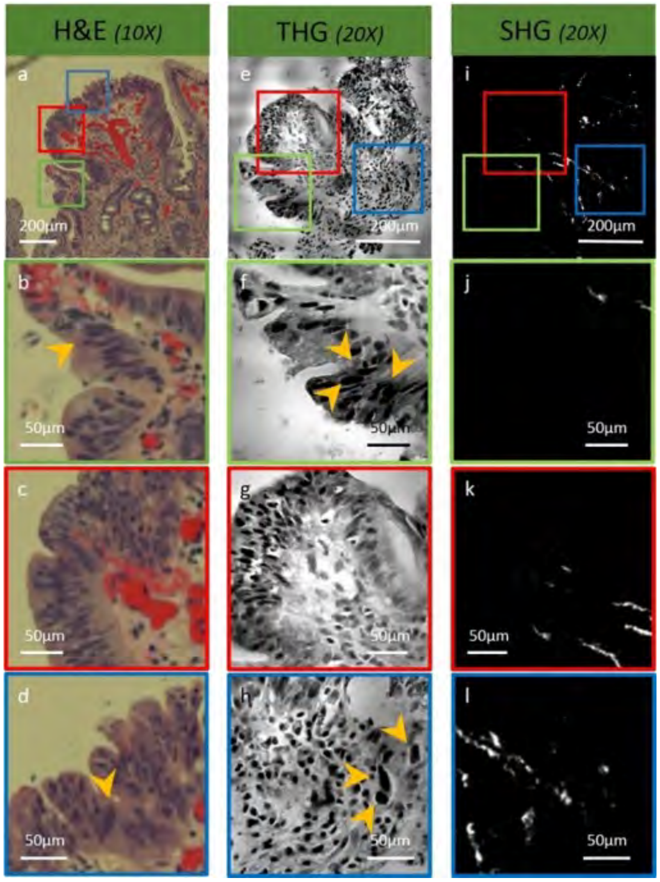

Figure 4.4: MPM and conventional light microscopy images of high-grade dysplastic tissue. (a) Conventional light microscopy image of the tissue after labeling with H&E. There is a progressive dysplastic change in a background of intestinal metaplasia. Cells have marked hyperchromatic nuclei nuclear stratification, loss of polarity and a markedly increased N:C ratio, considerably more than in low grade dysplasia. (b-d) magnified squared regions marked in (a). (e) High resolution THG and (f-h) corresponding magnified regions. (i) High resolution SHG image and (j-l) the magnified regions marked in to show basement membrane collagen (i). The dense nuclei with variable shapes and sizes as well as the loss of orderly arrangement of the cells are consistent with high-grade dysplasia. Arrows represent the cells with high-grade dysplasia. (FOV in (e) and (i): $500 \times 500 \mu m^2$, acquisition time: <1min)

#### 4.1.4.4 Basement membrane collagen

The SHG images acquired simultaneously with the THG images in this study show thickening of sub-epithelial (basement membrane) collagen with advancing stages of dysplasia. Figure 4.5 shows the same SHG images of different stages of the dysplasia shown in Figure 4.2-4.4 when contrast adjusted by using Fiji. In each image (Figure 4.5(a-c)), three areas of sub-epithelial collagen were chosen (A, B, C) and the thickness measured increased progressively with advancing grades of dysplasia, with marked thickening in high-grade dysplasia.

### 4.1.5 Discussion

This initial work indicates the potential of MPM in generating label-free images of Barrett's mucosa with contrast and clarity that is equal, if not superior, to traditional H&E microscopy enabling a histologic diagnosis to be made. Furthermore, the imaging of the sub-epithelial basement membrane evidences increasing thickness of collagen with progression of dysplasia, most prominently in the high-grade form. The increased thickness of basement membrane collagen may represent the body's response to carcinogenesis by attempting to prevent invasion of cells into deeper layers as the disease progresses to cancer. Noting that this observation has been made in a small sample and the findings need to be verified in a larger study, we believe that the implied capability of the SHG MPI to selectively image basement membrane collagen may enable it to become a quantifiable tool for the identification of high-grade dysplasia, which would be of great clinical value. Histological sample preparation and examination by a pathologist to identify the morphological features of a suspicious biopsy in conventional H&E light microscopy are not only time-consuming and burdensome; a diagnosis cannot be made in-vivo or at the point of care. MPM has the advantage of being able to provide high quality images ex-vivo or in-vivo and at the point of care. Fur-

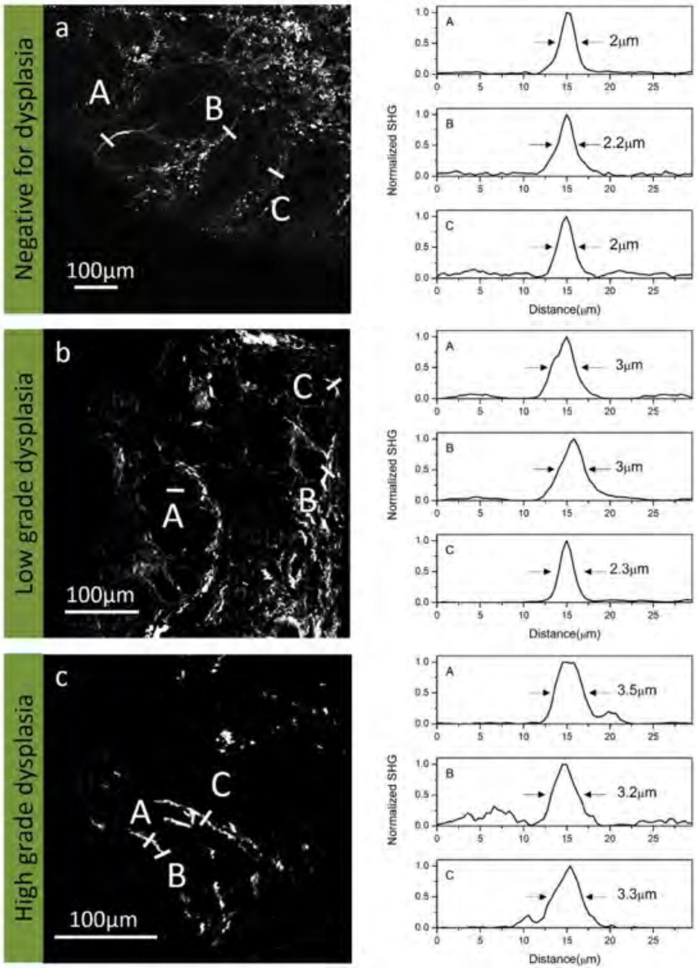

Figure 4.5: SHG signal from Barrett's with non-dysplastic dysplasia (a), low grade dysplasia (b) and high grade dysplasia (c). Corresponding graphs to the right show the thickness of the basement membrane collagen measured at each of the three chosen points per image, which confirm increasing thickness with progression of dysplasia

thermore, MPM should be able to image sub-epithelial buried glands and detect early invasion of cancer in reconstructed 3D images as well as 2D views.

### 4.1.6 Conclusion

We believe these to be the first reported THG images of Barrett's esophagus for demonstration of MPI to identify diagnostic features of low- and high-grade dysplasia in Barrett's. We also report on thickened basement membrane collagen in dysplastic Barrett's epithelium in SHG images, which may prove to be a complementary diagnostic marker of disease stage. Our preliminary results suggest that label-free THG and SHG images may provide not only a substitution for H&E histology in Barrett's, but the future construction of a fiber-optic probe may enable in-vivo detection of unseen dysplasia or cancer during endoscopy and guide therapy, such as endoscopic mucosal resection and radio-frequency ablation.

## 4.2 Multiphoton microscopy as a detection tool for photobleaching of EO

### 4.2.1 Introduction

The photochemical properties of materials are of crucial importance for their acceptance in commercial optical systems. Nowadays, pulsed lasers with high peak intensities are widely used in different optical devices, where the high laser intensities can cause materials to undergo photochemical reactions and remove molecules from the population. This process is called photobleaching and is caused by transitions between excited states of different multiplicity as well as chemical reactions, interaction with the environment and interaction with the excitation light [162][163]. In general, the photostability of a material dictates its suitability for a particular application and molecules with diverse photochemical properties are required for different optical systems. Highly photostable molecules are needed for applications such as optical modulators and switches while materials with a large photobleaching rate are needed for three-dimensional read-write devices [164][165]. Thus, for successful device fabrication it is crucial to characterize the materials' photostability properties to ensure the best device performance and yield. Standard optical characterization techniques such as optical microscopy and Raman spectroscopy [166] are time-consuming and not suitable for rapid characterization in large scale samples. Furthermore, these techniques only indicate a change in materials shape and molecular structure and do not elucidate the bleaching mechanisms. From the discussion above, the need for a better method of understanding the probability and mechanisms of photobleaching of various materials at a specific applied excitation irradiance is clear. Multi-photon microscopy (MPM) is a powerful technique that allows mapping of thin film samples with any kind of optical response such as multi-photon fluorescence (MPFL), second-, and third-harmonic generation (SHG, THG). There are several reports that discuss the measurement of the photobleaching of materials by observing the decrease of the fluorescence intensity using two-photon imaging [110][167][168]. However, these studies are limited only to fluorescent materials. The number of photons involved in the bleaching process can be determined by investigating the bleaching rate versus the excitation irradiance. Many researchers have worked to gain a better understanding of photobleaching in the case of one- and two-photon excitations [169][170]. However, only a few reports are available on photobleaching in the case of three- and more photon excitation [164]. Further, most previous works have been carried out at the wavelengths in the visible range of spectrum which makes it difficult to detect two-, and three-photon ex- citation signals due to the lack of optical components such as lenses and objectives with high sensitivity in the UV regime.

We have in this article successfully employed a multi-photon microscope with a compact femtosecond fiber laser at 1550nm to explore electro-optical (EO) materials suitability in terms of photostability for optical devices such as waveguides. Excitation in the 1550nm band is not only a necessity for telecommunication devices, but also simplifies the detection of second-, and third-harmonic signals due to the existence of high quality optical elements and highly sensitive PMTs in the visible regime. The high photon densities provided from the pulsed laser together with the detection capabilities enable us to utilize various nonlinear optical responses of materials such as SHG, THG, or fluorescence induced by multi-photon absorption for photobleaching studies. This capability significantly broadens the range of materials that can be investigated. Compared to fluorescence detection, THG detection has a large dynamic range and thus larger probing sensitivity. Further, SHG is a beneficial probe for non-centrosymmetric materials with a relatively large second-order susceptibility $(\chi^{(3)})$ as well as for studying the interfaces. To show the capability of our technique, we investigate the photobleaching mechanisms of three well-known EO materials: Disperse Red 1 (DR1), lithium niobate ($LiNbO_3$), and the recently developed EO polymer, SEO250. This method is fast and convenient and can be used for rapid characterization of large scale samples. To our knowledge, this is the first detailed study of the photochemical properties of EO materials in the telecommunications range near 1550nm.

### 4.2.2 Experimental setup

The experimental configuration is depicted in Figure 4.6.

The light source in the MPM system is a femtosecond laser beam at 1550nm. The repetition rate and duration of the pump source is approximately 75MHz and 150fs, respectively. In [47], Kieu et al. have reported the design and performance of the fiber laser source in more detail. The input femtosecond laser beam is raster- scanned on the sample using a 2D galvo scanner system. The beam is relayed and expanded with a scan lens and a tube lens arranged in a telescopic scheme. The back aperture of the objective is fully illuminated to make use of

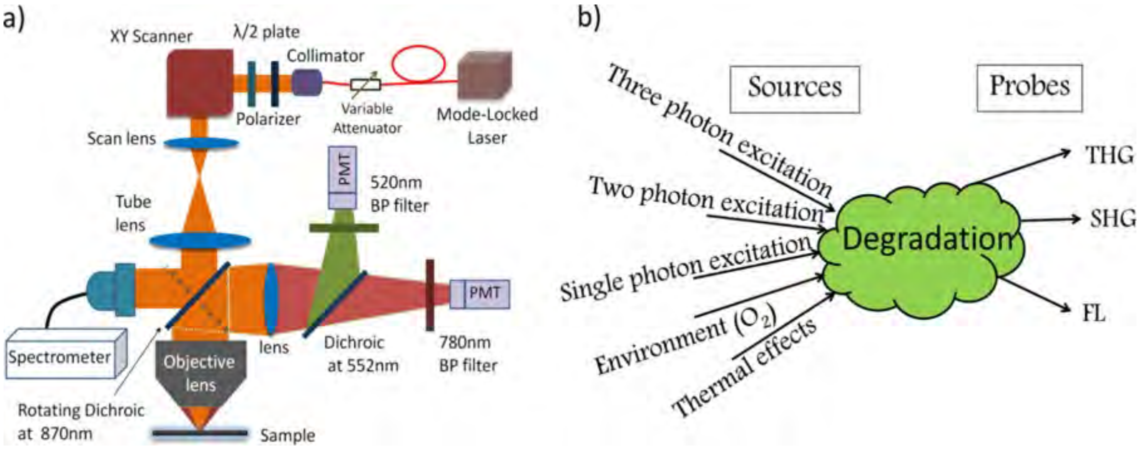

Figure 4.6: The schematic of the multi-photon microscope, and b) diagram showing various sources and probes on materials photodegradation study

the full NA (NA=0.5, 20× aspheric objective lens) and create the smallest possible laser spot size on the sample (confocal parameter=7.2$\mu m$, spot size=1.4$\mu m$). The backscattered signals are detected simultaneously using two highly sensitive high gain PMTs through a series of dichroic beam splitters and filters. A narrow bandpass filter ( 20nm FWHM bandwidth) is used before each of the PMTs to detect the SHG ( 780 nm) and THG ( 520 nm) generated from the laser focal spot. The fluorescence due to two- or three-photon excitation can be measured by removing the 780nm bandpass filter from the transmission path of dichroic mirror. The generated multi-photon signals can also be detected with a sensitive spectrometer with the use of a rotating dichroic mirror at 870nm. The diagram shown in Figure 4.6(b) demonstrates the main mechanisms (single-, two-, and three- photon excitation, photo-oxidation and temperature increase) involved in material degradation when pulsed lasers with high peak intensities are used. It further shows the various probes that can be utilized by our MPM system to study material photobleaching, among which the FL emission is the most studied probe so far. As explained above, with the various probes available, we have the capability to study the photostability of a broad range of materials needed for various applications.

### 4.2.3 Results and discussion

#### 4.2.3.1 Lithium niobate

In this section, we use lithium niobate ($LiNbO_3$) which is a highly stable (thermally, chemically, and mechanically) ferroelectric crystal to understand the uncertainty of our experimental measurements. $LiNbO_3$ has many applications in photonic devices due to its high nonlinear optical coefficients and a broad visible and infrared transparency. Properties and applications of $LiNbO_3$ have been widely studied resulting in several excellent review papers on this material [171][172]. One of the significant applications of LiNbO3 is for electro-optic modulation. Further, $LiNbO_3$ has a significant SHG coefficient due to its non-centrosymmetric crystal structure. Thus, we use the SHG signal of $LiNbO_3$ as a probe to explore its photostability and the uncertainty of our multi-photon imaging system. The multi-photon spectrum of the $LiNbO_3$ sample excited at 1550nm is shown in Figure 4.7(a). As expected, the sample shows a strong SHG signal around 775nm. Figure 4.7(b) demonstrates the normalized SHG signal of the sample continuously irradiated with various powers of the laser (0.5, 1.5, and 2.5 mW average powers) for 3 minutes. As shown, the decay in the SHG signal is less than 2% over 3 minutes of the exposure time. The potential mechanisms that can contribute to the observed decay are material photobleaching, stage drift which moves the sample from the focal plane, laser pump power and polarization drift, among which the stage drift has the largest contribution. The independence of the slight decay in the SHG signal of the input power suggests that the drift is not due to material photobleaching. Further measurements show that the drift in laser power is on average 0.5% of the set power. Other mechanisms such as dispersion of lenses in the system and the drift in the laser polarization have negligible effects on the measurement results.

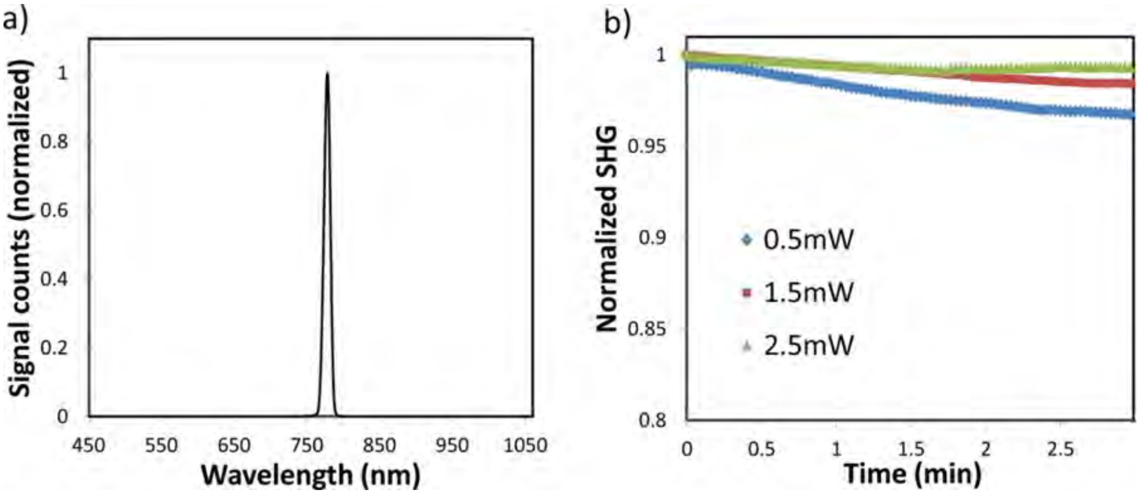

Figure 4.7: $LiNbO_3$ multiphoton spectrum excited at 1550nm, and b) normalized SHG intensity versus laser exposure timing for various laser powers

#### 4.2.3.2 Disperse Red 1

Disperse Red 1 (DR1) is an EO chromophore well-known for its nonlinear optical properties and applications in EO modulators and switches [173]. It is usually doped in an amorphous polymer to enable the formation of uniform amorphous thin films. In this work, polymethylmethacrylate (PMMA) was used as the host material. PMMA is a common material often used in the fabrication of waveguide devices due to its high optical damage threshold and good stability. DR1 was doped in PMMA as follows: a 6% wt. DR1 solution in chlorobenzene was mixed with 6% wt. PMMA solution in chlorobenzene (1:1 volume). The mixture was stirred at $50°C$ overnight and filtered with $0.2\mu m$ PTFE syringe filters. The solution was spin coated onto the fused silica substrate to make a 150 nm thin film.

The multiphoton spectrum of the sample excited at 1550nm is shown in Figure 4.8(a). Since the sample shows no fluorescence but a strong THG signal (sharp

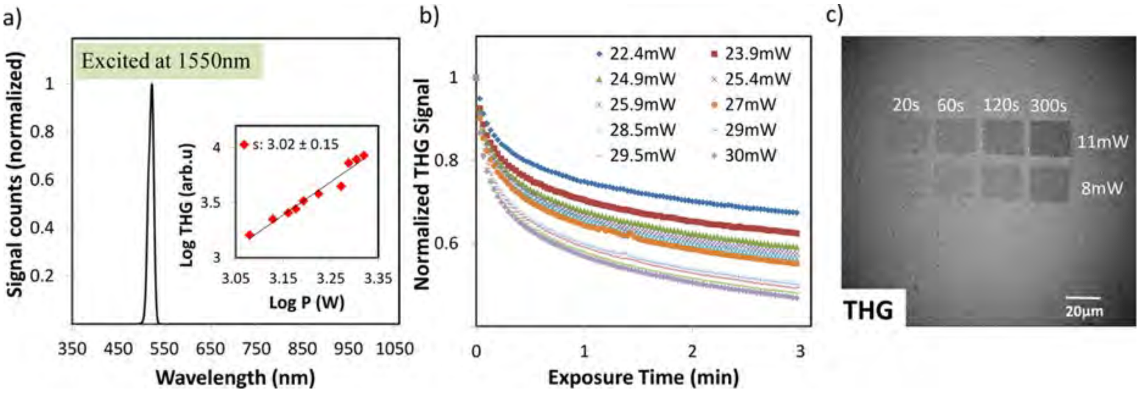

Figure 4.8: Multiphoton spectrum of DR1 on fused silica, the inset shows the log-log plot of the output THG signal versus input power, b) normalized THG intensity versus exposure timing for various laser powers, and c) THG profile of the sample where each square

peak at 517nm), we use THG as a probe to explore the photobleaching mechanism of DR1 (the cubic dependence of the output power on the input pump shown in the inset also indicates that the probe is THG signal). Figure 4.8(b) demonstrates the normalized THG signal reflected back from the sample when it is continuously irradiated with the focused laser beam at 1550 nm for 3 minutes. The THG profile of the sample is shown in Figure 4.8(c) where several areas of the sample ($26\mu m \times 26\mu m$ squares, $512 \times 512$ pixels$^2$) each continuously exposed by various powers and timings of the laser are shown. It can be seen that at very low irradiation power (below 8mW), photobleaching is negligible. However, for excitation peak power values greater than 8mW, the process of photobleaching becomes significant and a decay of the THG is observed. In order to fit our experimental data for THG signal, we tried three different functions: single-, double-, and stretched-exponential. The results of Figure 4.9(a) demonstrate that both double- and stretched- exponential functions could fit the data with good agreement. It should be noted that several relaxation phenomena in complex condensed-matter systems have been found to follow the stretched-exponential decay law. Specially, dielectric relaxation in polymers are usually described as being a stretched-exponential function [174]. Although a large weight percentage of polymer is used in DR1 samples, we chose to fit the experimental results with a double exponential since that would make the interpretation of the two well-known degradation phenomena in DR1 (photo-oxidation and tran-cis isomerization) easier. A double-exponential decay function can be written as [111]:

$$T = T_0 + T_1 e^{-k_1 t} + T_2 e^{-k_2 t} \tag{4.1}$$

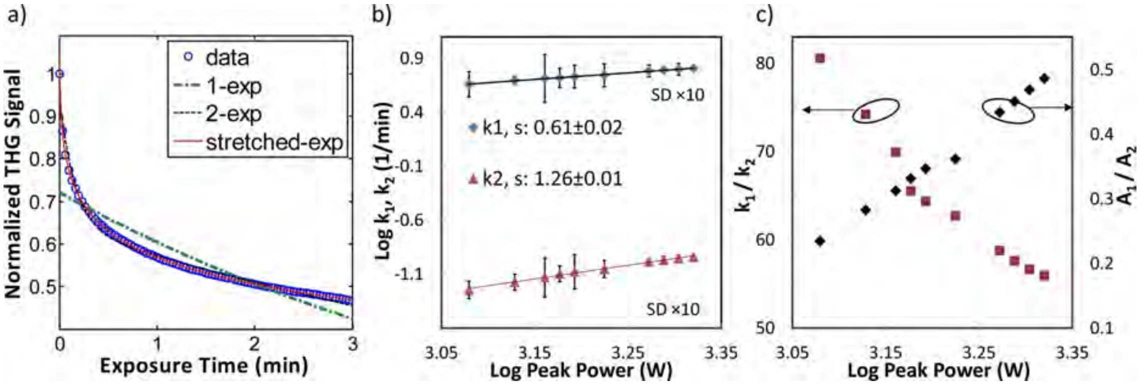

Figure 4.9: DR1 decay curve with 30mW power (circle-marked line), best fitted one- (dash- dotted line), double-(dotted line), and stretched-exponential (solid line) functions, b) log- log plots of the photobleaching rates $k_1$ and $k_2$ vs. irradiation power, and c) the ratio between parameters $\mathrm{k}_1$ and $k_2$ (left axis) and $A_1$ and $A_2$ (right axis) vs irradiation power

In this expression T is the THG photon flux, $k_1$ and $k_2$ are the rates of decrease of THG signal, called here photobleaching rates (1/s), $T_1$ and $T_2$ are the initial contributions to the THG signal from each exponential decay (photon/s), and $T_0$ is a noise constant. The two exponential decay rates in the bleaching function represents two different mechanisms involved in the photobleaching process of DR1. The photobleaching rates $k_1$ and $k_2$ versus irradiation power are depicted in Figure 4.9(b). As can be seen, the slopes of logarithmic plots are 0.61 and 1.26 for $k_1$ and $k_2$, respectively. Hence, the slopes of the photobleaching rates suggest that a one-photon process is the bleaching source for both mechanisms. It is shown in Figure 4.9(c) that the first mechanism associated with $k_1$ is a much faster process compared to the second mechanism $(k_1 \gg k_2)$. On the other hand, the contribution to the THG signal from the two mechanisms is comparable. As mentioned earlier, the dominant degradation mechanisms in DR1 are photo-oxidation and tran-cis isomerization [175][176]. The photo-oxidation (described by the first mechanism with decay rate of $k_1$ is due to triplet ground state oxygen molecules that absorb infrared photons and become singlet oxygen free-radical species that aggressively attack the chromophores. Further, tran-cis isomerization which leads to statistical photo-orientation of the DR1 molecules, is a relatively slow process described by the second mechanism with decay rate of $k_2$.

#### 4.2.3.3 SEO250

SEO250 is a popular EO polymer, which also has a relatively large $\chi^{(3)}$ and negligible fluorescence when it is unpoled (the emission spectrum is shown in Figure 4.10(a) with a strong signal at 517nm and no fluorescence).

A prime application of this polymer is in EO channel waveguide devices. SEO250 is highly photostable with negligible photobleaching in the ultraviolet regime of the spectrum and the ability to transmit on the order of 50mW of CW 1550nm for hundreds of hours well beyond what is needed for most optical communication applications. The sample was fabricated by dissolving SEO250 3% wt. in dibromomethane and leaving it to stir overnight, then a 350 nm thick film was fabricated by spin coating the solution on a fused silica substrate. Figure 4.10(b) shows the normalized photobleached THG signal reflected back from the sample versus exposure time for different excitation powers. The THG profile of the sample is demonstrated in Figure 4.10(c) with 16 squares $(26\mu m \times 26\mu m, 512 \times 512 \text{ pixels}^2)$ each continuously exposed by laser powers ranging from 9-25 mW and 15, 30, 60, and 120 sec exposure times

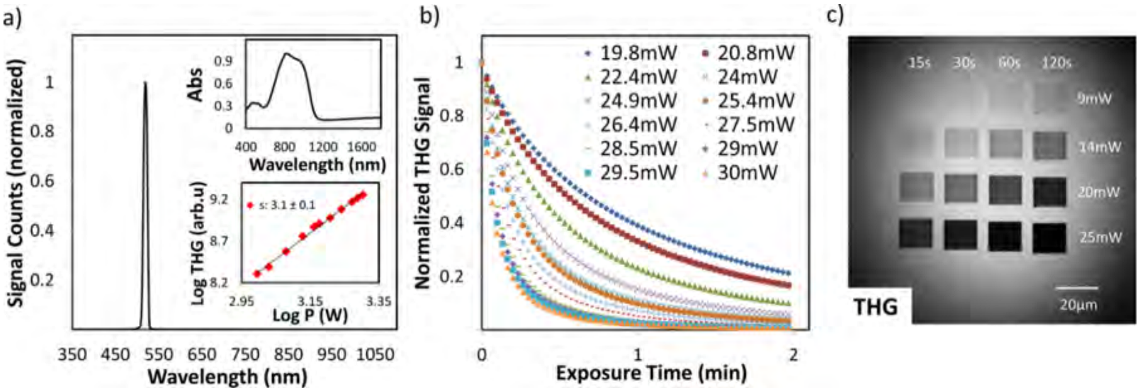

Figure 4.10: Multiphoton spectrum of SEO250 on fused silica, the inset shows a UV/Vis absorption spectrum of SEO250 (top) and the log-log plot of the output THG signal versus input power (bottom), b) normalized THG intensity versus laser exposure timing for various laser powers, and c) THG profile of the sample where each square is continuously exposed by a different laser power and exposure timing

$(\sim 0.5 frame/sec)$. As can be seen in this figure, the observed bleaching has a clear correlation to the amount of laser power as well as to the total duration of the exposure. Figure 4.11(a) demonstrates that the THG decay of SEO250 versus time could be fitted by both a double-exponential and a stretched-exponential. However, consideration of the relative decay rate and amplitude of the two introduced mechanisms when a double-exponential decay law is used, indicates that there is likely a single process for the photobleaching. Figure 4.11(b) demonstrates a log-log plot of the photobleaching rates $(k_1$ and $k_2)$ versus laser power and the ratio of the two mechanisms contribution (shown in the inset) when a double-exponential is used. The slopes of the logarithmic plots (2.27 for $k_1$ and 1.95 for $k_2$) show that bleaching for both mechanisms is due to a two-photon excitation source since both photobleaching rates depend on square of the excitation power. Further, it can be seen that the two mechanisms are comparable in their speed and contribution. Thus, we chose to use a stretched-exponential function to describe the bleaching mechanism of SEO250:

$$T = T_0 e^{-kt^{\beta}} \tag{4.2}$$

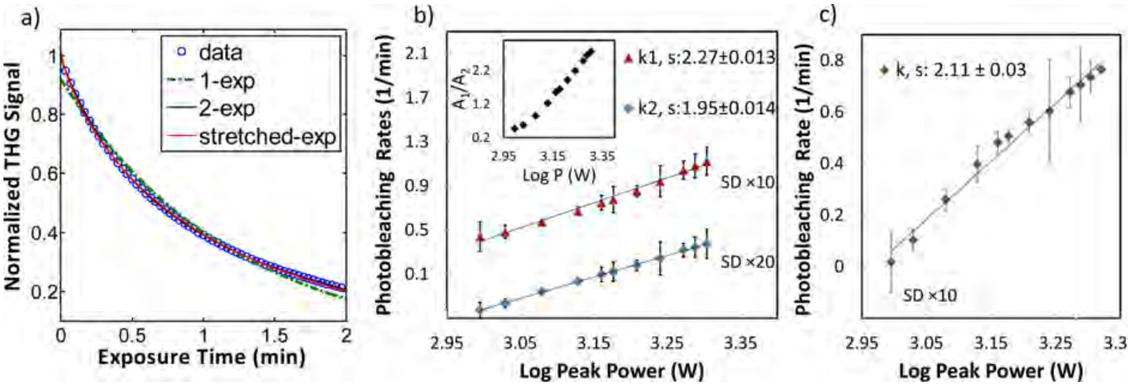

Figure 4.11: a) Fitting SEO250 decay curve with 19.8 mW power (circle-marked line) with 1- (dash-dotted line), 2-(dotted line), and stretched-(solid line) exponential functions. b) log- log plots of the photobleaching rates $k_1$ and $k_2$ for SEO250, inset: the ratio between parameters $A_1$ and $A_2$ vs irradiation power, and c) the photobleaching rate versus irradiation power when the experimental data was fitted with a stretched-exponential function

where $T$ is the THG photon flux, $k$ is the photobleaching rate (1/s), and $0 < \beta < 1$ is a dispersive factor. The slope 2.11 of the plot shown in Figure 4.11(c) demonstrates that as expected from the double-exponential model, only two photons are involved in the bleaching process and that the degradation mechanism is two-photon excitation. This is consistent with the fact that the SEO250 EO chromophore has intense one-photon absorption at 775nm and the non- centrosymmetric nature of the chromophore relaxes the usual parity driven one and two-photon absorption selection rules.

### 4.2.4 Conclusion

In summary, the photobleaching of three electro-optical materials (lithium niobate, Disperse Red 1, and SEO250) was explored under ultrashort pulsed illumination at 1550nm using multi- photon microscopy. One-photon and two-photon excitation have been identified as the main bleaching mechanisms for DR1 and SEO250, respectively. Further, the large chemical stability of $LiNbO_3$ has been confirmed. This method is designed to be a rapid screening test to assist in the development of new materials and to properly target them for applications. Moreover, it can be realized on a broad range of materials using detection probes such as multi-photon excitation FL, SHG, and THG. Furthermore, the involvement of two, three, or even more photons in the bleaching process can be explored. The main application of this work is in the design of various optical devices such as channel waveguides, EO modulators, etc., where by choosing suitable conditions for device performance, such as excitation threshold and the type of material, fabrication with optimum performance and yield is feasible.

## 4.3 Multi-photon microscopy for characterization of 2D materials

Besides biological and photobleaching monitoring applications, we used our MPM to characterize electro-optic (EO) polymers used in Si-photonic devices [176] . In this project, we imaged phase modulators consisting of silicon waveguide devices with EO polymer cladding and measured the SHG intensity using MPM and correlated this intensity with Pockels coefficient ($r_{33}$) measurement. This allowed us to map out $r_{33}$ locally and make quantitative measurements of poled polymer films on non-transparent silicon substrates which is not accessible with conventional Pockels coefficient measurement techniques. Figure 4.12 below shows the MPM images and the quantitative comparison between SHG intensity and $r_{33}$ values.

Using MPM enables rapid characterization and measurement of the Pockels coefficient and may open up a new window to utilize MPM for such application in photonics. Moreover, it can be used for rapid poling optimization by changing laser power, scanning speed and incident light polarization.

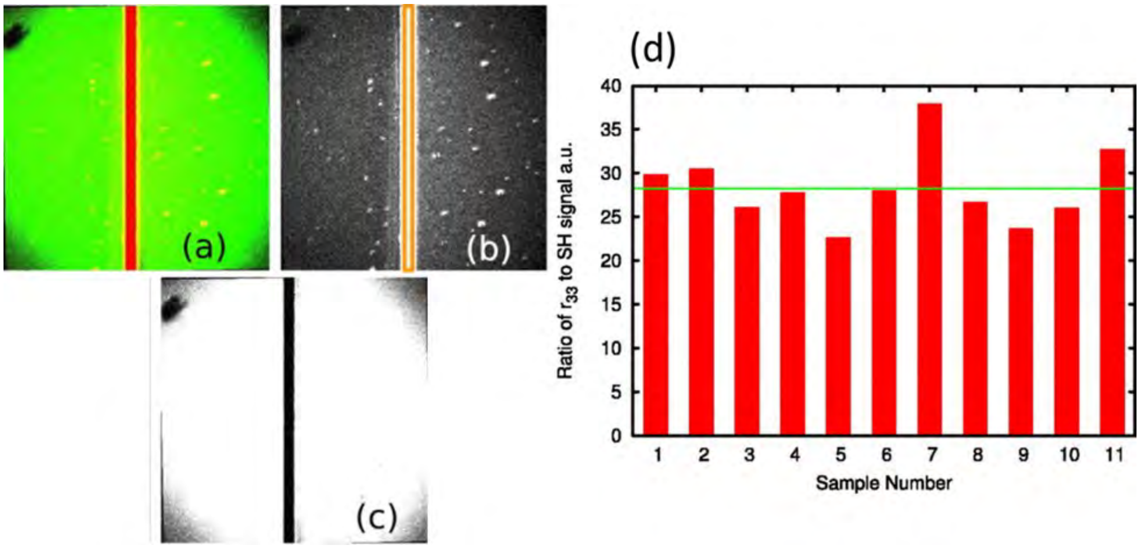

Figure 4.12: (a) Composite of SHG (red) and THG (green), (b) SHG in the poled region, (c) THG from on top of the gold electrodes. The orange box in (b) indicates the region in which the quantitative SHG data was collected. (d) Ratio of the measured $r_{33}$ to the square root

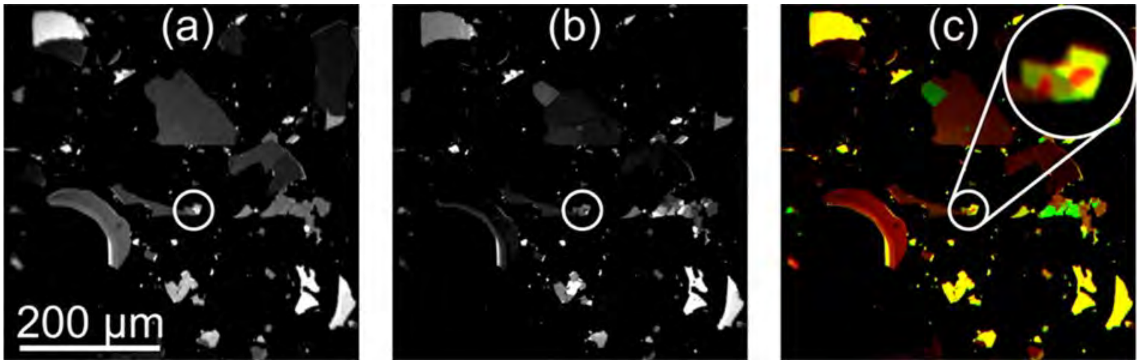

Figure 4.13: Typical multiphoton micrographs of a sample containing exfoliated graphene on $SiO_2/Si$ substrate. (a) Fluorescence, (b) third-harmonic signal, and (c) merged RGB image using fluorescence (red) and THG (green) signals. One particularly interesting few-layer graphene flake considered below is marked with white circles and shown magnified in the merged RGB image

MPM can also be used to characterize 2D materials [100][101][102]. 3PEF and THG signals were used to map out and characterize 2D materials like graphene, GaSe and GaTe. The contrast between the 2D material and substrate appears in THG signal where there is refractive index mismatch or interface between the structures. We showed that MPM can be used as a rapid and noninvasive technique to distinguish between single- and bi-layer graphene in a few seconds compared to the time-consuming and slow conventional technique like Raman microscopy [100]. Besides the speed of scanning, one can map out a larger FOV $(500\mu m \times 500\mu m)$ compared to $50\mu m \times 50\mu m$ one in Raman. Figure 4.13 shows the typical multi-photon images of a sample containing exfoliated graphene on $SiO_2/Si$ substrate. As can be seen, 3PEF and THG signal provide different information about the sample based on the nature of excitation wavelength and emitted signal. In the flakes shown inside the marked circle the contrast between single- and bi-layer areas are readily observable. Figure 4.14 also indicates the power of THG signal on distinguishing different layers of graphene. In this graph the THG intensity was plotted versus the laser power on the sample for different number of layers available on the exfoliated sample. According to the data points and exponential fitted curves, there is almost cubic dependency of the THG signal to the incident power.

We also used SHG and THG signals to investigate the nonlinear optical properties of GaSe which is a 2D layered semiconductor material with a well-known optical crystal [101]. We compared MPM images with standard characterization tools like AFM and Raman measurements to validate our finding. Figure 4.15 presents the SHG and THG signals from a few-layer GaSe flake. The multiphoton emission spectra of different layers were also shown in Figure 4.15(e). Note that SHG and THG provide slightly different information about the layers as can be seen in (c) and quantitative measurement in (d).

Figure 4.16 shows the power dependency curves for SHG and THG signals

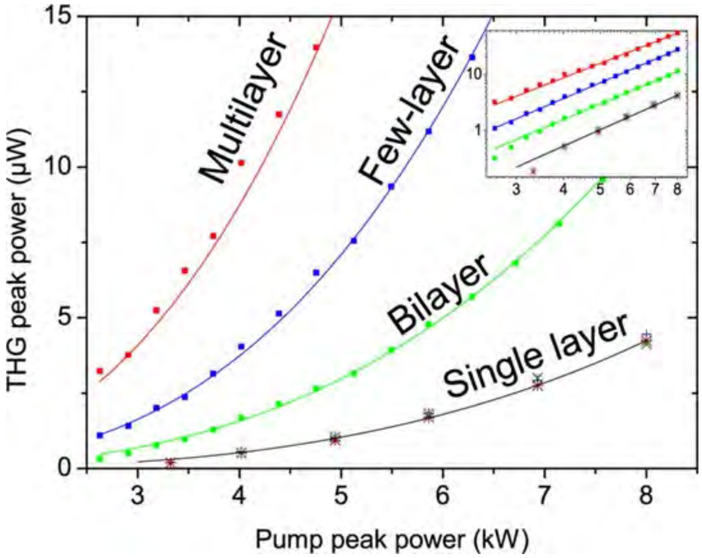

Figure 4.14: Dependence of the THG peak signal on the laser peak power and number of graphene layers. Dots are measurement values; the curves are exponential fits to the power dependence. In the logarithmic plot in the inset, three points corresponding to the lowest THG power deviate from the general trend because the power level is below the linear regime of our detection system

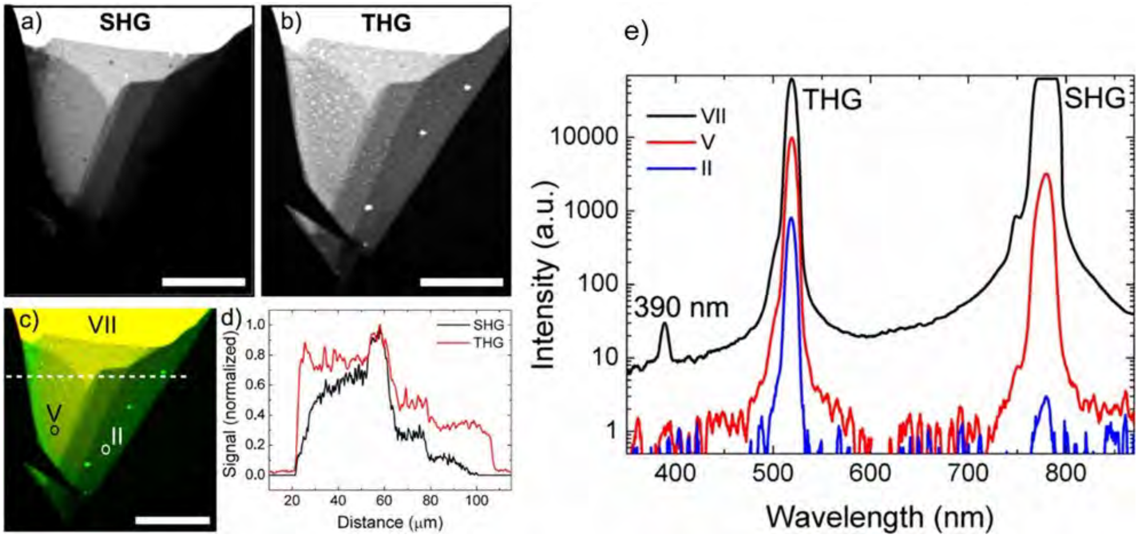

Figure 4.15: (a) SHG and (b) THG images of the few-layer GaSe flake, (c) RGB composite image generated from the SHG and THG images, and (d) cross-sections of the SHG and THG signals taken from the white dashed line in (c). The spectra of the generated light have been measured from the points marked with Roman numbers II, V and VII in (c). (e). Measured spectra of the generated light from three different positions (different thicknesses) on the flake. The positions are marked by Roman numbers II, V and VII

versus the incident power. The slopes of 2 and 3 in the log-log plots ensures the harmonic process. Figure 4.16(c) is the SHG and THG peak powers versus the number of detected layers. According to this graph, the SHG and THG intensity increase with the number of layers. However, it should be noted that based on theory the reflected SHG and THG signals have sinc-like behavior for reflection mode. Through the reflected SHG and THG coherence length, the maximum SHG and THG signal can be calculated and the corresponding number of layers can be extracted. The reflected SHG and THG coherence length can be calculated as:

$$l_c^{BSHG} = \frac{\lambda}{4(n(2\omega)+n(\omega))} = \frac{1560nm}{4(2.75+2.85)} = 70nm \tag{4.3}$$

$$l_c^{BTHG} = \frac{\lambda}{6(n(3\omega)+n(\omega))} = \frac{1560nm}{6(2.75+3.19)} = 45nm \tag{4.4}$$

In which $n$ is the refractive index at the subscript frequency. Therefore, for layers with thicknesses of below the coherence length the SHG and THG signals increase monotonically. For layers larger than these values the intensities decrease. Note that this sinc-like behavior is periodic and for larger thicknesses, the SHG and THG intensities increase and then decrease.

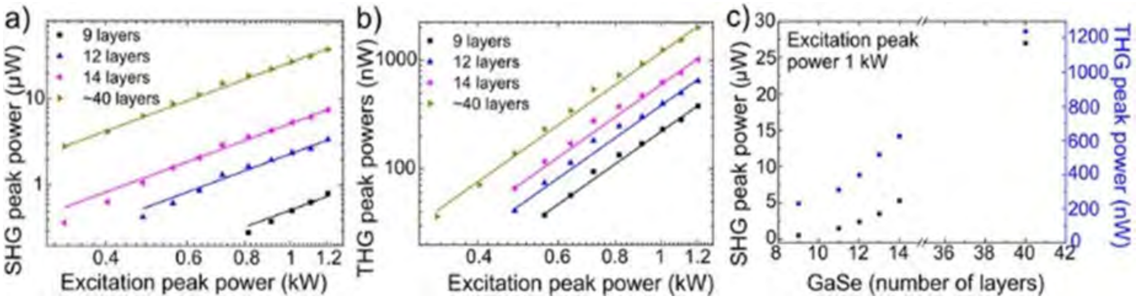

Figure 4.16: Power dependence of the (a) SHG and (b) THG signals. (c) SHG and THG signals as a function of the number of the GaSe layers measured with $1kW$ excitation peak power

Similarly, we performed the same study for another 2D semiconductor material, GaTe [103]. SHG and THG images as well as AFM micrograph are shown in Figure 4.17. The calculated coherence lengths for SHG and THG signals are 34nm and 46nm, respectively. According to SHG and THG intensities versus the excitation peak power show that for the layer thicknesses below the coherence lengths, the peak powers increase monotonically, while for layers thicker than the coherence lenght there is a decreasing trend. The nonlinear susceptibilities of 2D materials can be calculated using SHG and THG signals showing the powerful capability of MPM for rapid and accurate material characterization.

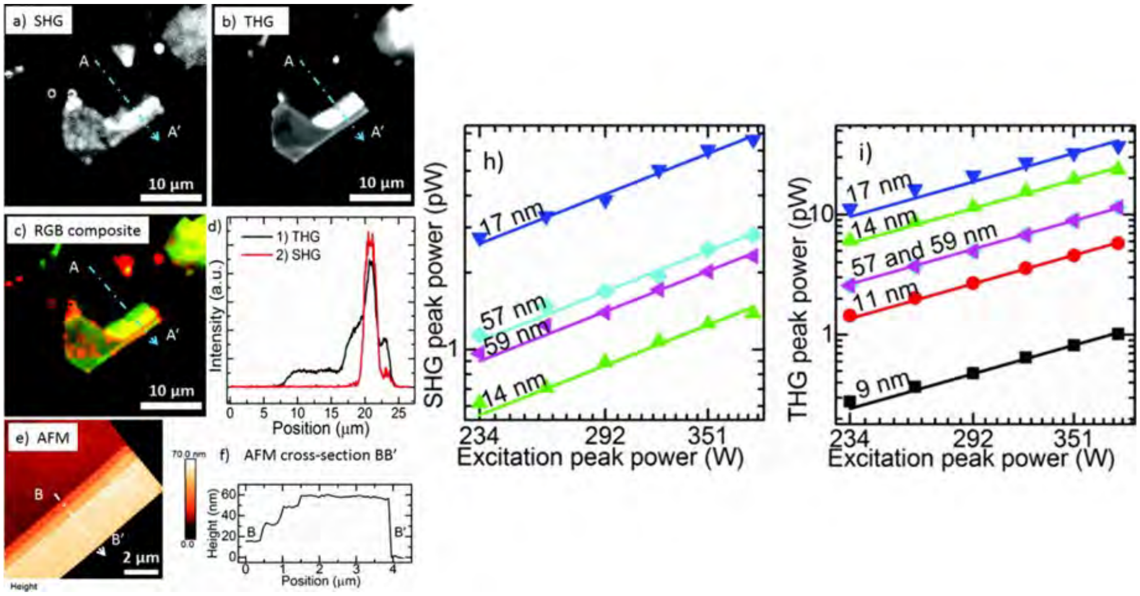

Figure 4.17: (a) SHG and (b) THG images of the few-layer GaTe flake. (c) RGB composite image generated from the SHG and THG images. (d) Cross-sectional SHG and THG signals taken from the blue dashed line in (c); scale bars in the SHG and THG images are $10\mu m$. (e) AFM image of the staircase area where the intensity is at maximum for both SHG and THG. (f) AFM cross-section of the staircase area taken from the white dashed line B-B′ in (e) showing the steps from 17 to 57nm. Excitation peak power dependence of the (h) SHG and (i) THG signals. The lines are fits to square (h) and cubic (i) power dependences

In another experiment, THG signal was used to characterize the third-order nonlinearity of high-quality nanocrystalline titanium dioxide ($TiO_2$) made with a novel Atomic Layered Deposition (ALD) technique [177]. The measurements show that the third-order nonlinearity decreases with the smaller crystal size. Real-time monitoring of chromophore alignment in photorefractive polymer devices through imaging SHG distribution was performed by applying electric field across the electrodes [104]. Figure 4.18 below shows the SHG intensity versus the induced electric field. As can be seen, the SHG signal increases with applied electric field until the breakdown occurs in which SHG signal vanishes.

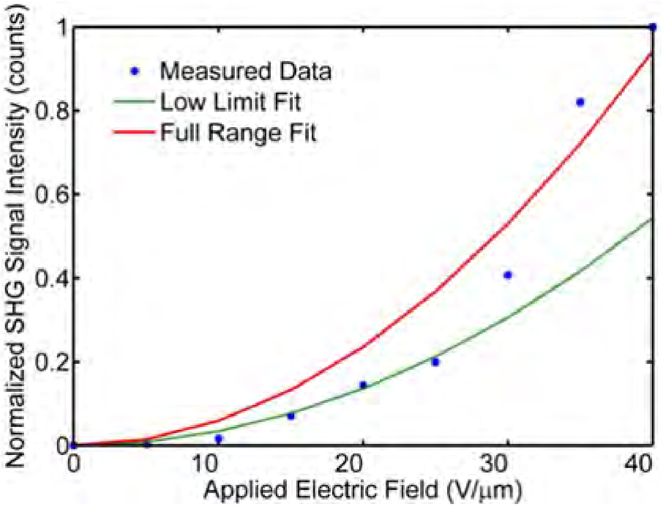

Figure 4.18: SHG intensity versus the induce voltage across the electrodes

Additionally, we used our MPM to image well-ordered quantum dots (QD) directly assembled within photonic nanocomposites. Figure 4.19 shows the multi-photon emission of QD and the polymer substrate. As can be observed the polymer exhibits strong THG while QD has stronger 3PEF signal.

The nonlinear properties of directly deposited and transferred to the dielectric substrate graphene were measured and compared [178]. It was also demonstrated that bi-layer transferred graphene and directly deposited one have comparable THG intensities and damage thresholds. Figure 4.20(a) above shows the damage threshold for mono- and-bi-layer transferred graphene as well as directly

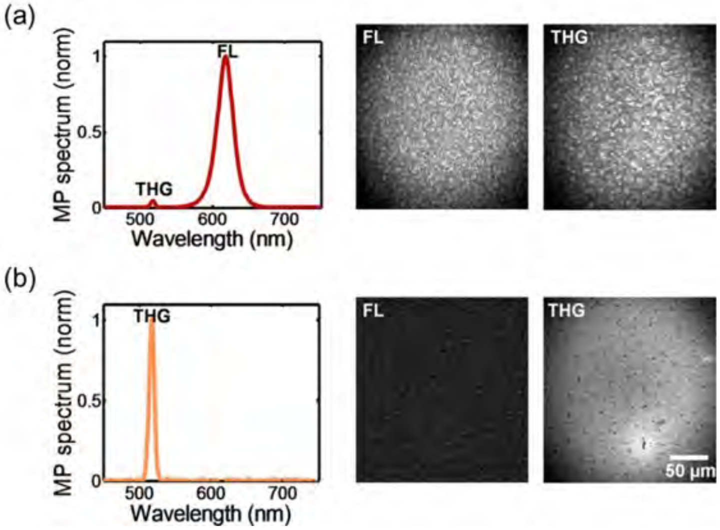

Figure 4.19: Normalized multiphoton excitation spectra and micrographs of (a) the blend of BBCP D with 30 wt % QDs and (b) neat polymer sample. The wavelength of light for excitation was 1550nm

deposited graphene. Figure 4.20(b, c) also depicts THG images of these two samples.

In an experiment, silicon surface was patterned on nanoridge array waveguides and the sample was illuminated by 1550nm excitation wavelength [179]. The THG signal for different trench and ridge geometries were measured and plotted in Figure 4.21(b). It was shown that for larger ridge sizes the THG increases. Moreover, the effect of incident light polarization on the THG signal was investigated. Figure 4.21(c) shows the THG signal for TE and TM polarizations. As expected for TE polarization THG is maximum while for TM polarization it reaches its minimum.

Finally, two-photon microscopy was used to compare the enhancement of 2PEF from three chromophores by fabricating grating substrate having the resonance frequency tuned to the 1040nm excitation wavelength [180]. Figure 4.22 below shows the 2PEF images of rhodamine 6G, GFP and chlorophyll across the

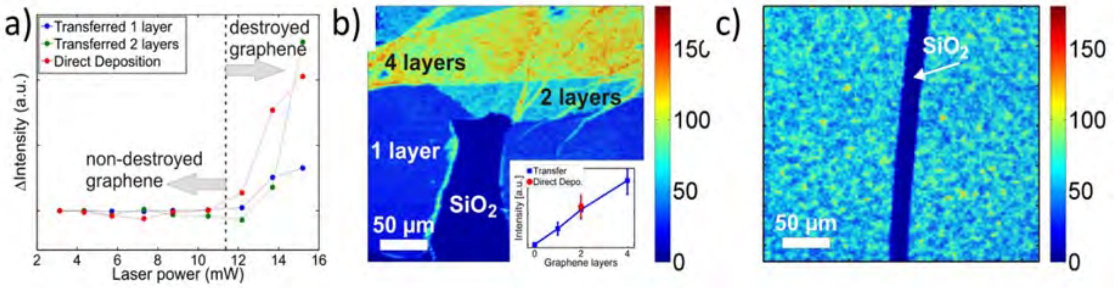

Figure 4.20: Damage threshold of directly deposited graphene is comparable to mono- and bi-layered graphene prepared by the transfer technique. ÎŤIntensity is the intensity difference of THG signal between the studied area and the reference area. The damage area has less THG than the pristine area. Multiphoton microscopic images of (a) transferred graphene film with a tear and folded areas and (b) directly deposited graphene with a scratch made by a scalpel. (a-inset) average graphene film thickness is comparable to folded bi-layered graphene prepared by transfer technique. (Both image size is about 300 × 300$\mu m^2$. Color bar indicates the intensity of THG signal.)

boundaries between the textured and planar substrates.

The comparison between 2PEF from planar and textured areas are also shown in Figure 4.23.

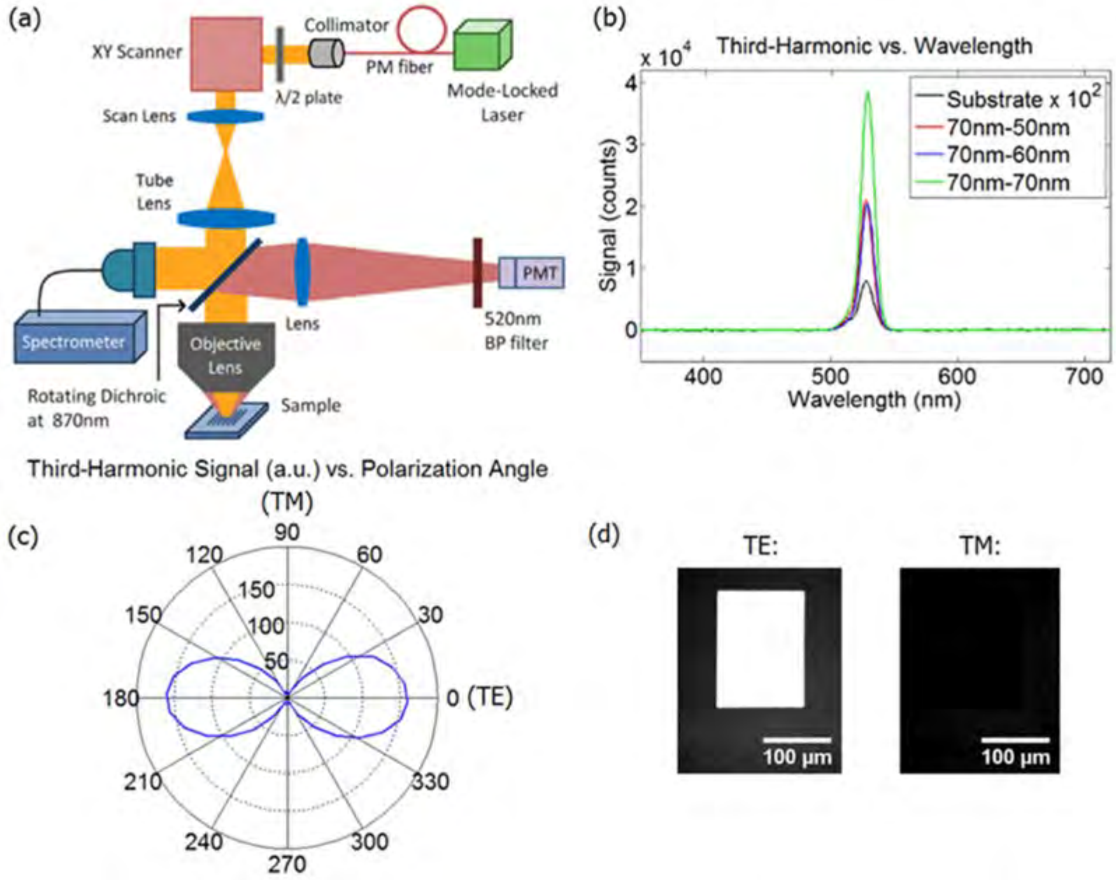

Figure 4.21: (a) Optical setup used to measure the third-harmonic signal of the silicon samples. (b) Measured third-harmonic spectra for the samples with different trench and ridge geometries. (c) THG signal as a function of the angle of polarization of the input be beam. (d) Spatially resolved optical images of the third-harmonic signal for two orthogonal polarizations of the input beam

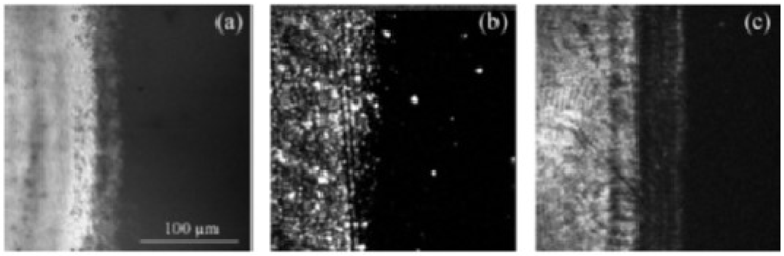

Figure 4.22: Multiphoton microscope images of the boundaries between textured (left) and planar (right) substrates coated with rhodamine 6G (a), green fluorescent protein (b), and chlorophyll (c)

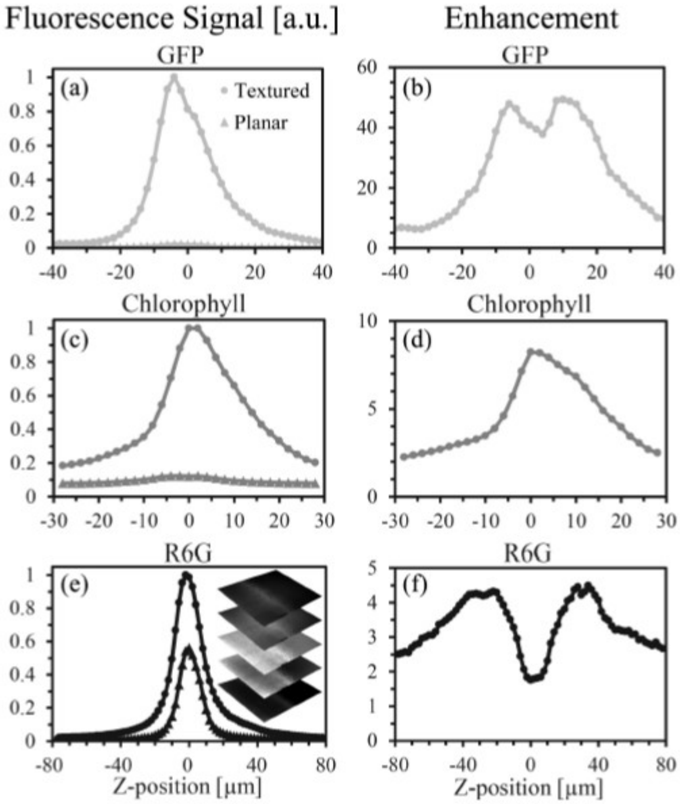

Figure 4.23: Fluorescence signals (left column) and enhancements (right column) calculated from the MPM measurements. The inset shows five images of the R6G sample at different focus positions

# CHAPTER 5

## Summary

In this dissertation I described the theory of multiphoton microscopy and multiphoton imaging modalities including SHG, THG, 2PEF and 3PEF. The full design and assembly of a compact MPM was explained in details starting from the optical design of a relay lens system, compound scan tube lenses. A laser scanning LabVIEW-based software was also developed to acquire, save and manipulate the images. Throughout the application section, a novel methodology based on nonlinear response of a sharp edge of GaAs wafer was introduced to characterize the objective lenses used in MPM. This method is originated from a known technique called "knife edge"; however, here we expanded this technique to the nonlinear regime. Different imaging modalities were utilized to investigate the biological samples in response to femtosecond illumination. A clear correlation between label-free THG images and conventional H&E light microscopy images were found in [99]. Moreover, it was shown that SHG is an alternative modality that can be used to help pathologists distinguish between different stages of cancer progress. THG signal was also used to monitor the photobleaching of EO polymers under femntosecond illumination at certain powers and pulse durations [4]. The decay in THG signal can indicate the life-time of EO polymer which can be used for manufacturing of the modulators used in telecommunication systems. MPM can also be used to characterize the optical properties of 2D materials such as Graphene [100], GaSe [101] and GaTe [102]. This brought a rapid and accurate methodology for 2D materials characterization in the field which can be replaced for slow characterization techniques such as Raman, SEM or AFM. The wide range of MPM applications make MPM a promising tool for studies of not only biological samples but also optical characterization of 2D materials. Currently, new applications of MPM are discovered every day showing that MPM is on its path to be used widespread; however, a few limitations in laser source size and cost, optimum optical design and detection have to be addressed before it becomes widely used in special applications such as clinical diagnosis.

# REFERENCES

[1] Warren R Zipfel, Rebecca M Williams, and Watt W Webb. Nonlinear magic: multiphoton microscopy in the biosciences. *Nature biotechnology*, 21(11):1369–1377, 2003.

[2] Soroush Mehravar, Bhaskar Banerjee, Hemant Chatrath, Babak Amirsolaimani, Krunal Patel, Charmi Patel, Robert a Norwood, Nasser Peyghambarian, and Khanh Kieu. Label-free multi-photon imaging of dysplasia in Barrett's esophagus. *Biomedical Optics Express*, 7(1):148, 2016.

[3] Kaitlin Harpel, Robert Dawson Baker, Babak Amirsolaimani, Soroush Mehravar, Josef Vagner, Terry O. Matsunaga, Bhaskar Banerjee, and Khanh Kieu. Imaging of targeted lipid microbubbles to detect cancer cells using third harmonic generation microscopy. *Biomedical Optics Express*, 7(7):2849, 2016.

[4] Shiva Shahin, Soroush Mehravar, Palash Gangopadhyay, Nasser Peyghambarian, Robert. a. Norwood, and Khanh Kieu. Multiphoton microscopy as a detection tool for photobleaching of EO materials. *Optics Express*, 22(25):30955–30962, 2014.

[5] M. J. Levene. In Vivo Multiphoton Microscopy of Deep Brain Tissue. *Journal of Neurophysiology*, 91(4):1908–1912, 2004.

[6] Fritjof Helmchen, Karel Svoboda, Wilfred Denk, and David W. Tank. In vivo dendritic calcium dynamics in deep-layer neocortical pyramidal neurons. *Nature*, 2:989–996, 1999.

[7] Nicholas G. Horton, Ke Wang, Chun Chin Wang, and Chris Xu. In vivo three-photon imaging of subcortical structures of an intact mouse brain using quantum dots. *2013 Conference on Lasers and Electro-Optics Europe and International Quantum Electronics Conference, CLEO/Europe-IQEC 2013*, 7(March):205–209, 2013.

[8] Matthew J. Farrar, Frank W. Wise, Joseph R. Fetcho, and Chris B. Schaffer. In vivo imaging of myelin in the vertebrate central nervous system using third harmonic generation microscopy. *Biophysical Journal*, 100(5):1362–1371, 2011.

[9] Evan P. Perillo, Justin E. McCracken, Daniel C. Fernée, John R. Goldak, Flor a. Medina, David R. Miller, Hsin-Chih Yeh, and Andrew K. Dunn. Deep in vivo two-photon microscopy with a low cost custom built mode-locked 1060 nm fiber laser. *Biomedical Optics Express*, 7(2):324, 2016.

[10] Ryosuke Kawakami, Kazuaki Sawada, Aya Sato, Terumasa Hibi, Yuichi Kozawa, Shunichi Sato, Hiroyuki Yokoyama, and Tomomi Nemoto. Visualizing hippocampal neurons with in vivo two-photon microscopy using a 1030 nm picosecond pulse laser. *Scientific reports*, 3:1014, 2013.

[11] Timothy Ragan, Lolahon R Kadiri, Kannan Umadevi Venkataraju, Karsten Bahlmann, Jason Sutin, Julian Taranda, Ignacio Arganda-Carreras, Yongsoo Kim, H Sebastian Seung, and Pavel Osten. Serial two-photon tomography for automated ex vivo mouse brain imaging. *Nature Methods*, 9(3):255–258, 2012.

[12] Pierre Mahou, Maxwell Zimmerley, Karine Loulier, Katherine S Matho, Guillaume Labroille, Xavier Morin, Willy Supatto, Jean Livet, Delphine Débarre, and Emmanuel Beaurepaire. Multicolor two-photon tissue imaging by wavelength mixing. *Nature Methods*, 9(8):815–818, 2012.

[13] Adrian Negrean and Huibert D Mansvelder. Optimal lens design and use in laser-scanning microscopy. *Biomedical optics express*, 5(5):1588–609, 2014.

[14] P S Tsai, C Mateo, J J Field, C B Schaffer, M E Anderson, and D Kleinfeld. Ultra-large field-of-view two-photon microscopy. *Opt.Express*, 23(1094-4087 (Electronic)):13833–13847, 2015.

[15] Spencer L. Smith Jeffrey N. Stirman, Ikuko T. Smith, Michael W. Kudenov. Wide field-of-view, multi-region two-photon imaging of neuronal activity. pages 1–16, 2014.

[16] Galiya Sharafutdinova, John Holdsworth, and Dirk Van Helden. Improved field scanner incorporating parabolic optics . Part 1 : Simulation. 48(22):4389–4396, 2009.

[17] Galiya Sharafutdinova, John Holdsworth, and Dirk van Helden. Improved field scanner incorporating parabolic optics. Part 2: Experimental verification and potential for volume scanning. *Applied optics*, 49(29):5517–5527, 2010.

[18] David G. Rosenegger, Cam Ha T Tran, Jeffery LeDue, Ning Zhou, and Grant R. Gordon. A high performance, cost-effective, open-source microscope for scanning two-photon microscopy that is modular and readily adaptable. *PLoS ONE*, 9(10), 2014.

[19] Q T Nguyen, N Callamaras, C Hsieh, and I Parker. Construction of a two-photon microscope for video-rate Ca(2+) imaging. *Cell calcium*, 30(6):383–93, 2001.

[20] Volodymyr Nikolenko and Rafael Yuste. How to build a two-photon microscope with a confocal scan head. *Cold Spring Harbor Protocols*, 8(6):588–592, 2013.

[21] Edward Botcherby, Christopher Smith, Martin Booth, Rimas Juskaitis, and Tony Wilson. Arbitrary-scan imaging for two-photon microscopy. 7569:756917, 2010.

[22] Gergely Katona, Gergely Szalay, Pál Maák, Attila Kaszás, Máté Veress, Dániel Hillier, Balázs Chiovini, E Sylvester Vizi, Botond Roska, and Balázs Rózsa. Fast two-photon in vivo imaging with three-dimensional random-access scanning in large tissue volumes. *Nature Methods*, 9(2):201–208, 2012.

[23] Fritjof Helmchen, Werner Go, Werner Göbel, and Björn M Kampa. Imaging cellular network dynamics in three dimensions using fast 3D laser scanning. *Nat Methods*, 4(1):73–79, 2007.

[24] Benjamin A. Flusberg, Juergen C. Jung, Eric D. Cocker, Erik P. Anderson, and Mark J. Schnitzer. In vivo brain imaging using a portable 39?gram two-photon fluorescence microendoscope. *Optics Letters*, 30(17):2272, 2005.

[25] D E Spence, P N Kean, and W Sibbett. 60-fsec pulse generation from a self-mode-locked Ti:sapphire laser. *Optics letters*, 16(1):42–44, 1991.

[26] C. T A Brown, M. A. Cataluna, A. A. Lagatsky, E. U. Rafailov, M. B. Agate, C. G. Leburn, and W. Sibbett. Compact laser-diode-based femtosecond sources. *New Journal of Physics*, 6:1–21, 2004.

[27] Charles G Durfee, Tristan Storz, Jonathan Garlick, Steven Hill, Jeff a Squier, Matthew Kirchner, Greg Taft, Kevin Shea, Henry Kapteyn, Margaret Murnane, and Sterling Backus. Direct diode-pumped Kerr-lens mode-locked Ti:sapphire laser. *Optics Express*, 20(13):13677–13683, 2012.

[28] Michael D. Young, Sterling Backus, Charles Durfee, and Jeff Squier. Multiphoton imaging with a direct-diode pumped femtosecond Ti: Sapphire laser. *Journal of Microscopy*, 249(2):83–86, 2013.

[29] Herman A. Haus. Mode-locking of lasers. *IEEE Journal on Selected Topics in Quantum Electronics*, 6(6):1173–1185, 2000.

[30] K.F. Wall and A. Sanchez. Titanium Sapphire lasers. *The Lincoln laboratory journal*, 3(3):447–462, 1990.

[31] Claude Rullière, editor. *Femtosecond Laser Pulses*. Advanced Texts in Physics. Springer New York, New York, NY, 2005.

[32] *Solid-State Laser Engineering*, volume 1 of *Springer Series in Optical Sciences*. Springer New York, New York, NY, 2006.

[33] M. Guina, N. Xiang, and O. G. Okhotnikov. Stretched-pulse fiber lasers based on semiconductor saturable absorbers. *Applied Physics B: Lasers and Optics*, 74(SUPPL.):193–200, 2002.

[34] Jeff Squier and Michiel Müller. High resolution nonlinear microscopy: A review of sources and methods for achieving optimal imaging. *Review of Scientific Instruments*, 72(7):2855–2867, 2001.

[35] P F Curley, A I Ferguson, J G White, and W B Amos. Application of a femtosecond self-sustaining mode-locked Ti:sapphire laser to the field of laser scanning confocal microscopy. *Optical and Quantum Electronics*, 24:851–859, 1992.

[36] Ke Wang, Tzu-Ming Liu, Juwell Wu, Nicholas G. Horton, Charles P. Lin, and Chris Xu. Three-color femtosecond source for simultaneous excitation of three fluorescent proteins in two-photon fluorescence microscopy. *Biomedical Optics Express*, 3(9):1972, 2012.

[37] Andrew C. Millard, Paul W. Wiseman, David N. Fittinghoff, Kent R. Wilson, Jeffrey A. Squier, and Michiel Müller. Third-harmonic generation mi-

croscopy by use of a compact, femtosecond fiber laser source. *Applied optics*, 38(36):7393–7397, 1999.

[38] C Xu and F W Wise. Recent Advances in Fiber Lasers for Nonlinear Microscopy. *Nature photonics*, 7(11):875–882, 2013.

[39] a Brenier. A new evaluation of Yb3+-doped crystals for laser applications. *Journal of Luminescence*, 92(v):199–204, 2001.

[40] F Brunner, G J Spühler, J. Aus der Au, L Krainer, F Morier-Genoud, R Paschotta, N Lichtenstein, S Weiss, C Harder, A A Lagatsky, A Abdolvand, N V Kuleshov, and U Keller. Diode-pumped femtosecond Yb:KGd(WO4)2 laser with 1.1-W average power. *Optics Letters*, 25(15):1119, 2000.

[41] Hung-Wen Chen, Guoqing Chang, Shanhui Xu, Zhongmin Yang, and Franz X. Kärtner. 3 GHz, fundamentally mode-locked, femtosecond Yb-fiber laser. *Optics Letters*, 37(17):3522, 2012.

[42] K. Tamura, E. P. Ippen, and H. A. Haus. Pulse dynamics in stretched-pulse fiber lasers. *Applied Physics Letters*, 67(1995):158, 1995.

[43] M E Fermann. Passive mode locking by using nonlinear polarization evolution in a polarization-maintaining erbium-doped fiber. *Optics letters*, 18(11):894, 1993.

[44] S Yamashita. A Tutorial on Nonlinear Photonic Applications of Carbon Nanotube and Graphene. *Lightwave Technology, Journal of*, 30(4):427–447, 2012.

[45] Tawfique Hasan, Zhipei Sun, Fengqiu Wang, Francesco Bonaccorso, Ping Heng Tan, Aleksey G. Rozhin, and Andrea C. Ferrari. Nanotube

- Polymer composites for ultrafast photonics. *Advanced Materials*, 21(38-39):3874–3899, 2009.

[46] Khanh Kieu and Masud Mansuripur. Femtosecond laser pulse generation with a fiber taper embedded in carbon nanotube/polymer composite. *Optics Letters*, 32(15):2242, 2007.

[47] John M. Girkin, Simon Poland, and Amanda J. Wright. Adaptive optics for deeper imaging of biological samples. *Current Opinion in Biotechnology*, 20(1):106–110, 2009.

[48] O Albert, L Sherman, G Mourou, T B Norris, and G Vdovin. Smart microscope: an adaptive optics learning system for aberration correction in multiphoton confocal microscopy. *Optics letters*, 25(1):52–54, 2000.

[49] Martin J Booth, Mark a a Neil, Rimas Juskaitis, and Tony Wilson. Adaptive aberration correction in a confocal microscope. *Proceedings of the National Academy of Sciences of the United States of America*, 99(9):5788–5792, 2002.

[50] Aurélie Facomprez, Emmanuel Beaurepaire, and Delphine Débarre. Accuracy of correction in modal sensorless adaptive optics. *Optics Express*, 20(3):2598, 2012.

[51] Zhibin Wang, Dan Wei, Ling Wei, Yi He, Guohua Shi, Xunbin Wei, and Yudong Zhang. Aberration correction during real time in vivo imaging of bone marrow with sensorless adaptive optics confocal microscope. *Journal of biomedical optics*, 19(8):086009, 2014.

[52] Lingjie Kong and Meng Cui. In vivo deep tissue imaging via iterative multiphoton adaptive compensation technique. *IEEE Journal on Selected Topics in Quantum Electronics*, 22(4), 2016.

[53] P. T. Galwaduge, S. H. Kim, L. E. Grosberg, and E. M. C. Hillman. Simple wavefront correction framework for two-photon microscopy of in-vivo brain. *Biomedical Optics Express*, 6(8):2997, 2015.

[54] L. Sherman, J. Y. Ye, O. Albert, and T. B. Norris. Adaptive correction of depth-induced aberrations in multiphoton scanning microscopy using a deformable mirror. *Journal of Microscopy*, 206(1):65–71, 2002.

[55] Nicolas Olivier, Delphine Débarre, and Emmanuel Beaurepaire. Dynamic aberration correction for multiharmonic microscopy. *Optics letters*, 34(20):3145–3147, 2009.

[56] Delphine Débarre, Edward J Botcherby, Tomoko Watanabe, Shankar Srinivas, Martin J Booth, and Tony Wilson. Image-based adaptive optics for two-photon microscopy. *Optics Letters*, 34(16):2495, 2009.

[57] P Marsh, D Burns, and J Girkin. Practical implementation of adaptive optics in multiphoton microscopy. *Opt Express*, 11(10):1123–1130, 2003.

[58] Na Ji, DE Milkie, and Eric Betzig. Adaptive optics via pupil segmentation for high-resolution imaging in biological tissues. *nAture methods*, 7(2):141–147, 2009.

[59] Martin Skorsetz, Pablo Artal, and Juan M. Bueno. Performance evaluation of a sensorless adaptive optics multiphoton microscope. *Journal of Microscopy*, 261(3):249–258, 2016.

[60] David Sinefeld, Hari P Paudel, Dimitre G Ouzounov, Thomas G Bifano, Chris Xu, D Kobat, M E Durst, N Nishimura, A W Wong, C B Schaffer, C Xu, J C Jung, A D Mehta, E Aksay, R Stepnoski, and M J Schnitzer. Adaptive optics in multiphoton microscopy: comparison of two, three and four photon fluorescence. *Neurosci*, 13(11):1433–1440, 2010.

[61] Karsten Bahlmann, Peter T So, Michael Kirber, Robert Reich, Bernard Kosicki, William McGonagle, and Karl Bellve. Multifocal multiphoton microscopy (MMM) at a frame rate beyond 600 Hz. *Optics express*, 15(17):10991, 2007.

[62] T. Nielsen, M. Fricke, D. Hellweg, and P. Andresen. High efficiency beam splitter for multifocal multiphoton microscopy. *Journal of Microscopy*, 201(3):368–376, 2001.

[63] Martin Straub and Stefan W Hell. Multifocal multiphoton microscopy: a fast and efficient tool for 3-D fluorescence imaging. *Bioimaging*, 6(1998):177–185, 1998.

[64] Rainer Pick and Stefan W Hell. Multifocal multiphoton microscopy J org. 23(9):655–657, 1998.

[65] Alexander Egner and Stefan W. Hell. Time multiplexing and parallelization in multifocal multiphoton microscopy. *Journal of the Optical Society of America A*, 17(7):1192, 2000.

[66] A. H. Buist, M. Müller, J. Squier, and G. J. Brakenhoff. Real time two-photon absorption microscopy using multi point excitation. *Journal of Microscopy*, 192(2):217–226, 1998.

[67] Raluca Niesner, Volker Andresen, Jens Neumann, Heinrich Spiecker, and Matthias Gunzer. The power of single and multibeam two-photon microscopy for high-resolution and high-speed deep tissue and intravital imaging. *Biophysical journal*, 93(7):2519–29, 2007.

[68] Ki Hean Kim, Christof Buehler, Karsten Bahlmann, Timothy Ragan, Wei-Chung a Lee, Elly Nedivi, Erica L Heffer, Sergio Fantini, and Peter T C So.

Multifocal multiphoton microscopy based on multianode photomultiplier tubes. *Optics express*, 15(18):11658–11678, 2007.

[69] Israel Veilleux, J.A. Spencer, D.P. Biss, D. Cote, and C.P. Lin. In Vivo Cell Tracking With Video Rate Multimodality Laser Scanning Microscopy. *IEEE Journal of Selected Topics in Quantum Electronics*, 14(1):10–18, 2008.

[70] Anthony M D Lee, Hequn Wang, Yingqiu Yu, Shuo Tang, Jianhua Zhao, Harvey Lui, David I McLean, and Haishan Zeng. In vivo video rate multiphoton microscopy imaging of human skin. *Optics letters*, 36(15):2865–2867, 2011.

[71] G.Y. Fan, H. Fujisaki, A. Miyawaki, R.-K. Tsay, Roger Y. Tsien, and Mark H. Ellisman. Video-Rate Scanning Two-Photon Excitation Fluorescence Microscopy and Ratio Imaging with Cameleons. *Biophysical Journal*, 76(5):2412–2420, 1999.

[72] Edward J Botcherby, Christopher W Smith, Michael M Kohl, Delphine Débarre, Martin J Booth, Rimas Juškaitis, Ole Paulsen, and Tony Wilson. Aberration-free three-dimensional multiphoton imaging of neuronal activity at kHz rates. *Proceedings of the National Academy of Sciences of the United States of America*, 109(8):2919–24, 2012.

[73] Y Kremer, J-F Léger, R Lapole, N Honnorat, Y Candela, S Dieudonné, and L Bourdieu. A spatio-temporally compensated acousto-optic scanner for two-photon microscopy providing large field of view. *Optics express*, 16(14):10066–10076, 2008.

[74] Paul a Kirkby, K M Naga Srinivas Nadella, and R Angus Silver. A compact Acousto-Optic Lens for 2D and 3D femtosecond based 2-photon microscopy. *Optics express*, 18(13):13721–45, 2010.

[75] K Konig, H Liang, M W Berns, and B J Tromberg. Cell damage in near-infrared multimode optical traps as a result of multiphoton absorption. *Optics Letters*, 21(14):1090–1092, 1996.

[76] G D Reddy, K Kelleher, R Fink, and P Saggau. Three-dimensional random access multiphoton microscopy for functional imaging of neuronal activity. *Nat Neurosci*, 11(6):713–720, 2008.

[77] R. Salom??, Y. Kremer, S. Dieudonn??, J. F. L??ger, O. Krichevsky, C. Wyart, D. Chatenay, and L. Bourdieu. Ultrafast random-access scanning in two-photon microscopy using acousto-optic deflectors. *Journal of Neuroscience Methods*, 154(1-2):161–174, 2006.

[78] Yonghong Shao, Wan Qin, Honghai Liu, Junle Qu, Xiang Peng, Hanben Niu, and Bruce Z. Gao. Addressable multiregional and multifocal multiphoton microscopy based on a spatial light modulator. *Journal of Biomedical Optics*, 17(3):030505, 2012.

[79] A Bullen, S S Patel, and P Saggau. High-Speed , Random-Access Fluorescence Microscopy : 1 . High-Resolution Optical Recording with Voltage-Sensitive Dyes and Ion Indicators ryz :. *Biophysical Journal*, 73(1):477–491, 1997.

[80] Benjamin F Grewe, Fabian F Voigt, Marcel van 't Hoff, and Fritjof Helmchen. Fast two-layer two-photon imaging of neuronal cell populations using an electrically tunable lens. *Biomedical optics express*, 2(7):2035–2046, 2011.

[81] G J Brakenhoff, J Squier, T Norris, A C Bliton, M H Wade, and B Athey. Real-time two-photon confocal microscopy using a femtosecond, amplified Ti:sapphire system. *Journal of Microscopy*, 181(3):253–259, 1996.

[82] Dan Oron, Eran Tal, and Yaron Silberberg. Scanningless depth-resolved microscopy. *Optics express*, 13(5):1468–1476, 2005.

[83] Guanghao Zhu, James van Howe, Michael Durst, Warren Zipfel, and Chris Xu. Simultaneous spatial and temporal focusing of femtosecond pulses. *Optics express*, 13(6):2153–2159, 2005.

[84] O D Therrien, B Aubé, S Pagès, P De Koninck, and D Côté. Wide-field multiphoton imaging of cellular dynamics in thick tissue by temporal focusing and patterned illumination. *Biomedical optics express*, 2(3):696–704, 2011.

[85] Li-Chung Cheng, Chia-Yuan Chang, Chun-Yu Lin, Keng-Chi Cho, Wei-Chung Yen, Nan-Shan Chang, Chris Xu, Chen Yuan Dong, and Shean-Jen Chen. Spatiotemporal focusing-based widefield multiphoton microscopy for fast optical sectioning. *Optics Express*, 20(8):8939, 2012.

[86] M. E. Durst, G. Zhu, and C. Xu. Simultaneous spatial and temporal focusing in nonlinear microscopy. *Optics Communications*, 281(7):1796–1805, 2008.

[87] Samarendra K Mohanty, Rainer K Reinscheid, Xiaobin Liu, Naoe Okamura, Tatiana B Krasieva, and Michael W Berns. In-depth activation of channelrhodopsin 2-sensitized excitable cells with high spatial resolution using two-photon excitation with a near-infrared laser microbeam. *Biophysical journal*, 95(8):3916–26, 2008.

[88] Michael E Durst, Adam A Straub, and Chris Xu. Enhanced axial confinement of sum-frequency generation in a temporal focusing setup. *Optics letters*, 34(12):1786, 2009.

[89] Bertalan K Andrasfalvy, Boris V Zemelman, Jianyong Tang, and Alipasha Vaziri. Two-photon single-cell optogenetic control of neuronal activity by

sculpted light. *Proceedings of the National Academy of Sciences of the United States of America*, 107(26):11981–6, 2010.

[90] Edward J Botcherby, Martin J Booth, Rimas Juskaitis, and Tony Wilson. Real-time extended depth of field microscopy. *Optics express*, 16(26):21843–21848, 2008.

[91] Edward J Botcherby, Martin J Booth, Rimas Juskaitis, and Tony Wilson. Real-time slit scanning microscopy in the meridional plane. *Optics letters*, 34(10):1504–1506, 2009.

[92] F. Anselmi, C. Ventalon, a. Begue, D. Ogden, and V. Emiliani. From the Cover: Three-dimensional imaging and photostimulation by remote-focusing and holographic light patterning. *Proceedings of the National Academy of Sciences*, 108(49):19504–19509, 2011.

[93] Erich E. Hoover, Jeffrey J. Field, David G. Winters, Michael D. Young, Eric V. Chandler, John C. Speirs, Jacob T. Lapenna, Susy M. Kim, Shi You Ding, Randy A. Bartels, Jing W. Wang, and Jeff A. Squier. Eliminating the scattering ambiguity in multifocal, multimodal, multiphoton imaging systems. *Journal of Biophotonics*, 5(5-6):425–436, 2012.

[94] Erich E Hoover, Michael D Young, Eric V Chandler, Anding Luo, Jeffrey J Field, Kraig E Sheetz, Anne W Sylvester, and Jeff a Squier. Remote focusing for programmable multi-layer differential multiphoton microscopy. *Biomedical optics express*, 2(1):113–122, 2010.

[95] Joseph P. Zinter and Michael J. Levene. Maximizing fluorescence collection efficiency in multiphoton microscopy. *Optics Express*, 19(16):15348, 2011.

[96] Lily Zheng. Third-harmonic generation of intense laser pulses, 1996.

[97] Francesco S. Pavone and Paul J. Campagnola. *Second harmonic generation imaging*. CRC Press, Taylor & Francis, 2013.

[98] W Denk, J H Strickler, and W W Webb. Two-photon laser scanning fluorescence microscopy. *Science (New York, N.Y.)*, 248(4951):73–6, apr 1990.

[99] S Mehravar, R A Norwood, N Peyghambarian, and K Kieu. Real-time dual-comb spectroscopy with a free-running femtosecond fiber laser. 231104:4–5, 2016.

[100] Antti Säynätjoki, Lasse Karvonen, Juha Riikonen, Wonjae Kim, Soroush Mehravar, Robert a. Norwood, Nasser Peyghambarian, Harri Lipsanen, and Khanh Kieu. Rapid large-area multiphoton microscopy for characterization of graphene. *ACS Nano*, 7(10):8441–8446, 2013.

[101] Lasse Karvonen, Antti Säynätjoki, Soroush Mehravar, Raul D Rodriguez, Susanne Hartmann, Dietrich R T Zahn, Seppo Honkanen, Robert A Norwood, N Peyghambarian, Khanh Kieu, Harri Lipsanen, and Juha Riikonen. Investigation of second- and third-harmonic generation in few-layer gallium selenide by multiphoton microscopy. *Scientific reports*, 5(April):10334, 2015.

[102] Jannatul Susoma, Lasse Karvonen, Antti Säynätjoki, Soroush Mehravar, Robert A. Norwood, Nasser Peyghambarian, Khanh Kieu, Harri Lipsanen, and Juha Riikonen. Second and third harmonic generation in few-layer gallium telluride characterized by multiphoton microscopy. *Applied Physics Letters*, 108(7), 2016.

[103] Brittany Lynn, Alexander Miles, Soroush Mehravar, Pierre-Alexandre Blanche, Khanh Kieu, Robert A. Norwood, and N. Peyghambarian. Real-time imaging of chromophore alignment in photorefractive polymer de-

vices through multiphoton microscopy. *MRS Communications*, 5(02):243–250, jun 2015.

[104] Ioanna Sakellari, Elmina Kabouraki, David Gray, Vytautas Purlys, Costas Fotakis, Alexander Pikulin, Nikita Bityurin, Maria Vamvakaki, and Maria Farsari. Diffusion-assisted high-resolution direct femtosecond laser writing. *ACS Nano*, 6(3):2302–2311, 2012.

[105] Babak Amirsolaimani, Oscar D. Herrera, Roland Himmelhuber, Khanh Kieu, Robert A. Norwood, and Nasser Peyghambarian. Electro-optic polymer channel waveguide fabrication using multiphoton direct laser writing. In *2015 IEEE Optical Interconnects Conference (OI)*, pages 104–105. IEEE, apr 2015.

[106] Richard W Cole, Tushare Jinadasa, and Claire M Brown. Measuring and interpreting point spread functions to determine confocal microscope resolution and ensure quality control. *Nature protocols*, 6(12):1929–41, 2011.

[107] P. A. Young, S. G. Clendenon, J. M. Byars, R. S. Decca, and K. W. Dunn. The effects of spherical aberration on multiphoton fluorescence excitation microscopy. *Journal of Microscopy*, 242(2):157–165, 2011.

[108] Godefridus J. Brakenhoff, G. W H Wurpel, K. Jalink, L. Oomen, L. Brocks, and J. M. Zwier. Characterization of sectioning fluorescence microscopy with thin uniform fluorescent layers: Sectioned Imaging Property or SIPcharts. *Journal of Microscopy*, 219(3):122–132, 2005.

[109] a. Antonini, C. Liberale, and T. Fellin. Fluorescent layers for characterization of sectioning microscopy with coverslip-uncorrected and water immersion objectives. *Optics Express*, 22(12):14293, 2014.

[110] C Eggeling, J Widengren, R Rigler, and C a Seidel. Photobleaching of Fluorescent Dyes under Conditions Used for Single-Molecule Detection:âĂL' Evidence of Two-Step Photolysis. *Analytical chemistry*, 70(13):2651–2659, 1998.

[111] G H Patterson and D W Piston. Photobleaching in two-photon excitation microscopy. *Biophysical journal*, 78(4):2159–62, 2000.

[112] J. M. Zwier, G. J. Van Rooij, J. W. Hofstraat, and G. J. Brakenhoff. Image calibration in fluorescence microscopy. *Journal of Microscopy*, 216(1):15–24, 2004.

[113] G. Vicidomini, M. Schneider, P. Bianchini, S. Krol, T. Szellas, and A. Diaspro. Characterization of uniform ultrathin layer for z-response measurements in three-dimensional section fluorescence microscopy. *Journal of Microscopy*, 225(1):88–95, 2007.

[114] J M Khosrofian and B a Garetz. Measurement of a Gaussian laser beam diameter through the direct inversion of knife-edge data. *Applied optics*, 22(21):3406, 1983.

[115] Marcos a C de Araújo, Rubens Silva, Emerson de Lima, Daniel P Pereira, and Paulo C de Oliveira. Measurement of Gaussian laser beam radius using the knife-edge technique: improvement on data analysis. *Applied optics*, 48(2):393–396, 2009.

[116] Yi Chiu and Jiun-Hung Pan. Micro knife-edge optical measurement device in a silicon-on-insulator substrate. *Optics express*, 15(10):6367–6373, 2007.

[117] K Kieu, R J Jones, and N Peyghambarian. High power femtosecond source near 1 micron based on an all-fiber Er-doped mode-locked laser. *Optics express*, 18(20):21350–21355, 2010.

[118] Caroline a Schneider, Wayne S Rasband, and Kevin W Eliceiri. NIH Image to ImageJ: 25 years of image analysis. *Nature Methods*, 9(7):671–675, 2012.

[119] C. Sheppard and M. Gu. Image formation in two-photon fluorescence microscopy. *Optik*, 86(3):104–106, 1990.

[120] Gary W. Falk. Risk Factors for Esophageal Cancer Development. *Surgical Oncology Clinics of North America*, 18(3):469–485, 2009.

[121] Hutchinson Cancer Research Center. Esophageal cancer risk may be reduced through a variety of lifestyle factorsâĂŞfrom taking aspirin to losing belly fat. Fred. *Hutchinson Cancer Research Center*, 2013.

[122] M Solaymani-Dodaran, R F A Logan, J West, T Card, and C Coupland. Risk of oesophageal cancer in Barrett's oesophagus and gastro-oesophageal reflux. *Gut*, 53(8):1070–1074, aug 2004.

[123] Stuart J. Spechler and Rhonda F. Souza. Barrett's Esophagus. *http://dx.doi.org/10.1056/NEJMra1314704*, 2014.

[124] David J. Kearney, Casey Crump, Charles Maynard, and Edward J. Boyko. A case-control study of endoscopy and mortality from adenocarcinoma of the esophagus or gastric cardia in persons with GERD. *Gastrointestinal Endoscopy*, 57(7):823–829, 2003.

[125] Nicholas J. Shaheen, Prateek Sharma, Bergein F. Overholt, Herbert C. Wolfsen, Richard E. Sampliner, Kenneth K. Wang, Joseph A. Galanko, Mary P. Bronner, John R. Goldblum, Ana E. Bennett, Blair A. Jobe, Glenn M. Eisen, M. Brian Fennerty, John G. Hunter, David E. Fleischer, Virender K. Sharma, Robert H. Hawes, Brenda J. Hoffman, Richard I. Rothstein, Stuart R. Gordon, Hiroshi Mashimo, Kenneth J. Chang, V. Raman Muthusamy, Steven A.

Edmundowicz, Stuart J. Spechler, Ali A. Siddiqui, Rhonda F. Souza, Anthony Infantolino, Gary W. Falk, Michael B. Kimmey, Ryan D. Madanick, Amitabh Chak, and Charles J. Lightdale. Radiofrequency Ablation in Barrett's Esophagus with Dysplasia. *http://dx.doi.org/10.1056/NEJMoa0808145*, 2009.

[126] Oliver Pech, Andrea May, Hendrik Manner, Angelika Behrens, Jürgen Pohl, Maren Weferling, Urs Hartmann, Nicola Manner, Josephus Huijsmans, Liebwin Gossner, Thomas Rabenstein, Michael Vieth, Manfred Stolte, and Christian Ell. Long-term Efficacy and Safety of Endoscopic Resection for Patients With Mucosal Adenocarcinoma of the Esophagus. *Gastroenterology*, 146(3):652–660.e1, 2014.

[127] Denis Chatelain and Jean-François Fléjou. High-grade dysplasia and superficial adenocarcinoma in Barrett's esophagus: histological mapping and expression of p53, p21 and Bcl-2 oncoproteins. *Virchows Archiv : an international journal of pathology*, 442(1):18–24, jan 2003.

[128] John R Goldblum and Gregory Y Lauwers. Dysplasia arising in barrett's esophagus: diagnostic pitfalls and natural history. *Seminars in diagnostic pathology*, 19(1):12–9, feb 2002.

[129] B.J. Reid, R.C. Haggitt, C.E. Rubin, G. Roth, C.M. Surawicz, G. Van Belle, K. Lewin, W.M. Weinstein, D.A. Antonioli, H. Goldman, W. MacDonald, and D. Owen. Observer variation in the diagnosis of dysplasia in Barrett's esophagus. *Human Pathology*, 19(2):166–178, feb 1988.

[130] Elizabeth Montgomery, Mary P. Bronner, John R. Goldblum, Joel K. Greenson, Marian M. Haber, John Hart, Laura W. Lamps, Gregory Y. Lauwers, Audrey J. Lazenby, David N. Lewin, Marie E. Robert, Alicia Y. Toledano,

Yu Shyr, and Kay Washington. Reproducibility of the diagnosis of dysplasia in Barrett esophagus: A reaffirmation. *Human Pathology*, 32(4):368–378, 2001.

[131] Nathan A Gray, Robert D Odze, and Stuart Jon Spechler. Buried Metaplasia After Endoscopic Ablation of Barrett's Esophagus: A Systematic Review. *The American Journal of Gastroenterology*, 106(11):1899–1908, nov 2011.

[132] E. Chabrun, M. Marty, and F. Zerbib. Development of esophageal adenocarcinoma on buried glands following radiofrequency ablation for Barrett's esophagus. *Endoscopy*, 44(S 02):E392–E392, nov 2012.

[133] R. Odze and G. Lauwers. Histopathology of Barrett's esophagus after ablation and endoscopic mucosal resection therapy. *Endoscopy*, 40(12):1008–1015, dec 2008.

[134] Helen Lantz and Nimish Vakil. Barrett's esophagus and argon plasma coagulation: buried trouble? *The American journal of gastroenterology*, 98(7):1647–9, jul 2003.

[135] Prateek Sharma, Robert H Hawes, Ajay Bansal, Neil Gupta, Wouter Curvers, Amit Rastogi, Mandeep Singh, Matt Hall, Sharad C Mathur, Sachin B Wani, Brenda Hoffman, Srinivas Gaddam, Paul Fockens, and Jacques J Bergman. Standard endoscopy with random biopsies versus narrow band imaging targeted biopsies in Barrett's oesophagus: a prospective, international, randomised controlled trial. *Gut*, 62(1):15–21, jan 2013.

[136] Michael J Connor and Prateek Sharma. Chromoendoscopy and magnification endoscopy in Barrett's esophagus. *Gastrointestinal Endoscopy Clinics of North America*, 13(2):269–277, 2003.

[137] Elizabeth L Bird-Lieberman, André A Neves, Pierre Lao-Sirieix, Maria O'Donovan, Marco Novelli, Laurence B Lovat, William S Eng, Lara K Mahal, Kevin M Brindle, and Rebecca C Fitzgerald. Molecular imaging using fluorescent lectins permits rapid endoscopic identification of dysplasia in Barrett's esophagus. *Nature Medicine*, 18(2):315–321, jan 2012.

[138] Timothy J. Muldoon, Sharmila Anandasabapathy, Dipen Maru, and Rebecca Richards-Kortum. High-resolution imaging in Barrett's esophagus: a novel, low-cost endoscopic microscope. *Gastrointestinal Endoscopy*, 68(4):737–744, 2008.

[139] D. Adler, C. Zhou, T.-H. Tsai, H.-C. Lee, L. Becker, J. Schmitt, Q. Huang, J. Fujimoto, and H. Mashimo. Three-dimensional optical coherence tomography of Barrett's esophagus and buried glands beneath neosquamous epithelium following radiofrequency ablation. *Endoscopy*, 41(09):773–776, sep 2009.

[140] Bevin Lin, Shiro Urayama, Ramez M. G Saroufeem, Dennis L. Matthews, and Stavros G. Demos. Establishment of rules for interpreting ultraviolet autofluorescence microscopy images for noninvasive detection of Barrett's esophagus and dysplasia. *Journal of Biomedical Optics*, 17(1):016013, 2012.

[141] Winfried Denk, James H Strickler, and Watr W Webb. Two-Photon Laser Scanning Fluorescence Microscopy Author ( s ): Winfried Denk , James H . Strickler and Watt W . Webb Published by : American Association for the Advancement of Science Stable URL : http://www.jstor.org/stable/2874052 Accessed : 24-04-2016. 248(4951):73–76, 2016.

[142] Melissa C Skala, Jayne M Squirrell, Kristin M Vrotsos, Jens C Eickhoff, Annette Gendron-Fitzpatrick, Kevin W Eliceiri, and Nirmala Ramanujam.

Multiphoton microscopy of endogenous fluorescence differentiates normal, precancerous, and cancerous squamous epithelial tissues. *Cancer research*, 65(4):1180–6, feb 2005.

[143] Serena Wong, Michael H. Nathanson, Jianxin Chen, and Dhanpat Jain. Evaluation of barrett esophagus by multiphoton microscopy. *Archives of Pathology and Laboratory Medicine*, 138(2):204–212, 2014.

[144] Jason N. Rogart, Jun Nagata, Caroline S. Loeser, Robert D. Roorda, Harry Aslanian, Marie E. Robert, Warren R. Zipfel, and Michael H. Nathanson. Multiphoton Imaging Can Be Used for Microscopic Examination of Intact Human Gastrointestinal Mucosa Ex Vivo. *Clinical Gastroenterology and Hepatology*, 6(1):95–101, 2008.

[145] Tzu-Lin Sun, Yuan Liu, Ming-Chin Sung, Hsiao-Ching Chen, Chun-Hui Yang, Vladimir Hovhannisyan, Wei-Chou Lin, Yung-Ming Jeng, Wei-Liang Chen, Ling-Ling Chiou, Guan-Tarn Huang, Ki-Hean Kim, Peter T. C. So, Yang-Fang Chen, Hsuan-Shu Lee, and Chen-Yuan Dong. Ex vivo imaging and quantification of liver fibrosis using second-harmonic generation microscopy. *Journal of Biomedical Optics*, 15(3):036002, 2010.

[146] Shuangmu Zhuo, Jianxin Chen, Guizhu Wu, Shusen Xie, Liqin Zheng, Xingshan Jiang, and Xiaoqin Zhu. Quantitatively linking collagen alteration and epithelial tumor progression by second harmonic generation microscopy. *Applied Physics Letters*, 96(21):94–97, 2010.

[147] D Yelin and Y Silberberg. Laser scanning third-harmonic-generation microscopy in biology. *Optics express*, 5(8):169–175, 1999.

[148] G. Omar Clay, Andrew C. Millard, Chris B. Schaffer, Juerg Aus-der Au, Philbert S. Tsai, Jeffrey a. Squier, and David Kleinfeld. Spectroscopy of

third-harmonic generation: evidence for resonances in model compounds and ligated hemoglobin. *Journal of the Optical Society of America B*, 23(5):932, 2006.

[149] Jung-Hoon Park, Wei Sun, and Meng Cui. High-resolution in vivo imaging of mouse brain through the intact skull. *Proceedings of the National Academy of Sciences*, 112(30):9236–9241, 2015.

[150] Eung Jang Lee, Boram Kim, Hong-Gyu Ahn, Seung-Han Park, Eunji Cheong, and Sangyoup Lee. In-vivo and label-free imaging of cellular and tissue structures in mouse ear skin by using second- and third-harmonic generation microscopy. *Journal of the Korean Physical Society*, 66(4):597–601, 2015.

[151] Louis Jay, Jean Michel Bourget, Benjamin Goyer, Kanwarpal Singh, Isabelle Brunette, Tsuneyuki Ozaki, and St??phanie Proulx. Characterization of tissue-engineered posterior corneas using second- and third-harmonic generation microscopy. *PLoS ONE*, 10(4):1–13, 2015.

[152] J Ohanna T Rägårdh, G Illian R Obb, K Amal K E G Adalla, S Tuart C Obb, C Hristopher T Ravis, G I A N U C A O Ppo, and G A I L M C C Onnell. Label-free imaging of thick tissue at 1550 nm using a femtosecond optical parametric generator. 40(15):3484–3487, 2015.

[153] Sunil Kumar, Tschackad Kamali, Jonathan M. Levitte, Ori Katz, Boris Hermann, Rene Werkmeister, Boris Považay, Wolfgang Drexler, Angelika Unterhuber, and Yaron Silberberg. Single-pulse CARS based multimodal nonlinear optical microscope for bioimaging. *Optics Express*, 23(10):13082, 2015.

[154] Omid Masihzadeh, Tim C Lei, Scott R Domingue, Malik Y Kahook, Randy A Bartels, and David A Ammar. Third harmonic generation microscopy of a mouse retina. *Molecular Vision*, 21(April):538–547, 2015.

[155] Yu-Cheng Chen, Szu-Yu Lee, Yana Wu, Kirstin Brink, Dar-Bin Shieh, Timothy D Huang, Robert R Reisz, and Chi-Kuang Sun. Third-harmonic generation microscopy reveals dental anatomy in ancient fossils. *Optics letters*, 40(7):1354–7, 2015.

[156] Murat Yildirim, Nicholas Durr, and Adela Ben-Yakar. Tripling the maximum imaging depth with third-harmonic generation microscopy. *Journal of Biomedical Optics*, 20(9):096013–096013, 2015.

[157] K Kieu, S Mehravar, R Gowda, Robert A. Norwood, and N Peyghambarian. Label-free multi-photon imaging using a compact femtosecond fiber laser mode-locked by carbon nanotube saturable absorber. *Biomedical optics express*, 4(10):2187–95, 2013.

[158] Stephan Preibisch, Stephan Saalfeld, and Pavel Tomancak. Globally optimal stitching of tiled 3D microscopic image acquisitions. *Bioinformatics*, 25(11):1463–1465, 2009.

[159] L. C U Junqueira, G. Bignolas, and R. R. Brentani. Picrosirius staining plus polarization microscopy, a specific method for collagen detection in tissue sections. *The Histochemical Journal*, 11(4):447–455, 1979.

[160] Holde Puchtler, Faye Sweat Waldrop, and Linda S. Valentine. Polarization Microscopic Studies of Connective Tissue Stained with Picro-Sirius Red FBA. *Beiträge zur Pathologie*, 150(2):174–187, 1973.

[161] P. Whittaker, R. A. Kloner, D. R. Boughner, and J. G. Pickering. Quantitative assessment of myocardial collagen with picrosirius red staining and circularly polarized light. *Basic Research in Cardiology*, 89(5):397–410, 1994.

[162] Ioannis Polyzos, George Tsigaridas, Mihalis Fakis, Vassilis Giannetas, Peter Persephonis, and John Mikroyannidis. Substituent effect on the photo-

bleaching of pyrylium salts under ultrashort pulsed illumination. *Journal of Physical Chemistry B*, 110(6):2593–2597, 2006.

[163] Meindert A van Dijk, Lukas C Kapitein, Joost van Mameren, Christoph F Schmidt, and Erwin J G Peterman. Combining optical trapping and single-molecule fluorescence spectroscopy: enhanced photobleaching of fluorophores. *The journal of physical chemistry. B*, 108:6479–6484, 2004.

[164] I Polyzos, G Tsigaridas, M Fakis, V Giannetas, and P Persephonis. Three-photon induced photobleaching in a three-dimensional memory material. *Optics letters*, 30(19):2654–2656, 2005.

[165] Two-photon Three-dimensional Optical Storage Memory. Storage Memory. pages 843–845, 1994.

[166] Daniil N. Bratashov, Admir Masic, Alexey M. Yashchenok, Matthieu F. Bedard, Olga A. Inozemtseva, Dmitry A. Gorin, Tamara Basova, Torsten K. Sievers, Gleb B. Sukhorukov, Mathias Winterhalter, Helmuth M??hwald, and Andre G. Skirtach. Raman imaging and photodegradation study of phthalocyanine containing microcapsules and coated particles. *Journal of Raman Spectroscopy*, 42(10):1901–1907, 2011.

[167] J. Mertz. Molecular photodynamics involved in multi-photon excitation fluorescence microscopy. *The European Physical Journal D*, 3(1):53–66, 1998.

[168] D Day, M Gu, and A Smallridge. Use of two-photon excitation for erasable-rewritable three-dimensional bit optical data storage in a photorefractive polymer. *Optics letters*, 24(14):948–950, 1999.

[169] I Polyzos, G Tsigaridas, M Fakis, V Giannetas, and P Persephonis. Two-photon absorption properties of novel organic materials for three-dimensional optical memories. 369:264–268, 2003.

[170] S. Gavrilyuk, S. Polyutov, P. C. Jha, Z. Rinkevicius, H. ??gren, and F. Gel'Mukhanov. Many-photon dynamics of photobleaching. *Journal of Physical Chemistry A*, 111(47):11961–11975, 2007.

[171] E.L. Wooten, K.M. Kissa, a. Yi-Yan, E.J. Murphy, D.a. Lafaw, P.F. Hallemeier, D. Maack, D.V. Attanasio, D.J. Fritz, G.J. McBrien, and D.E. Bossi. A review of lithium niobate modulators for fiber-optic\ncommunications systems. *IEEE Journal of Selected Topics in Quantum Electronics*, 6(1):69–82, 2000.

[172] Mahmoud M. Abouelleil and Fred J. Leonberger. Waveguides in lithium niobate. *Journal of the American Ceramic Society*, 72(8):1311–1321, 1989.

[173] H. R. S. Mahdavi, E. Mohajerani, M. Mohseni, and Y. Aghili. A novel approach to analyze photoinduced effects in a DR1 dye-doped hybrid nanocomposite film. *Journal of Sol-Gel Science and Technology*, 52(1):82–87, 2009.

[174] Reuven Chen and P. L. Leung. The decay of OSL signals as stretched-exponential functions. *Radiation Measurements*, 37(4-5):519–526, 2003.

[175] A. Galvan-Gonzalez, M. Canva, G.I. I Stegeman, R. Twieg, T.C. C Kowalczyk, and H.S. S Lackritz. Effect of temperature and atmospheric environment on the photodegradation of some Disperse Red 1-type polymers. *Optics letters*, 24(23):1741–1743, 1999.

[176] Roland Himmelhuber, Khanh Kieu, Oscar D. Herrera, Robert a. Norwood, and Nasser Peyghambarian. Characterization of coplanar poled electro optic polymer films for Si-photonic devices with multiphoton microscopy. *2013 Optical Interconnects Conference, OI 2013*, 161109:90–91, 2013.

[177] Tapani Alasaarela, Lasse Karvonen, Henri Jussila, Antti Säynätjoki, Soroush Mehravar, Robert a Norwood, Nasser Peyghambarian, Khanh

Kieu, Ilkka Tittonen, and Harri Lipsanen. High-quality crystallinity controlled ALD TiO2 for waveguiding applications. *Optics letters*, 38(20):3980–3, 2013.

[178] Tommi Kaplas, Lasse Karvonen, Sepehr Ahmadi, Babak Amirsolaimani, Soroush Mehravar, Nasser Peyghambarian, Khanh Kieu, Seppo Honkanen, Harri Lipsanen, and Yuri Svirko. Optical characterization of directly deposited graphene on a dielectric substrate. *Optics Express*, 24(3):2965, 2016.

[179] Matthew W. Puckett, Rajat Sharma, Felipe Vallini, Shiva Shahin, Faraz Monifi, Peter N. Barrina, Soroush Mehravar, Khanh Kieu, and Yeshaiahu Fainman. Silicon Nanoridge Array Waveguides for Nonlinear and Sensing Applications. 23(22):28224–28233, 2015.

[180] Byron Cocilovo, Oscar D. Herrera, Soroush Mehravar, Yunnan Fang, Kenneth H. Sandhage, Khanh Kieu, and Robert A. Norwood. Surface-Enhanced Two-Photon Excitation Fluorescence of Various Fluorophores Evaluated Using a Multiphoton Microscope. *Journal of Lightwave Technology*, 33(16):3446–3452, 2015.